博士論文（要約）

Study on Alumina Reduction by Laser Ablation

（レーザーアブレーションによるアルミナ還元に関する研究）

田中　聖也

Seiya Tanaka

Department of Aeronautics and Astronautics

School of Engineering

The University of Tokyo

Study on Alumina Reduction by Laser Ablation

by

Seiya Tanaka

Submitted to the Department of Aeronautics and Astronautics on February 9, 2022,
in partial fulfillment of the requirements for the degree of Doctor of Engineering

Abstract

Alumina reduction by laser ablation using a continuous-wave (CW) laser was investigated with the eventual goal of lunar resource utilization. A large aluminum collection rate in the laser ablation method using a CW laser was expected because of its high laser input energy.

The existence of aluminum atoms in the ablation plume, which was ejected from an alumina rod surface by laser ablation, was detected by emission spectroscopy. This result indicates the alumina dissociation into aluminum is successfully conducted by laser ablation using a CW laser. The plume temperature was increased up to 4,100 K, and the molar reduction percentage achieved 32% by alumina rod preheating. The limitation of plume temperature was estimated to be the superheat limit temperature of alumina. The ablation rate was affected by laser intensity and laser spot occupancy. Therefore, for maximum aluminum production, the laser irradiation condition can be optimized.

Moreover, aluminum particles were detected on the alumina rod surface after laser ablation. For the mechanism of aluminum particle nucleation, impurity precipitation from oxygen-deficient alumina, which would be produced on the alumina rod surface by laser ablation, was proposed. From evaluation of the aluminum particle distribution with SEM observation and EDX analysis, the surface condition of alumina rod during aluminum particle nucleation was temperatures of 933–2,300 K and cooling rates of alumina rod surface, which affected the impurity precipitation, was measured to be 600–800 K/s. The obtained conditions would be applicable to the aluminum collection from the ablation plume because it is validated that the aluminum particle nucleation on the alumina rod surface obeyed the heterogeneous nucleation theory.

Aluminum collection from ablation plume using a temperature-controlled collection plate was conducted by applying the obtained temperature conditions of aluminum particle nucleation. At a plate temperature of 1,500 K, aluminum adhered to a tantalum collection plate. The measured aluminum collection percentage was 2.0%, which was two orders of magnitude larger than the previous result using a collection tube. By combining the optimized alumina dissociation condition and the established efficient aluminum collection system, the aluminum collection rate was measured to 0.11 mg/s, which was three orders of magnitude larger than the measured rate in the laser ablation method using a pulsed laser in the previous research.

Thesis Supervisor: Prof. Kimiya Komurasaki

Contents

List of Figures

List of Tables

Nomenclature

c = speed of light

c_{H2} = concentration of hydrogen gas

c_{heat} = specific heat

C_2 = second radiation constant

D = diffusion coefficient

D_0 = constant in diffusion coefficient

E_{Al} = energy consumption for 1 kg aluminum production

$E_{\mathrm{Al\_th}}$ = theoretical value of energy consumption for 1 kg aluminum production

E_{b} = heat of vaporization

E_{d} = dissociation energy

E_{m} = heat of melting

E_{s} = surface energy of wall

F = laser intensity

f = focal length

G = Gibbs free energy

ΔG^* = Gibbs free energy at the critical radius

$\Delta_f G$ = standard Gibbs free energy of formation

h = Planck's constant

ΔH_{v} = latent heat of vaporization

I = emission intensity

J_{nu} = nucleation rate

J_{D} = diffusion flux

J_{re} = chemical reaction rate

k = Boltzmann's constant

M = atomic or molecular weight

M^2 = M squared, M^2=12–13 in the CW laser used in this research
m = mass of atom
$\dot{m}_{\mathrm{ab}}$ = ablation rate
$\dot{m}_{\mathrm{Al}}$ = aluminum collection rate
m_{Al} = aluminum mass
n = number density
n_{Al} = number density of aluminum
n_{l} = number density of bulk liquid
n_{p} = number of particles
n_{su} = number density of supersaturated vapor
P = ambient pressure
P^0 = standard pressure
P_{Al} = aluminum vapor pressure
P_{Laser} = input laser power
P_{O2} = partial pressure of oxygen
P_{s} = saturated vapor pressure
Q = activation energy of diffusion
R = gas constant
R_{L} = radius of input beam
Re = Reynolds number
r = distance from rod center
r_{a} = alumina rod radius
r_{L} = laser spot size (radius)
r_{p} = particle radius
r_{p}^* = critical radius
T = plume temperature
T_{c} = critical temperature
T_{cp} = collection plate temperature
T_{pre} = preheating temperature
T_{rod} = rod surface temperature
T_{s} = surface temperature
T_{th} = superheat limit temperature
t = period from beginning of laser irradiation

t_{ox} = oxide film thickness
V_{s} = volume of sealed vessel
v_{p} = particle volume
x_i = molar number
z = distance from focal point along the beam propagation axis
α = laser spot occupancy, area ratio of laser spot to alumina rod surface
ε = emissivity
η_{co} = aluminum collection percentage
η_{re} = molar reduction percentage
θ = contact angle
λ = wavelength
μ = chemical potential
μ^0 = chemical potential at standard pressure
μ_v = viscosity coefficient
ρ_{Al} = density of aluminum
ρ_{g} = gas density
ρ_{l} = liquid density
ς = surface coverage of aluminum
σ = surface tension
Φ = viscous dissipation term

Subscripts

i = number of chemical species
j = number of SEM images

Chapter 1

Introduction

1.1 In-situ resource utilization (ISRU) on the Moon

The construction of a manned lunar base has been proposed by several organizations such as NASA, ESA, and JAXA with the aim of planetary geological surveys conducted by sample returns and deep space exploration [1–4]. Nevertheless, the transportation costs of building materials for the lunar base and oxygen for humans from the Earth are enormous, making lunar base construction unrealistic. For realization of low-cost space exploration, the utilization of local resources has been proposed based on in situ resource utilization (ISRU) [5–12]. ISRU, as the name implies, is a concept of living off local resources without transporting materials from the Earth.

The lunar surface contains a resource called regolith, mixed various minerals [13]. Because there is no atmosphere on the lunar surface, fine particles falling at high speed from the space do not burn up in the atmosphere as they do on the Earth. The falling particles impact the lunar surface, scraping off the rocks and creating regolith. The utilization of lunar regolith has been researched variously [14–17]. The production of cement concrete from the lunar regolith, for example, has been researched for the building materials of the lunar base.

In addition to the utilization of lunar regolith itself, material extraction from regolith is one of the most valuable ways of the lunar resource utilization. Alumina is one of the most attractive materials in the lunar regolith. The composition of lunar constituents resembles that of the Earth: alumina (Al_2O_3) accounts for 32% of the representative mineral on the Lunar Highlands, as presented in Figure 1-1 [12]. A large amount of aluminum and oxygen would be readily obtainable on the Moon by alumina reduction from the lunar regolith. The alumina in the Lunar Highlands regolith exists in the state of aluminosilicate $Al_2O_3 \cdot nSiO_2$: ferroan anorthite and plagioclase feldspar [12]. The acquisition of aluminum and oxygen requires alumina extraction from the lunar regolith and alumina reduction without consumables to be consistent with ISRU.

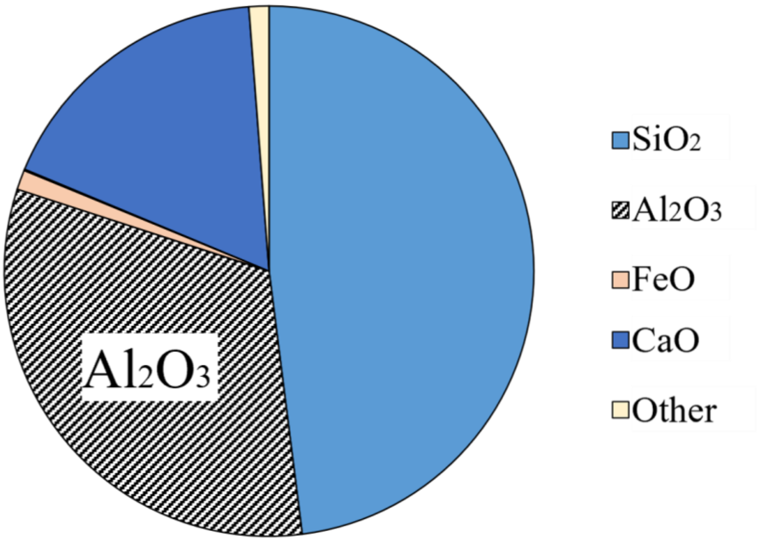

Figure 1-1 Chemical composition of plagioclase in the lunar regolith.

1.2 Characteristics of aluminum

Aluminum is a relatively new metal, discovered in the 19th century because alumina reduction needs enormous energy. However, aluminum has been used in various fields from architecture to aerospace widely because of its unique characteristics. In addition, the utilization of aluminum, which can be obtained by alumina reduction from the lunar regolith, is expected to advance lunar exploration as a building material of lunar bases. In this section, the unique characteristics of aluminum are described.

HIGH SPECIFIC STRENGTH [18]

Aluminum has high specific strength of aluminum, which is twice that of stainless steel. Aluminum is the lightest of mass-used metals called "ton metals" because of its low specific gravity of 2.7, about one-third that of iron and copper. Despite the lightness of aluminum, the strength of aluminum is only 33% less than that of stainless steel. These unique characteristics make aluminum a representative metal with high-specific strength. Moreover, aluminum alloys with various metals such as copper and magnesium have even higher specific strength than pure aluminum. Duralumin, an example of aluminum alloy, has 1.5 times the specific strength of aluminum. The high-specific strength expands the utilization of aluminum for aircrafts and other various applications, not only the manned lunar base.

SPECIFIC MECHANICAL PROPERTIES AT LOW TEMPERATURE

Aluminum has a unique mechanical property: the strength does not change at low temperatures and increases at cryogenic temperatures [19]. Because of this specific property, aluminum is utilized for liquefied gas and rocket fuel tanks. Aluminum is suitable as a building material for the lunar base, considering the low-temperature condition on the lunar surface: 100 K in the lunar night.

HIGH REFLECTIVITY

High-purity and well-polished aluminum reflects light rays from infrared to ultraviolet and all electromagnetic waves oscillated from radios and radars. Moreover, aluminum can cut alpha and beta rays with a thin thickness [20–21]. Therefore, aluminum has been utilized in space structures directly exposed to cosmic rays. The effects of radiation on humans inside, which is a problem for long-term stays on the lunar surface, could be prevented by making a building out of aluminum materials on the lunar surface.

HIGH CHEMICAL RESISTANCE [22]

Aluminum has a high chemical resistance as a passive material. A thin but dense aluminum-oxide film spontaneously covers aluminum alloys and prevents pure aluminum from chemical reactions with oxygen, water, and other reactive substances. The chemical resistance of aluminum is superior to magnesium, which reacts with hot water. In addition to the harmless of aluminum, its high corrosion resistance increases the safety to handle. Therefore, aluminum has high safety and usability. Because of these properties, aluminum is often used in space development, which requires a high level of safety.

HIGH ENERGY DENSITY

Aluminum has a high energy density: combustion heat of 837 kJ/mol. Table 1 shows a comparison of the energy densities of aluminum and various energy storage materials. The energy density of aluminum is extremely high, about 100 times higher than that of lithium-ion batteries and liquid hydrogen. Aluminum can be expected as the material in batteries and energy storage systems. The high energy density of aluminum suggests that a large amount of energy is required for alumina reduction.

Table 1-1 Energy densities of aluminum and various energy storage materials.

Material	Energy density /(kJ/g)	Energy density /(kJ/cm^3)	Chemical stability
Aluminum	31	84	◎
Magnesium	24	43	○
Li-ion battery	0.36	0.9	△
Liquid H_2	0.60	0.05	×

1.3 Alumina extraction from mineral

1.3.1 Alumina extraction from bauxite on the Earth: the Bayer process

The Bayer process is an industrial method of alumina production from bauxite, which is composed of pure alumina, silicon dioxide and iron oxide [23–24]. In this process, alumina is extracted by a chemical treatment at a high temperature with an aqueous sodium hydroxide solution to remove silicon dioxide and iron oxide. Alumina in bauxite chemically reacts with an aqueous sodium hydroxide solution as described in Eq. (1-1).

$$\mathrm{Al_2O_3 + 2NaOH + 3H_2O \rightarrow 2Na[Al(OH)_4]} \qquad (1\text{-}1).$$

The substances other than alumina in bauxite do not resolve with the aqueous solution of sodium hydroxide. After separating the extraction residue, aluminum hydroxide crystals are precipitated from the sodium aluminate solution and heated to a temperature of 1000 °C to obtain alumina, as shown in Eq. (1-2).

$$\mathrm{2Na[Al(OH)_4] \rightarrow Al_2O_3 + 2NaOH + 3H_2O} \qquad (1\text{-}2).$$

The precipitated solution is reused for the bauxite extraction process in Eq. (1-1) after adjusting the NaOHaq concentration. Therefore, the Bayer process can extract alumina with no usage of consumables.

1.3.2 Alumina extraction from regolith on the Moon

Alumina in the lunar regolith presents in a state of aluminosilicate $\mathrm{Al_2O_3 \cdot \mathit{n}SiO_2}$, not pure alumina [12]. Therefore, the Bayer process is inapplicable to the alumina extraction from the lunar regolith. Instead of the Bayer process, various alumina extraction methods from aluminosilicate have been researched [25]. The extraction methods are not in the practical use of alumina production because the alumina extraction from bauxite using the Bayer process is easy and cheap. However, the alumina extraction methods from aluminosilicate would be applicable for the utilization of lunar resources. The details of the extraction methods are described below.

NITRIC ACID PROCESS

This process is based on the insolubility of silica in nitric acid. Dry clay is chemically treated with nitric acid to form a slightly basic aluminum nitrate solution, in which iron is almost insoluble. The residue composed of silica and iron is extracted from the aluminum nitrate solution by filtration. The solution is concentrated for crystallizing aluminum nitrate nonahydrate. As a result of this process, the aluminum nitrate mother liquor is obtained to be recycled for the first chemical treatment. The precipitated crystals are decomposed to alumina, nitrogen oxides, and water vapor at a temperature of 500°C.

LIME-SODA SINTER PROCESS

The clay, including aluminosilicate, is sintered with limestone and soda ash in this process. As a result of sintering, the aluminosilicate is dissociated and converted to sodium aluminate and dicalcium silicate. The sintered product is chemically treated with dilute sodium carbonate to dissolve the sodium aluminate. Alumina trihydrate is precipitated from the solution by lime treating and desalting. Finally, alumina is obtained by calcining the alumina trihydrate.

HYDROCHLORIC ACID-ISOPROPYL ETHER EXTRACTION PROCESS

In this method, the clay is treated at atmospheric pressure with 20% hydrochloric acid, and the generated slurry is filtered to remove the silicic acid residue. The aluminum chloride solution is obtained by adding isopropyl ether to the slurry. The chloride aluminum, extracted from the solution by evaporative crystallization, is thermally dissociated into alumina solid and hydrochloric acid gas, used in circulation by cooling the hydrochloric acid gas with a large amount of cooling water.

1.4 Alumina reduction by molten salt electrolysis

1.4.1 Electrolysis using carbon electrodes: the Hall–Héroult process

The conventional alumina reduction method is the Hall–Héroult process, the only method in practical use [26]. This method was initially developed by Charles Martin Hall of the United States and Paul Héroult of France in the latter half of the 19th century. The schematic of Hall–Héroult process is presented in Figure 1-2. Alumina is dissolved in molten agent, glacial stone CaF_2, for lowering its melting point from 2,300 K to around 1,000 K. By decreasing the temperature required for alumina melting, the aluminum refining can be conducted at the low temperature. Carbon electrodes, whose source is generally a coke, are inserted and electrolyzed in the melted alumina pool. The alumina is electrolyzed using voltage (3–5 V) with passage of direct current through the carbon electrodes in molten salt of alumina. The produced aluminum is deposited at the cathode. The oxygen from alumina is combined with carbon from the anode to produce carbon dioxide. This method has high current efficiency and low energy consumption of $E_{\mathrm{Al}} = 13$ kWh/kg-Al [27]. The total chemical reactions in the Hall–Héroult process are shown in Eqs. (1-3) and (1-4).

$$\mathrm{Al_2O_3} + \frac{3}{2}\mathrm{C} \rightarrow 2\mathrm{Al} + \frac{3}{2}\mathrm{CO_2} \qquad (1\text{-}3).$$

$$\mathrm{Al_2O_3} + 3\mathrm{C} \rightarrow 2\mathrm{Al} + 3\mathrm{CO} \qquad (1\text{-}4).$$

The Hall-Héroult process, which produces high-purity aluminum at relatively low temperatures, has been widely used due to the limited availability of high-temperature heating methods.

However, carbon, which is consumed enormously in the Hall–Héroult process, cannot be mined from the lunar resources. Therefore, transportation from the Earth is fundamentally essential for the alumina reduction using the Hall–Héroult process for carbon replenishment. This necessity runs counter to the ISRU concept. Therefore, this alumina reduction technique is unsuitable for lunar operations. A carbon-free alumina reduction method is essential for alumina reduction on the Moon.

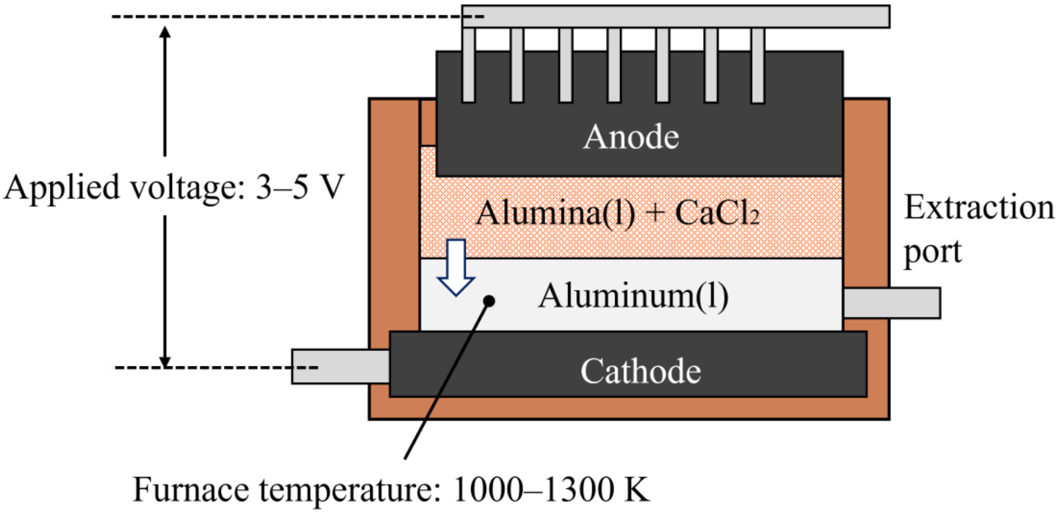

Figure 1-2 Schematic of the Hall–Héroult process.

1.4.2 Electrolysis using inert electrodes

To establish a carbon-free electrolysis method, molten salt electrolysis using inert electrodes has been assessed [28–30]. The inert electrodes are made of materials that do not dissolve with the molten salt and do not react in the electrolysis process. Therefore, instead of using the chemical energy of carbon, only electricity is consumed in this process. In theory, the energy consumption can be approximately E_{Al} =10 kWh/kg-Al, which is smaller than the value in the Hall–Héroult process [31]. The difficulty of inert electrode development, especially anodes, is the multiple requirements for its material [32].

- a low corrosion rate under 10 mm/year
- good resistance to fluorination and produced oxygen
- stable potential and low overpotential for oxygen evolution
- low electrical resistivity for low current efficiency
- adequate mechanical strength and thermal shock resistance
- simple electrical connection
- low cost and ease in manufacturing on an industrial scale

In the previous research, many materials have been tested for the inert anode material: Pt, Ni, Cu–Al–Ni–Fe alloy and Cu-Ni-Fe-O alloy. However, the measured energy consumption for aluminum production was 20–50 kWh/kg-Al, which was larger than the ideal value due to low current efficiency. Moreover, pollution of the inert anode occurred, which necessitates further processing to isolate impurities. These problems are expected to be solved for practical use.

1.5 Alumina reduction by laser heating

To establish a carbon-free alumina reduction method, thermal dissociation methods have been researched: usage of a laser. The chemical reaction formula of thermal dissociation of alumina is presented in Eq. (1-5).

$$\mathrm{Al_2O_3(s)} \rightarrow x_1\mathrm{Al} + x_2\mathrm{AlO} + x_3\mathrm{Al_2O} + x_4\mathrm{AlO_2} + x_5\mathrm{O_2} + x_6\mathrm{O} \qquad \text{(1-5).}$$

In the alumina reduction by laser, the energy consumption for aluminum production is estimated from Eqs. (1-6) and (1-7).

$$E_{\mathrm{Al}} = \frac{P_{\mathrm{Laser}}}{\dot{m}_{\mathrm{Al}}} \qquad \text{(1-6).}$$

$$\dot{m}_{\mathrm{Al}} = \dot{m}_{\mathrm{ab}} \eta_{\mathrm{re}} \frac{2M_{\mathrm{Al}}}{M_{\mathrm{Al_2O_3}}} \eta_{\mathrm{co}} \qquad \text{(1-7).}$$

The unit of P_{Laser} is kWh. The molar reduction percentage η_{re} is the molar percentage of aluminum generated from alumina dissociation to that contained in alumina consumed in the dissociation process. The aluminum collection percentage η_{co} is the percentage of collected aluminum to aluminum generated in the dissociation process.

In this section, firstly, the calculation of molar reduction percentage map and theoretical energy consumption for aluminum production is described to obtain the required values of temperature and pressure. Secondly, the magnesia reduction by laser ablation, which is the first demonstration of reduction by laser ablation, is explained with a concept of magnesium energy cycle. After that, alumina reduction methods by laser heating are described with referring to earlier researches.

1.5.1 Calculation of molar reduction percentage map

The direction of reactions can be estimated from the Gibbs free energy of the chemical system. A negative value for ΔG indicates that a reaction can proceed spontaneously without external inputs because the reactions move in the direction of lower energy of the chemical system. The Gibbs free energy of reduction reaction is calculated from Eq.(1-8).

$$\Delta G = \Delta_f G(T) - RT\, lnP_{O2}. \tag{1-8}$$

The high temperature and low partial pressure of oxygen cause the reduction reactions. The equilibrium composition in the gas mixture can be estimated from the Gibbs free energy. The equilibrium of a system corresponds to the minimum of its Gibbs free energy, which is calculated using Eqs. (1-9) and (1-10).

$$G = \sum_i x_i \mu_i(T, P). \tag{1-9}$$

$$\mu(T, P) = \mu^0(T) + RTln\left(\frac{P}{P^0}\right). \tag{1-10}$$

The equilibrium compositions of the gas mixture containing aluminum and oxygen in a molar ratio of 2:3 were calculated by application of the method developed by White et al. [33] at temperatures of 3,000–6,000 K and for total pressures of 0.1–1.5 atm. For calculations, we used Al, AlO, Al_2O, AlO_2, O_2, and O as chemical species. Their free energy data collected in NIST JANAF tables were used [34]. The calculation result of chemical composition at 1.0 atm is shown in Figure 1-3. The molar ratios of aluminum atom and oxygen atom were increased with plume temperature because the thermal dissociation proceeds with temperature increase. Using results of equilibrium compositions, the molar reduction percentage was calculated as presented in Figure 1-4. This graph shows that low pressure and high temperature are necessary to reduce alumina efficiently. Moreover, Table 1-2 presents the boiling point and 99% dissociation temperature estimated from Gibbs free energy of alumina and magnesia. The gap between boiling point and 99% dissociation temperature is large in alumina. This result indicates the thermal dissociation of alumina is more difficult than that of magnesia, considering the gas temperature increase over the boiling point by a laser.

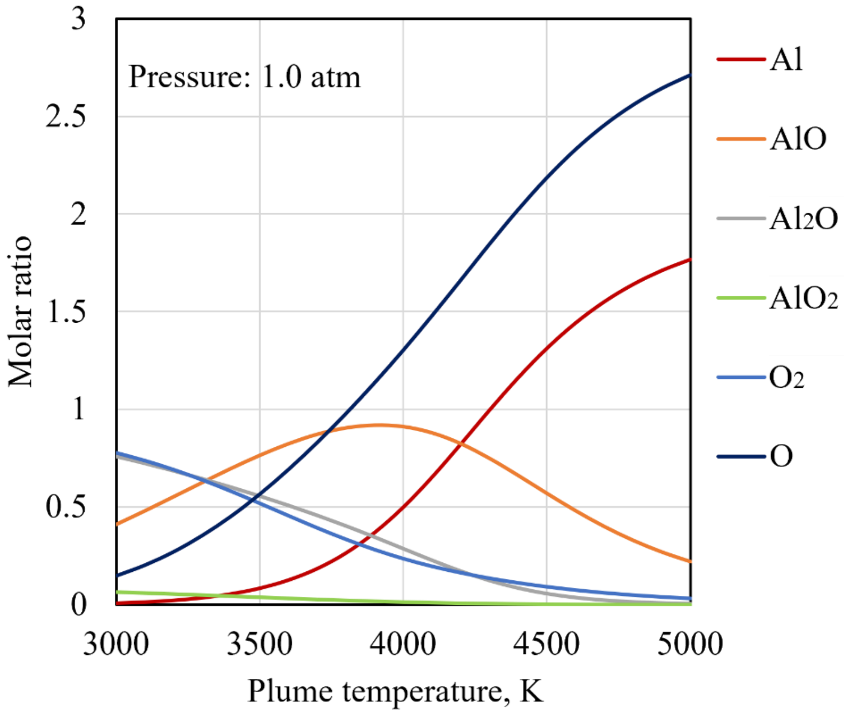

Figure 1-3 Chemical composition of Al-O system with various plume temperatures at 1.0 atm.

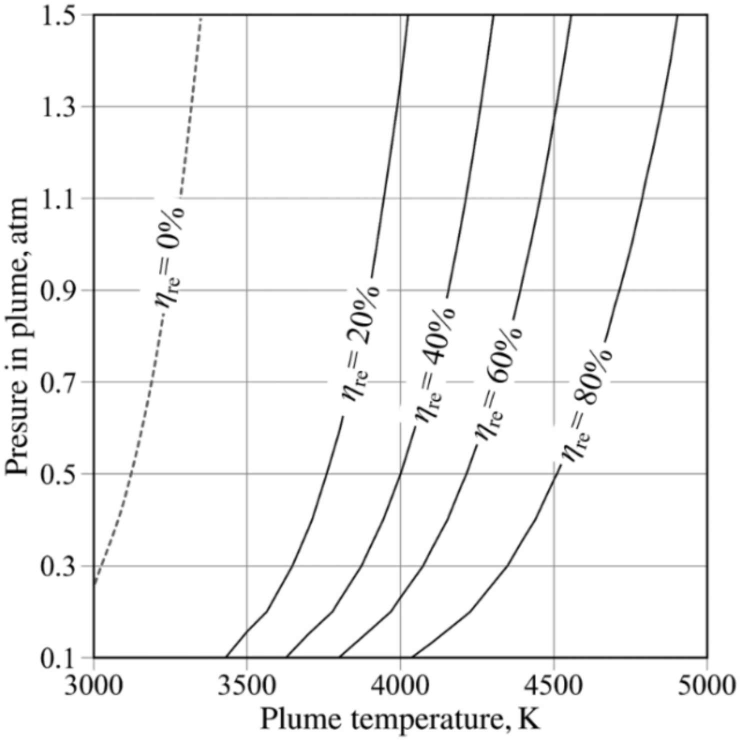

Figure 1-4 Distribution map of molar reduction percentage of alumina in various equilibrium temperatures and ambient pressures.

Table 1-2 Comparison of alumina and magnesia for boiling point and temperature for 99% dissociation at 1.0 atm estimated from Gibbs free energy.

Material	Boiling point/ K	Temperature for 99% dissociation at 1 atm ambient/ K
Alumina, Al_2O_3	3,250	5,400
Magnesia, MgO	3,870	4,000

1.5.2 Calculation of theoretical energy consumption for aluminum production

Assuming that all the input energy is consumed in alumina reduction, the theoretical value of energy consumption for aluminum production was calculated with various plume temperatures at standard pressure: 1.0 atm. The energy consumption for alumina dissociation can be calculated from Eq. (1-11) using the enthalpy change between alumina at 300 K and Al-O system at various temperatures.

$$E_{\mathrm{Al\_th}} = \frac{\Delta H(T,P)}{\dot{m}_{\mathrm{Al}}} \qquad (1\text{-}11).$$

The aluminum collection percentage was assumed to η_{co} = 100%. The enthalpy was calculated from the sum of enthalpies of various Al-O substances. The chemical composition calculated in the previous section was applied in this calculation. NIST-JANAF database was used for the enthalpy of various Al-O substances at different temperatures.

The calculation result of the theoretical energy consumption for aluminum production is presented in Figure 1-5. The theoretical value decreased with plume temperature because of the increase of the molar reduction percentage. The minimum value was obtained at a plume temperature of 5,500 K, not the highest plume temperature applied in this calculation: 6,000 K. This result is caused by the reason that the enthalpy increase by sensible heat becomes more significant than the increase of molar reduction percentage with plume temperature. In other words, at the high plume temperature, the input energy

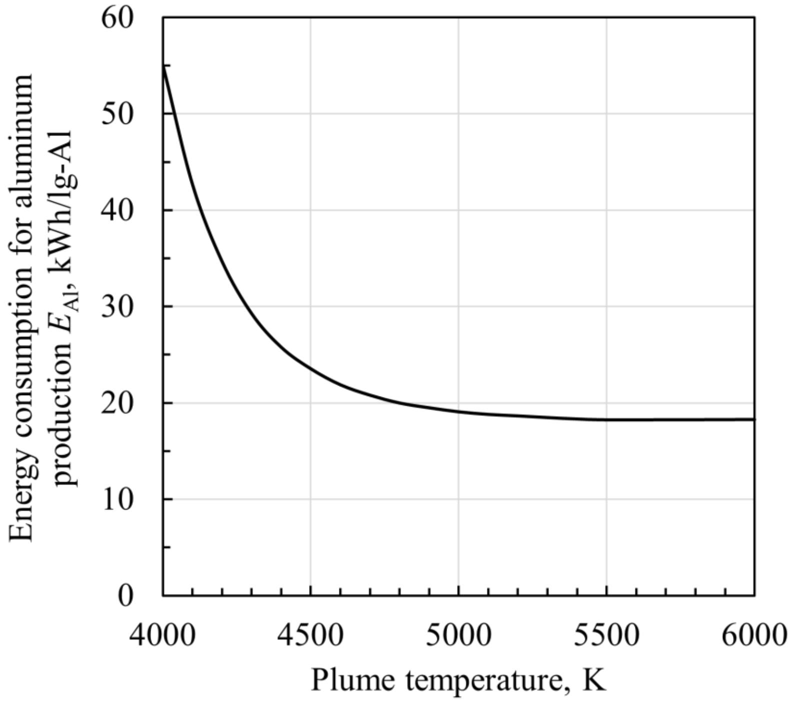

Figure 1-5 Calculated energy consumption for aluminum production with various plume temperatures.

is mainly consumed for increasing the molar reduction percentage. As a result, the ablation rate decreases, and the aluminum collection rate is not the maximum. The theoretical minimum value of energy consumption was $E_{Al\_th} = 18$ kWh/kg-Al, which was 1.8 times larger than the theoretical value of molten salt electrolysis using inert anodes. By applying a solar pumped laser to the laser ablation method, which has higher energy conversion efficiency than solar cells, the energy consumption for aluminum production in the laser ablation method would be smaller than that in the electrolysis method.

1.5.3 Magnesia reduction by laser ablation

MAGNESIUM ENERGY CYCLE

Magnesia reduction by laser ablation has been researched by Yabe for establishment of a magnesium energy cycle with the aim of a carbon-free energy storage system [35–40]. The energy cycle is composed of magnesia reduction and magnesium oxidation processes. In the magnesia reduction process, an enormous amount of energy is stored by magnesium as chemical potential, whose energy density is a few orders of magnitude higher than Li-ion batteries. Stored energy by magnesium does not degrade because its surface is covered with a dense passive film, providing high safety and stability during transportation and storage. The stored energy can be extracted from the chemical reaction of magnesia oxidation whenever required. As a result of this oxidation process, magnesia is produced and reused in the magnesia reduction process of the energy cycle. Therefore, the magnesium energy cycle would realize the carbon-free energy storage system without CO_2 emission with high safety by developing a carbon-free magnesia reduction method.

Moreover, a solar pumped laser has been supposed to be used in the magnesia reduction process. The solar pumped laser, which oscillates a laser beam directly using solar power, produces a laser beam without an additional energy power source and CO_2 gas emission. In addition, the solar pumped laser has high-energy transition efficiency of 30–40% [41–42]. This value is about twice as large as the power generation efficiency of a solar cell: approximately 15–20% [43–44]. Therefore, the solar pumped laser is a great energy source applicable to the reduction process in the magnesia energy cycle.

MAGNESIA REDUCTION METHODS

Laser ablation is a process of removing a surface layer from a solid material by irradiation with a laser beam [45–48]. For achieving necessary high temperature in magnesia dissociation into magnesium and oxygen: estimated to 4,000 K, the laser ablation phenomenon was applied into magnesia reduction. This magnesia reduction method using laser ablation incorporates two processes: magnesia dissociation and magnesium collection. In the laser ablation method, a cylinder-shaped magnesia sample was used as the target sample because the laser energy could be absorbed by passing through the sample inside, not just on the sample surface. The ejected ablation plume containing magnesium atoms dissociated from magnesia sample was cooled down in the collection system to adhere magnesium solid on the collection plate.

PULSED-LASER ABLATION

Firstly, a pulsed laser was used for causing the laser ablation of magnesia because of its enormous laser intensity enough to achieve the plume temperature to 4,000 K. The ablation plume was ejected from the magnesia sample by the laser irradiation. The ejected ablation plume containing produced magnesium atoms was cooled down by the argon gas blow, which caused the magnesium adhesion to the copper plate. As a result of the magnesia reduction by pulsed laser ablation, 43% of magnesium in the ablated magnesia adhered to the collection plate from the magnesia mass measurement using the chemical reaction with HCl aq. The energy consumption for magnesium production in the pulsed laser ablation method, E_{Mg}, was comparable to the value in the conventional magnesia reduction method. However, the ablation rate was much low due to the power limitation of the pulsed laser.

CONTINUOUS-LASER ABLATION

A continuous-wave (CW) laser was applied to the magnesia reduction method. The requirement on lasers will be significantly relaxed by applying a low-power CW laser to the laser ablation method. Moreover, the power input can be increased more easily than a pulsed laser. By the continuous laser ablation, the temperature of ablation plume ejected from a magnesia sample reached 5,000 K, which was higher than the boiling point of magnesia. Consequently, 99% of the magnesia in ablation plume was dissociated into magnesium and oxygen. The produced magnesium was cooled and adhered to a collection plate set above the ablation plume. The energy consumption for magnesium production in the laser ablation method was as small as the value of the conventional method. Moreover, the usage of silicon as a reducing agent was applied to the laser ablation method for magnesia reduction. As a result, the collection percentage was increased to lower the energy consumption.

This laser ablation method is applicable to the low-gravity environment because the laser beam and ablation plume are unaffected by gravity. Moreover, the pressurized environment can be established on the lunar surface by using a pressure vessel and sustainable ambient gas. Therefore, the laser ablation method is suitable for ceramics reduction toward the utilization of lunar resources on the Moon.

1.5.4 Alumina reduction by laser sustained plasma (LSP)

Thermal reduction of alumina powder by laser sustained plasma (LSP) was studied [49–51]. The LSP is generated and maintained by laser energy absorption through reverse bremsstrahlung. The center of LSP reaches a temperature of more than 10,000 K, which was expected to provide sufficient energy to reduce alumina powder [52–53]. The alumina reduction system consisted of a laser, an LSP generator, a nozzle, and an aluminum collection system: a copper tube with cooling water. Alumina powder at a mass rate of 10 mg/s passed through the LSP with argon gas flow to be heated and dissociated into aluminum atoms. The generated gas containing aluminum and oxygen atoms became a supersonic flow through the nozzle, a frozen flow in which no recombination occurs. The aluminum was expected to be cooled down through the copper tube in the frozen flow state and precipitate as aluminum solid on the tube wall.

As a result of the experiment, the line spectra of aluminum atoms were detected by emission spectroscopy of the supersonic flow. This result demonstrated that the alumina dissociation was successfully made. However, only a small amount of alumina powder went through the LSP because of the pressure gradient from the LSP. Results show that the alumina powder was not heated efficiently. The molar reduction percentage was estimated to $\eta_{\mathrm{re}} = 5.54\%$, which was calculated from comparing the intensity of the aluminum emission spectrum with that from the flow of aluminum powder instead of alumina.

For verifying the aluminum adhesion on the collection system, EDS (Energy Dispersive X-ray Analysis) was performed. As a result of the EDS analysis, a region where aluminum atoms exist but oxygen atoms are absent was detected, which indicated the aluminum adhesion on the cooling tube. Therefore, the aluminum collection from the supersonic Al-O flow was demonstrated by the water-cooled copper tube. Quantitative measurement of aluminum using hydrochloric acid was carried out, but hydrogen, which indicates the generation of aluminum, was not detected. This result indicated that the amount of collected aluminum was smaller than the measurement resolution due to the hydrogen detection limit.

1.5.5 Alumina reduction by laser ablation

PULSED-LASER ABLATION

Alumina reduction experiments by pulsed laser ablation were conducted [54]. A pulsed laser with pulse widths of 6-11 nm and a peak power of 4.0 MW was irradiated directly onto an alumina ball. The ablation plume was partially ionized and absorbed some laser energy by reverse bremsstrahlung. Therefore, the plume temperature was high enough for achieving a high molar reduction percentage: $\eta_{\mathrm{re}} = 99\%$. Argon was blown into the ablation plume from the side, encouraging adhesion of the produced aluminum to a copper plate placed on the side. After the experiment, the copper plate was inserted in the hydrochloric acid. The collected aluminum mass was estimated by measuring the volume of hydrogen gas produced by the chemical reaction of hydrochloric acid and aluminum. As a result, alumina was successfully reduced, and aluminum adhesion was confirmed. The mass of collected aluminum was measured to 0.23 mg in a laser irradiation period of 500 s and a peak power of 4.0 MW. The energy consumption for aluminum production was calculated to be $E_{\mathrm{Al}} = 19$ kWh/kg-Al, which is equivalent to the value in the conventional alumina reduction method. However, the ablation rate and aluminum collection rate were low, $\dot{m}_{\mathrm{ab}} = 2$ μg/s and $\dot{m}_{\mathrm{Al}} = 0.5$ μg/s respectively, because of the limitation of energy input by a pulsed laser, which is an issue to be addressed.

CONTINUOUS-LASER ABLATION

In this research, continuous laser ablation is used for alumina reduction instead of the pulsed-laser ablation. The laser ablation method using a CW laser is applicable to alumina reduction as well as to magnesia reduction. The laser ablation by a CW laser would achieve a large ablation rate because of the high laser energy input of a CW laser, which cannot be obtained by a pulsed laser. Moreover, the molar reduction percentage in the laser ablation method should be higher than the LSP heating method because the laser energy in laser ablation is directly absorbed by alumina. The laser intensity of a CW laser, which is supposed to affect the molar reduction percentage, is lower than the value of a pulsed laser. The ablation plume is non absorbable of the laser energy because of the low laser intensity. For these reasons, the molar reduction percentage in the laser ablation method using a CW laser would be lower than that using a pulsed laser. Considering the plume temperature in the magnesia reduction by continuous laser ablation was higher than the boiling point of magnesia, the molar reduction percentage in the alumina reduction by a CW laser is expected to be several tens of percent. Therefore, a large amount of aluminum collection rate would be obtainable by the laser ablation using a CW laser.

1.6 Problems in laser ablation method using a CW laser

The alumina reduction by the laser ablation method using a CW laser has problems in both processes of alumina dissociation and aluminum collection for obtaining high aluminum collection rate and low energy consumption to produce aluminum.

PROBLEM IN ALUMINA DISSOCIATION PROCESS

The alumina dissociation by laser ablation using a CW laser has not been demonstrated. The production of aluminum atoms by the laser ablation should be confirmed experimentally, even though the alumina dissociation at the temperature over the boiling point of alumina was predicted from the chemical composition calculation.

Moreover, maximization of aluminum production rate should be achieved for low energy consumption. However, the parameter dependencies of aluminum production rate by continuous-laser ablation have not been measured. The previous results of alumina reduction by a pulsed laser are inapplicable to the laser ablation method using a CW laser because the laser intensity varies by several orders depending on a pulsed or continuous-wave laser.

PROBLEM IN ALUMINUM COLLECTION PROCESS

High aluminum collection percentage is essential for achieving low energy consumption for aluminum production. The aluminum collection percentage in the laser ablation method using a CW laser would be low because of the relatively low molar reduction percentage than in magnesia reduction by a CW laser and alumina reduction by a pulsed laser. Therefore, the improvement of the aluminum collection system needs to be conducted. However, in the previous research of the laser ablation method, the collection process has not been discussed based on physical theories on the collection system. The elucidation of aluminum collection mechanisms is essential for improving the aluminum collection system.

1.7 Research objectives

The main objective of this study is establishment of an efficient alumina reduction method using laser ablation. The laser ablation method using a CW laser, which was demonstrated in the magnesia reduction, is expected to obtain a large aluminum collection rate. However, the alumina dissociation by continuous-laser ablation and the aluminum collection has not been demonstrated. Moreover, the metal collection from the ablation plume in the previous research has not been discussed based on physical theories on the collection system.

Therefore, to establish an efficient alumina reduction method using laser ablation, multiple objectives should be achieved in each process as follows.

OBJECTIVE IN ALUMINA DISSOCIATION PROCESS

1. Demonstration of alumina dissociation by laser ablation using a CW laser
2. Maximization of aluminum production rate by optimization of parameters

OBJECTIVE IN ALUMINUM COLLECTION PROCESS

3. Elucidation of aluminum collectible condition based on physical theories
4. Establishment of an efficient aluminum collection system

Finally, a comprehensive system evaluation of the alumina reduction method by laser ablation using a CW laser is conducted from the measured aluminum collection rate and energy consumption for aluminum production after achieving the objectives.

.

Chapter 2

Alumina dissociation by laser ablation

2.1 Background for alumina dissociation

2.1.1 Boiling of alumina with pressure dependence

The ablation plume, which is mainly composed of gas, does not absorb laser energy efficiently. For that reason, the plume temperature would be limited by the surface temperature of alumina rod. Considering the ablation is one of vaporization phenomena, the surface temperature should be affected by the boiling point of alumina. Therefore, the characteristics of alumina boiling point are critical to the alumina dissociation because the molar reduction percentage increases with plume temperature.

Boiling point decreases with ambient pressure according to Clausius-Clapeyron equation, Eq. (2-1).

$$\ln\left(\frac{P_{s1}}{P_{s2}}\right) = \frac{\Delta H_v}{R}\left(\frac{1}{T_2} - \frac{1}{T_1}\right) \qquad (2\text{-}1).$$

The calculated line of boiling point with various ambient pressures coincides with the line of $\eta_{re} = 0\%$ in the distribution map of molar reduction percentage because the alumina dissociation should start with alumina vaporization. The molar reduction percentage decreases with ambient pressure under the condition of constant plume temperature. The dependences of plume temperature and molar reduction percentage on ambient pressure are necessary to be compared for elucidating the effect of ambient pressure on alumina dissociation. Moreover, the increase of plume temperature from the boiling point of alumina is vital for obtaining a high molar reduction percentage. Therefore, the ambient pressure and laser intensity are critical parameters in the alumina dissociation.

2.1.2 Superheat with limitation temperature

Superheat is a metastable state in which a liquid is heated above the boiling point. Commonly, a liquid at a temperature of boiling point occurs boiling. However, the liquid without environmental change and bubbles, which become cores of gas, does not cause boiling. The liquid continues to be heated without boiling, resulting in superheating. The superheating state is unstable and suddenly boils with slight changes. The superheating phenomenon was experimentally confirmed by heating with little change [55].

Moreover, the enormous energy input can cause superheating. Previous research has reported the superheating state caused by laser ablation [56–57]. Therefore, in this study, the alumina rod surface and the ablation plume during laser ablation were supposed to be in the superheating state. Bubbles are generated from the superheated liquid around the dent on the heated surface. The high-energy molecules in the layer gather to expand the nucleus. As a result of the expansion, the superheated liquid layer generates a dome-shaped surface around the depression on the surface. When these bubbles become larger, they break through the superheated liquid layer and spout out, resulting in bumping.

The superheating state has the upper limit temperature because boiling can occur spontaneously without any bubble cores at high temperatures. This limit temperature is called superheat limit temperature. The superheat limit temperature can be estimated from Eq. (2-2) [58]. The critical temperature T_c, which is applied to Eq. (2-2), calculated from Guldberg law as shown in Eq. (2-3) [59].

$$T_{\mathrm{th}} \approx 0.9\,T_{\mathrm{c}} \qquad (2\text{-}2).$$

$$T_{\mathrm{c}} \approx 1.5\,T_{\mathrm{b}} \qquad (2\text{-}3).$$

The estimated values of superheat limit temperature of water and ethanol were matched to the experimentally measured values: 305°C of water and 201°C of ethanol [55]. In the case of alumina, the superheat limit temperature is estimated from Eqs. (2-2) and (2-3) to about 4,400 K.

In this research, the plume temperature should be increased to the superheat limit temperature of alumina for obtaining a high molar reduction percentage. For this achievement, high laser intensity and low heat loss at the laser spot are necessary. Therefore, the laser intensity, preheating temperature and laser spot occupancy, the area ratio of the laser spot to alumina rod surface, are important parameters. Moreover, these parameters should affect the ablation rate. The dependence of aluminum production rate on these parameters should be elucidated.

2.1.3 Objective of this chapter

This chapter aims to demonstrate the alumina dissociation by laser ablation using a CW laser and optimize the aluminum production rate in the alumina dissociation process. Emission spectroscopy was applied to detect aluminum atoms in the ablation plume. Moreover, the dependence of aluminum production rate on various parameters was verified by the measurements of ablation rate and plume temperature and the observation of ablation plume. In this study, the parameters were ambient pressure, preheating temperature, laser intensity, and laser spot occupancy.

2.2 Alumina dissociation system using a CW laser

2.2.1 Laser ablation under various ambient pressures

A schematic of the experimental setup is depicted in Figure 2-1. A CW CO_2 laser, YB-2000B7 by Panasonic, was used for the laser ablation of alumina. The laser power was 0.40–2.0 kW at a wavelength of 10.6 μm. The laser transverse mode was TEA (Transversely Excited Atmospheric) and its beam shape was TEM_{10}. The laser beam was expanded through a beam expander and was focused on a sintered alumina rod in a test chamber by a ZnSe convex lens. The focal length of ZnSe lens for the CW CO_2 laser was 190 mm. The laser energy loss through the optical system could be ignored because of the high laser transmittance of ZnSe window and lens with AR coating: over 99.9%. This 4-mm-diameter sintered alumina rod was inserted into a copper plate holder to prevent destruction because of the rapid heat input and drastic thermal gradient. The laser spot size on the alumina rod surface was 0.49 mm. The laser intensity was changed from 0.51 GW/m^2 to 2.6 GW/m^2, corresponding to laser power of 0.40 kW to 2.0 kW. The laser irradiation period was 1.0 s. The chamber was evacuated using a rotary pump during the experiment to remove oxygen. The ambient pressures were 0.30 atm, 0.50 atm, and 1.0 atm, which were controlled by changing argon mass flow rate into the chamber. The video camera was set at frame rates of 30 fps for the observation of ablation plume and 2,400 fps for the measurements of plume expansion speed. The mass change of the sintered alumina rod was measured using an electronic balance in a resolution of 0.1 mg. The experiments were conducted three times for one combination of laser intensity and ambient pressure.

2.2.2 Emission spectroscopy of an ablation plume

IDENTIFICATION OF ATOM AND MOLECULE FROM LINE SPECTRUM

To detect aluminum atoms generated from alumina dissociation in the ablation plume, emission spectroscopy of the plume was conducted. By the energy transition from a high to a low energy level, atoms and molecules emit light with a wavelength corresponding to the difference between the two energy levels. The substance of emission source can be

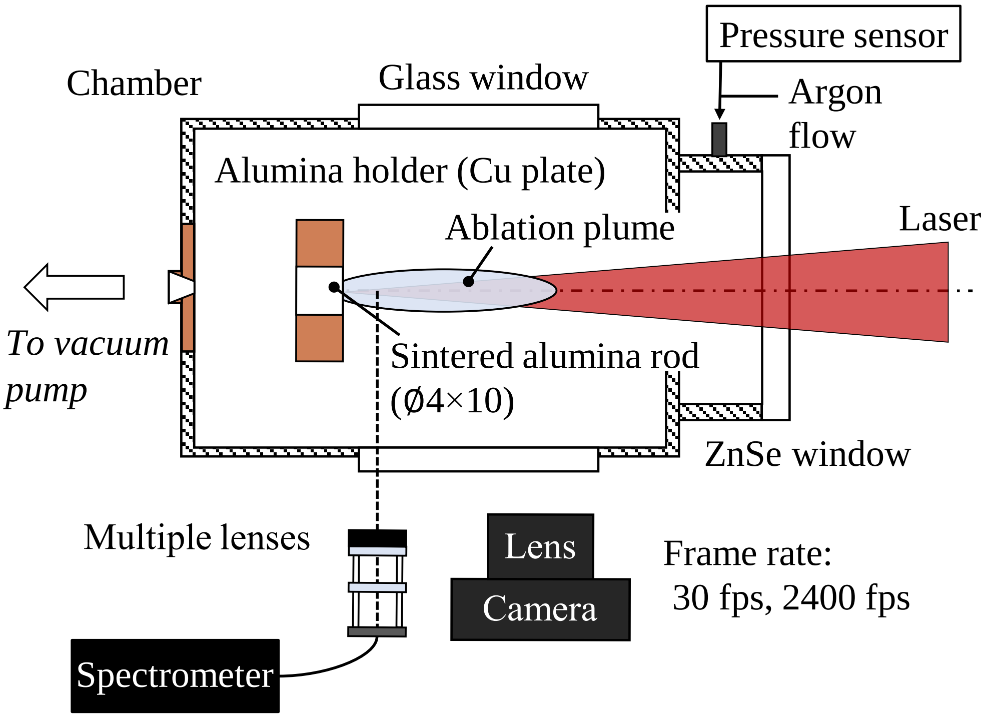

Figure 2-1 Alumina dissociation system using a CW CO_2 laser for laser ablation.

identified from the emission wavelength because the energy levels are unique to the substance. The atomic spectra of Al I have wavelengths of 396 nm, 394 nm, and 309 nm [60]. In this research, the measurement point was set at 5 mm from the alumina rod surface.

TEMPERATURE MEASUREMENT FROM BLACK BODY RADIATION

The plume temperature was estimated by application of curve fitting of Planck's law, using least-squares method for the black body radiation from solid or liquid particles in the ablation plume. The black body radiation is thermal radiation from the black body. The emission intensity of black body radiation depends on temperature and wavelength of emission as shown in Eq. (2-4), Planck's law.

$$I(\lambda, T) \propto \frac{2hc^2}{\lambda^5} \frac{1}{\exp\left(\frac{hc}{\lambda kT}\right) - 1} \tag{2-4}.$$

Under the assumption that the ablation plume was gray body, the temperature of ablation plume, which contained particles at the state of liquid or solid, can be measured by application of curve fitting of Planck's law to the continuous spectrum. The measured emission spectrum was calibrated with a standard light source of halogen lamp. The uncertainty was about 0.3% due to the random noise. Considering that the ablation plume has not been demonstrated to be gray body, the measured temperature could be different from the plume temperature. In this paper, the plume temperature was assumed to be equal to the temperature measured from the Planck curve fitting to the continuous spectrum.

2.2.3 Alumina rod preheating

The experiment of laser ablation with the alumina rod preheating was conducted with a different experimental setup from the previous setup in Figure 2-1. A schematic and photograph showing the experimental setup of preheating and laser ablation are presented in Figure 2-2 and Figure 2-3. A 4-mm diameter sintered alumina rod was inserted into a tantalum coil-shaped holder and was heated to 1,500–2,300 K using a semiconductor laser (976 nm wavelength) with 50–70 W power. The semiconductor laser was JOLD-250-CPXF-2P2 (JENOPTIK co.). The laser beam for rod preheating was irradiated through a collimator and a lens at a focal length of 125 mm. The laser spot size of the semiconductor laser on the alumina rod surface was 2.0 mm by controlling the lens position for the semiconductor laser. Figure 2-2 shows that the surface temperature of the sintered alumina rod was measured by application of Planck's law to the emission spectrum obtained at position A.

After alumina rod preheating, a CW CO_2 laser with 0.40–2.0 kW power was irradiated to the sintered alumina rod for 1.0 s. The semiconductor laser for alumina rod preheating was turned off at the beginning of laser ablation. The focal length of ZnSe lens for the CW CO_2 laser was 210 mm. The laser spot size on the alumina rod surface was 0.54 mm. The mass flow rate of argon gas was 6.0 slm. The ambient pressure in the test chamber was controlled to 1.0 atm. The ablation plume emission spectrum was measured using multiple lenses at position B in Figure 2-2 to measure the plume temperature.

a) Preheating

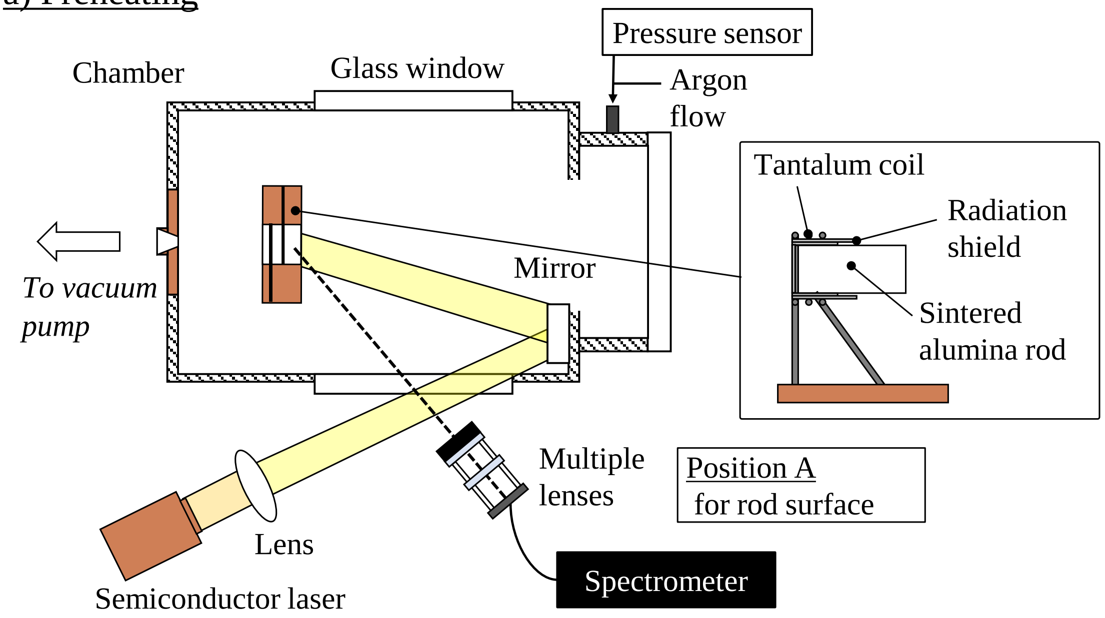

b) Laser ablation

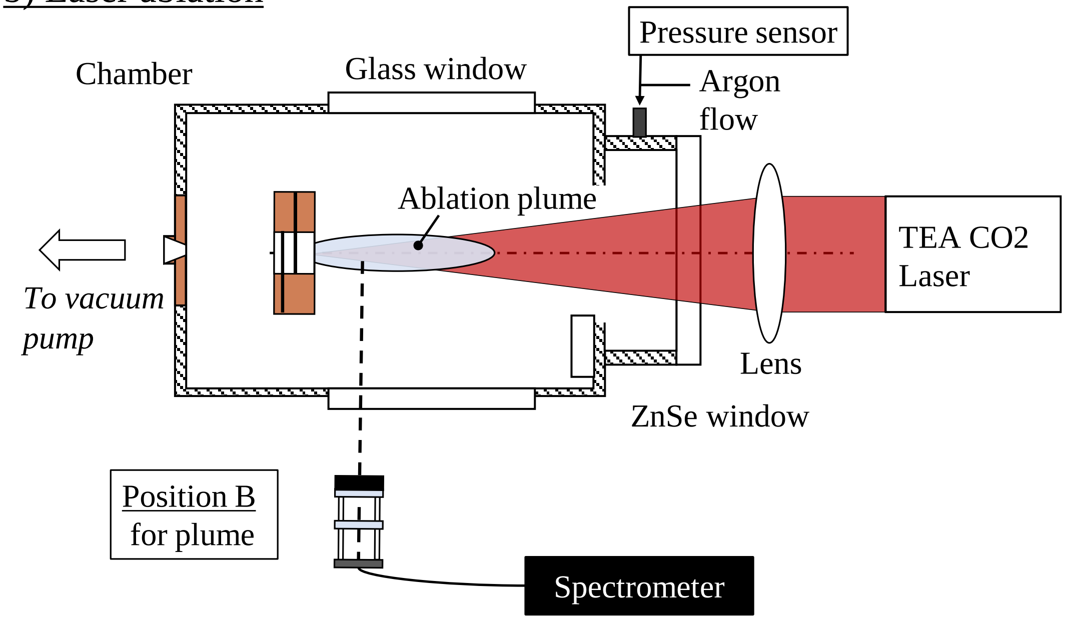

Figure 2-2 Alumina preheating and reduction system using a semiconductor laser for preheating (a) and TEA CO_2 laser for laser ablation (b).

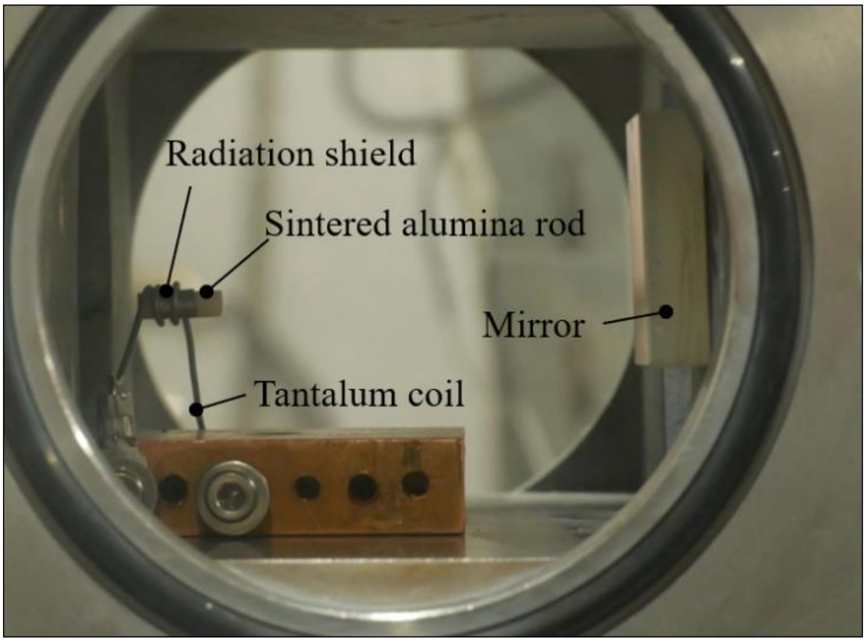

Figure 2-3 Photograph of the sintered alumina rod inserted into the tantalum coil holder in the test chamber.

2.2.4 Variation of laser spot sizes on alumina rods

The experimental schematic was the same as the alumina rod preheating experiment, as shown in Figure 2-2. The laser spot size on the alumina rod, which was changed by controlling the CO_2 laser lens position, was varied according to the beam waist size, as 0.49– 2.0 mm. The laser spot size at various lens positions was calculated from Eqs. (2-5) and (2-6) for obtaining the required laser spot size [61].

$$r_W = \frac{4\lambda f M^2}{\pi} \tag{2-5}$$

$$r_L(z) = r_W \sqrt{1 + \left(\frac{M^2 \lambda z}{\pi r_W^2}\right)^2} \tag{2-6}$$

The calculated laser spot size at various distances from the focal point is presented in

Figure 2-4. The lens position was determined by using the calculated results. The alumina rod radius was 1.5–2.0 mm. Therefore, the laser spot occupancy α was 0.060–1.0. In the experiment with various laser spot sizes, the preheating temperature T_{pre} was 1,500 K, and the ambient pressure in the test chamber was 1.0 atm. The laser intensity was changed from 0.032 GW/m^2 to 2.7 GW/m^2, corresponding to 0.40–2.0 kW laser power and 0.49–2.0 mm laser spot size. The laser irradiation period was 1.0 s.

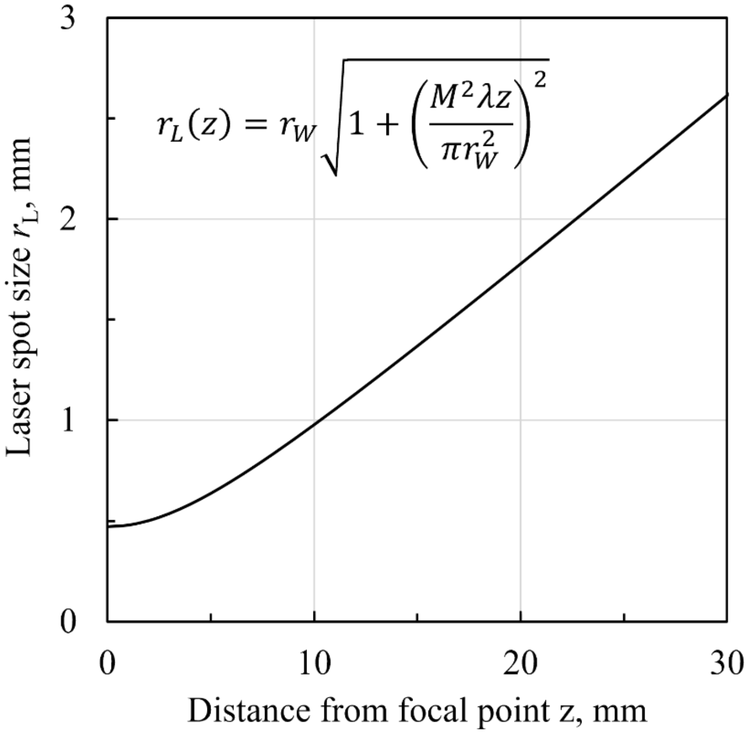

Figure 2-4 Laser spot size at various distances from focal point.

2.3 Detected aluminum atom existence in the ablation plume

Figure 2-5 presents the emission spectrum from an ablation plume under 1.0–1.2 atm ambient pressure and 0.51 GW/m^2 laser intensity. A combined Al I spectrum of 394 nm and 396 nm was observed, which indicates the existence of aluminum atoms in the ablation plume. Therefore, the alumina dissociation by the laser ablation using a CW laser was demonstrated. The aluminum monoxide molecules were also detected from molecular emission spectra observed at wavelengths of 450–550 nm. The line spectra of sodium and potassium were detected. These substances were contained in the sintered alumina rod. In addition to the atomic and molecular spectra, a continuous spectrum stemming from black body radiation was observed. Figure 2-5 shows the Planck curve fitting line to the continuous spectrum at a temperature of 3,450 K.

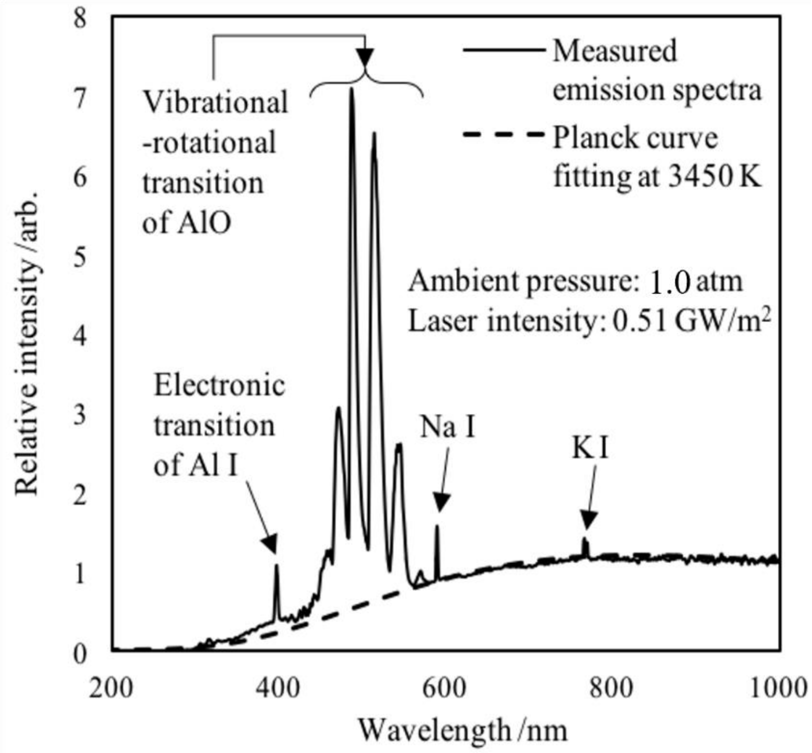

Figure 2-5 Measured emission spectrum from an ablation plume with a Planck curve fitting line.

2.4 Measured aluminum production rate

2.4.1 Pressure dependence

ABLATION PLUME

The sintered alumina rod was found to have been hollowed out via laser ablation. The ablation plume appearance during laser irradiation varied according to the ambient pressure as shown in Figure 2-6. At 0.0 atm, only particle ejections were observed. First, the sintered alumina rod melted from the laser irradiation spot. The liquid alumina formed a hemisphere on the surface. It started to boil. Alumina particles were ejected. This particle ejection resulted from the thermal expansion of the gas included in the sintered alumina rod. In the argon ambient, this phenomenon was also observed during the first 0.02 s. After that period, however, the ablation plume was ejected continuously until the laser irradiation ended in the argon ambient at 0.40 atm, 0.65 atm and 1.2 atm, which was not observed in 0.0 atm. By measuring the ablation plume expansion with the camera (2,400 fps), results showed that the expansion speed was 2.7–6.6 m/s, decreasing with ambient pressure (Table 2-1).

ABLATION RATE

The mass change during the particle ejections was measured as 0.40 mg. The particles were assumed to be a liquid or solid state of alumina ejected by boiling and thermal destruction. Therefore, the ablation rate was defined as the mass change per second during ejection of the ablation plume; 0.40 mg was excluded from calculation of ablation rate.

The results of ablation rate measurements are portrayed in Figure 2-7. The respective parameters were the ambient pressure and laser intensity. The error bars represent standard deviations of three measurements. The ablation rate was unaffected by ambient pressure, but it increased monotonically with laser intensity. An ablation rate of 8.9 kg/m^{2}s was obtained at 2.6 GW/m^2.

MOLAR REDUCTION PERCENTAGE

Figure 2-8 presents the plume temperatures estimated for different ambient pressures and laser intensities. The plume temperature varied (3,100–3,850 K), increasing with ambient pressure and laser intensity. This ambient pressure dependence would be attributable to the boiling point of alumina, which increases with ambient pressure, as described in Section 2.1.1. Liquid or solid alumina can absorb laser energy efficiently. Therefore, at higher ambient pressure, alumina can reach higher temperatures.

The molar reduction percentage was calculated for this experiment by application of the plume temperature to Figure 1-4. The energy consumption for aluminum production in the alumina dissociation process was calculated from the ablation rate and molar reduction percentage. Table 2-2 and Table 2-3 respectively present results of the molar reduction percentage and energy consumption for aluminum production for different ambient pressures and laser intensities. The molar reduction percentage of η_{re} = 13% was obtained in 1.0 atm and 2.6 GW/m^2, which is higher than the amounts of approximately 5% found in past studies using LSP heating. Energy consumption for aluminum production in the alumina dissociation process of $E_{\mathrm{Al}}\eta_{\mathrm{co}}$= 3.1 MWh/kg-Al was obtained in 1.0 atm and 2.6 GW/m^2. This value is two orders of magnitude larger than that of the molten salt electrolysis method because of the limitations imposed by reachable temperatures. Sintered alumina rods could not be heated enormously above the alumina boiling point by laser heating because alumina vapor does not absorb laser energy. Therefore, the molar reduction percentage would not be high.

Table 2-1 Measured ablation plume expansion speeds at various ambient pressures.

Ambient pressure /atm	Expansion speed of ablation plume /(m/s), u
1.0–1.2	2.7
0.50–0.65	4.3
0.30–0.40	6.6

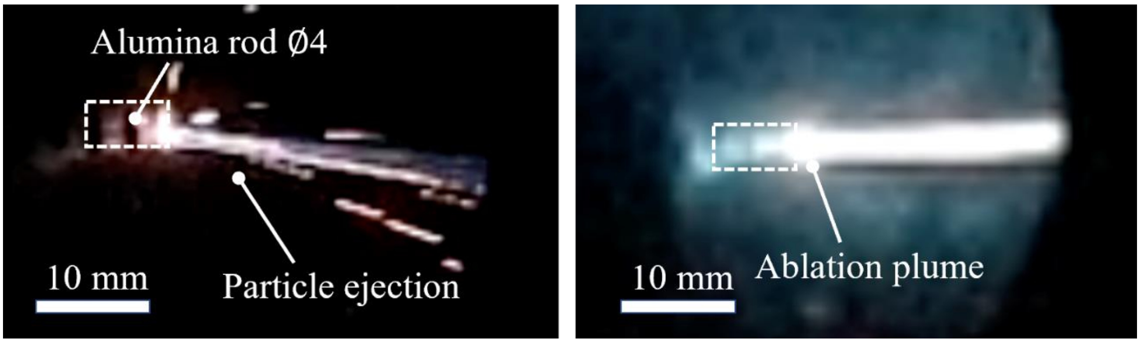

Figure 2-6 Particle ejection observed at 0 atm (left) and ablation plume observed at 0.30–1.0 atm in Ar flow (right): the laser was irradiated from the right; the ablation plume expanded to the right.

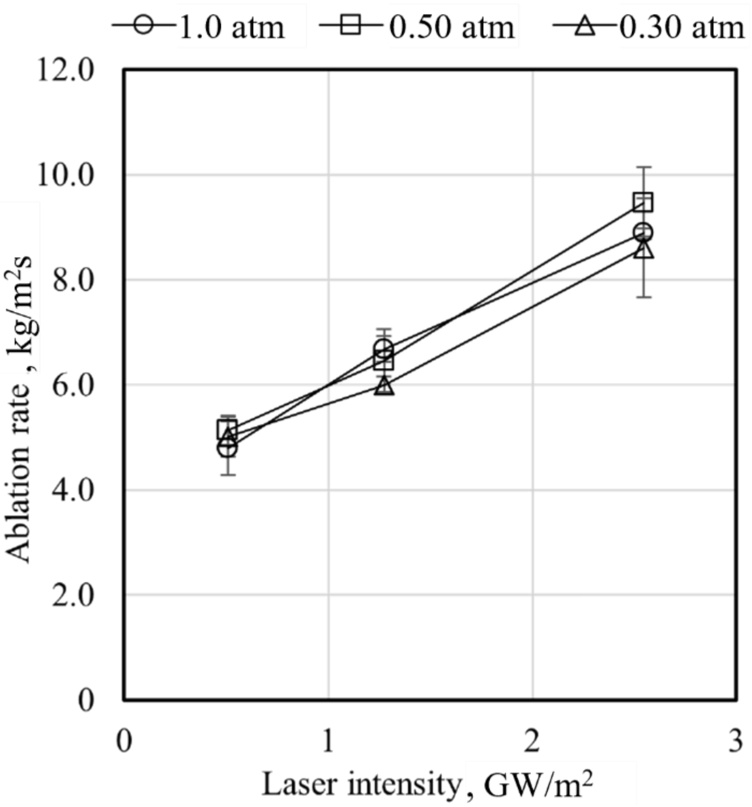

Figure 2-7 Measured ablation rate at various ambient pressures and laser intensities without alumina rod preheating.

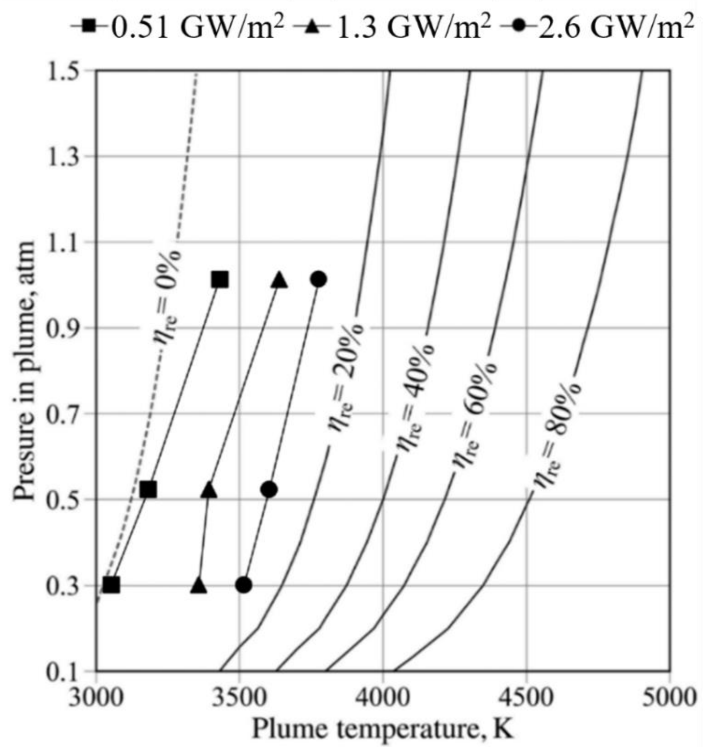

Figure 2-8 Estimated plume temperature at various ambient pressures and laser intensities.

Table 2-2 Molar reduction percentage and energy consumption with various ambient pressures at a laser intensity of 0.51 GW/m^2.

Ambient pressure /atm	Molar reduction percentage	Energy consumption for aluminum production, $E_{Al}\eta_{co}$ /(MWh/kg)
1.0–1.2	3.0%	3.7
0.50–0.65	1.6%	7.2
0.30–0.40	1.4%	8.1

Table 2-3 Molar reduction percentage and energy consumption with various laser intensities at ambient pressure of 1.0 atm.

Laser intensity /(GW/m^2)	Molar reduction percentage	Energy consumption for aluminum production, $E_{Al}\eta_{co}$ /(MWh/kg)
0.51	3.0%	3.7
1.3	7.5%	2.7
2.6	13%	3.1

2.4.2 Preheating temperature dependence

ABLATION PLUME

Figure 2-9(a) is a photograph of the sintered alumina rod during the preheating process. The alumina surface emitted intense light sufficient to measure the preheating temperature from the emission spectrum. After the preheating process, the CW CO_2 laser beam was irradiated to the sintered alumina rod to cause laser ablation. The ablation plume was ejected continuously until laser irradiation was completed, as presented in Figure 2-9(b). Spallation, which was observed in the earlier experiments without preheating, did not occur. This result shows that alumina preheating avoided spallation and enabled accurate measurement of the ablation rate. Moreover, the alumina rod surface transformed into a sphere by laser irradiation. The dome shape was maintained after laser ablation, as Figure 2-10 presents. The substances of a black part in the alumina rod was estimated to oxygen-deficient alumina.

ABLATION RATE

Figure 2-11 presents results of measurements of the alumina mass rate of change with various preheating temperatures. The error bars represent plus or minus standard deviations. With alumina preheating, the alumina mass rate of change decreased because alumina spallation was prevented during laser ablation. The alumina mass rate of change with preheating can be regarded as the ablation rate. The ablation rate was unaffected by the preheating temperature, but it increased with laser intensity.

MOLAR REDUCTION PERCENTAGE

Figure 2-12 presents the plume temperature estimated for different laser intensities for ablation and alumina preheating temperatures (1,500–2,300 K and no preheating). The error bars represent standard deviations of three measurements. With alumina preheating, the plume temperature was increased up to T = 4,100 K, which was higher than the temperatures obtained without alumina preheating. This result indicates that preheating of the sintered alumina rod increased the plume temperature. The molar reduction percentage calculated by application of the plume temperature to Figure 1-4 was η_{re} =

32%, which is a higher percentage than the η_{re} = 13% obtained without alumina preheating. Moreover, Figure 2-12 shows that the plume temperature measured in the preheating experiments was unaffected by the laser intensity and preheating temperature, but that in experiments with no preheating increased with laser intensity. This result suggests limitations of the plume temperature.

The change of plume temperature with time passing is depicted in Figure 2-13. The error bars represent standard deviations of three measurements. The plume temperature was constant during the laser ablation. This result indicates the increase of plume temperature by alumina rod preheating was not only the beginning of laser ablation. By the alumina rod preheating, the surface temperature would be increased to over 4,100 K at the beginning of laser ablation. The high surface temperature would be kept by the input energy of laser beam with compensating for energy loss of vaporization.

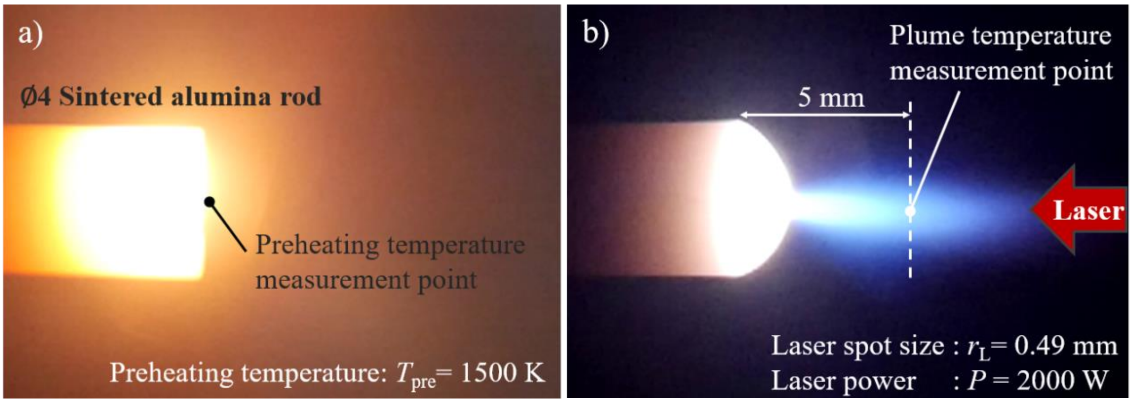

Figure 2-9 Images of the sintered alumina rod in the preheating experiments: a) the alumina rod in the preheating and b) ablation plume ejected from the rod surface.

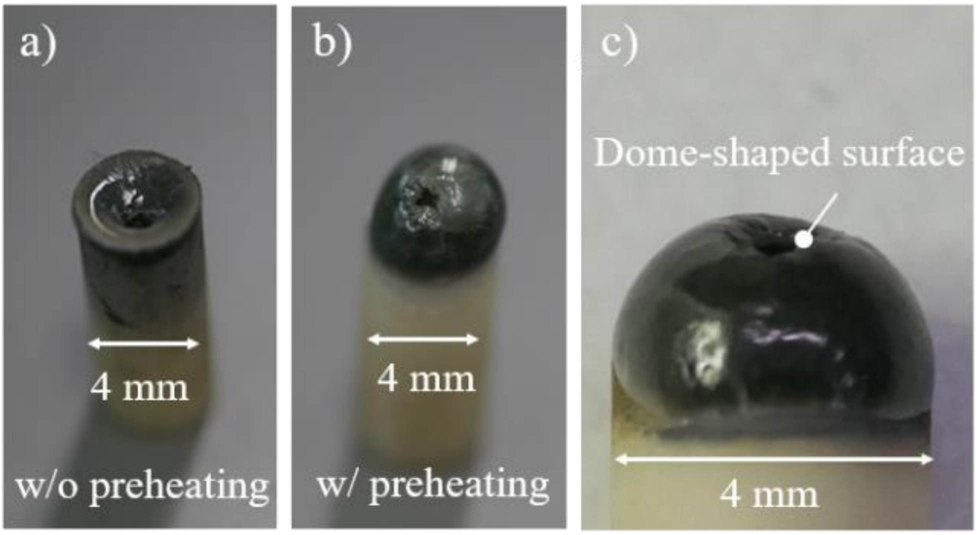

Figure 2-10 Photographs of a sintered alumina rod after laser ablation: a) without preheating, and b) and c) with preheating.

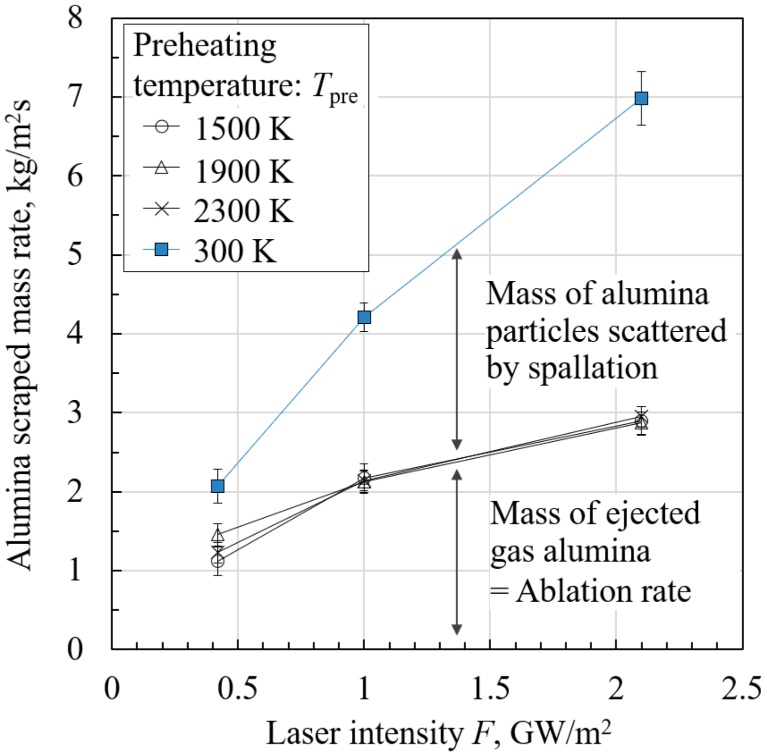

Figure 2-11 Alumina mass rate of change with various preheating temperatures. By alumina preheating, the alumina mass rate of change was decreased because alumina rod spallation was prevented.

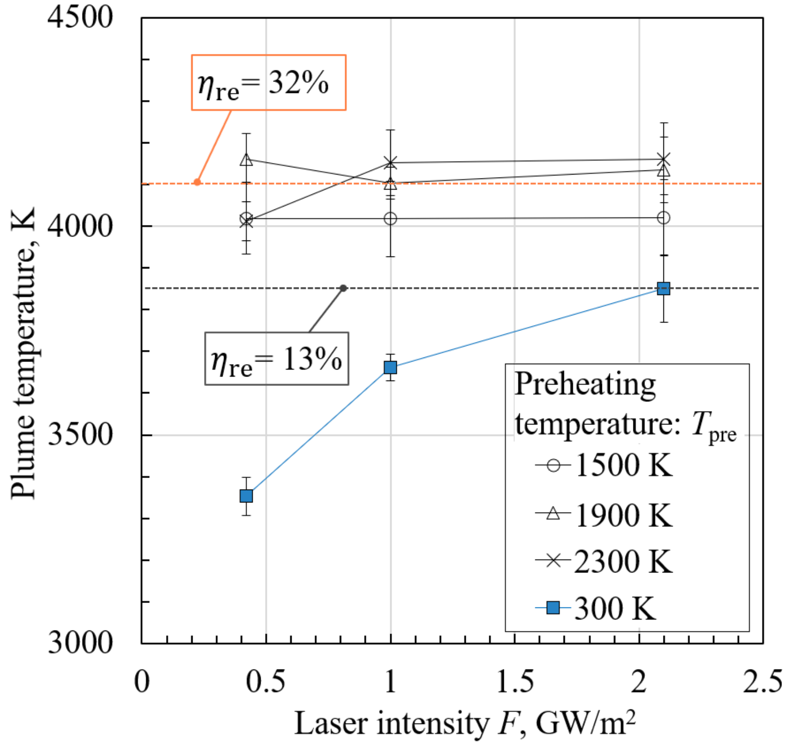

Figure 2-12 Measured plume temperature vs. laser intensities at various preheating temperatures.

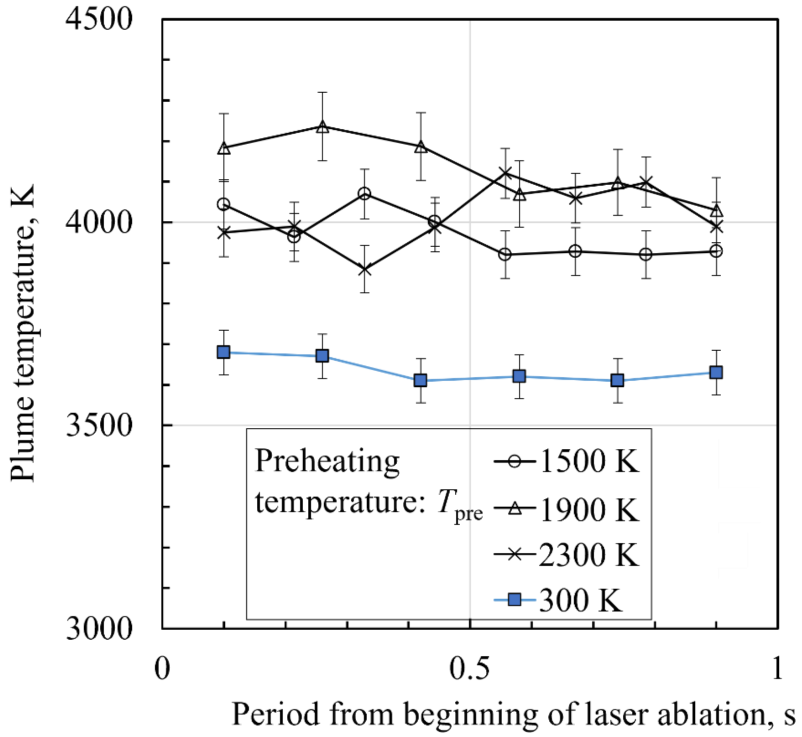

Figure 2-13 Measured plume temperature vs. laser intensities at various preheating temperatures.

2.4.3 Laser intensity and laser spot occupancy dependences

ABLATION PLUME

Photographs of ablation plumes with various laser spot sizes are presented in Figure 2-14. The ablation plume was expanded by laser spot size enlargement. The ablation plume radius was approximately equal to the laser spot size. Therefore, by application of the large laser spot size, the outer cooling part of the ablation plume caused by entrainment of the argon ambient would be decreased.

Under conditions of laser spot size r_L of 2.0 mm and 0.40–1.0 W laser power, and 1.4 mm and 0.50 W, the ablation plume was not ejected because the laser intensity was not sufficiently large to cause the laser ablation. This result indicates the threshold value of laser intensity causing the alumina laser ablation (F) as approximately 0.080 GW/m^2.

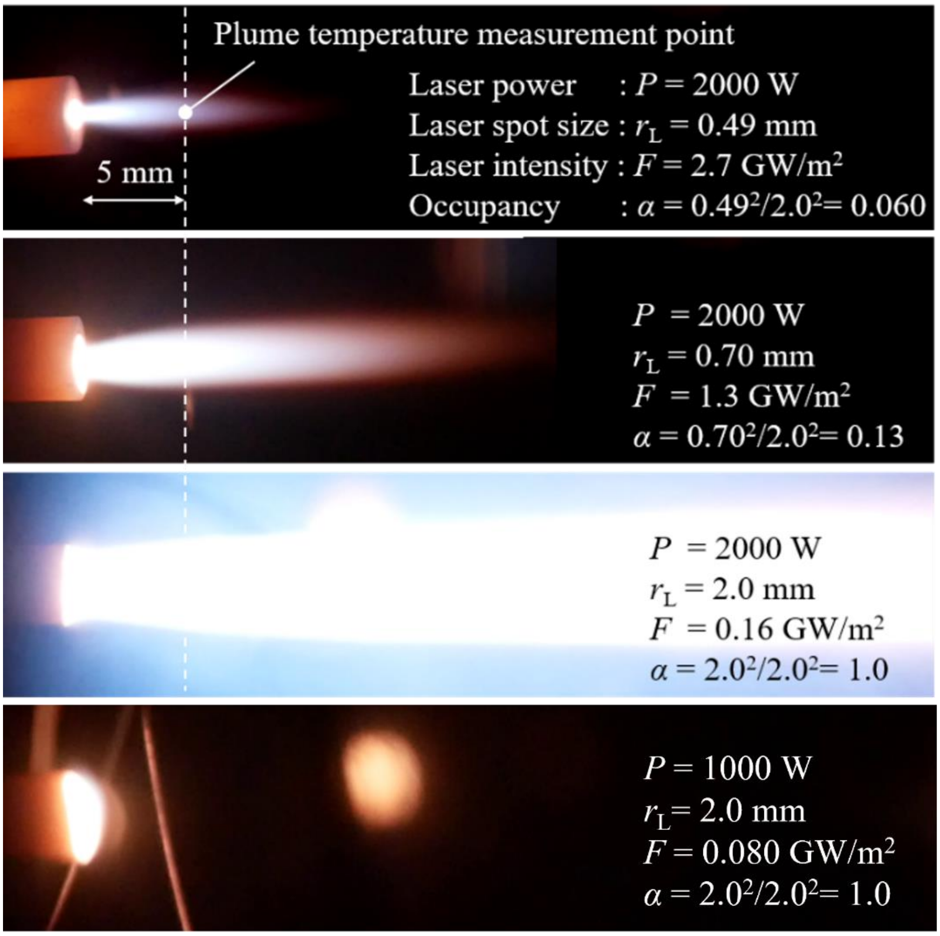

Figure 2-14 Photographs of ablation plumes with various laser spot sizes for r_L = 0.49–2.0 mm.

ABLATION RATE

Figure 2-15 presents the measured ablation rate per unit area for different occupancies. The error bars represent standard deviations of three measurements. The ablation rate per unit area was the quotient of the ablation rate divided by the area of the laser spot. The ablation rate per unit area increased monotonically with the laser spot occupancy.

MOLAR REDUCTION PERCENTAGE

Results of plume temperature measurements are portrayed in Figure 2-16. The error bars represent standard deviations of three measurements. The plume temperature T was unaffected by the laser intensities; it reached 4,090 ± 90 K. this should be the effect of rod preheating. The plume temperature results showed that the molar reduction percentage estimated from Figure 1-4 was $\eta_{\mathrm{re}} = 31.7 \pm 3.7\%$, which was smaller than the percentage in the pulsed laser ablation method: $\eta_{\mathrm{re}} = 99\%$. For further improvement of molar reduction percentage, the plume temperature needs to overcome the temperature limitation.

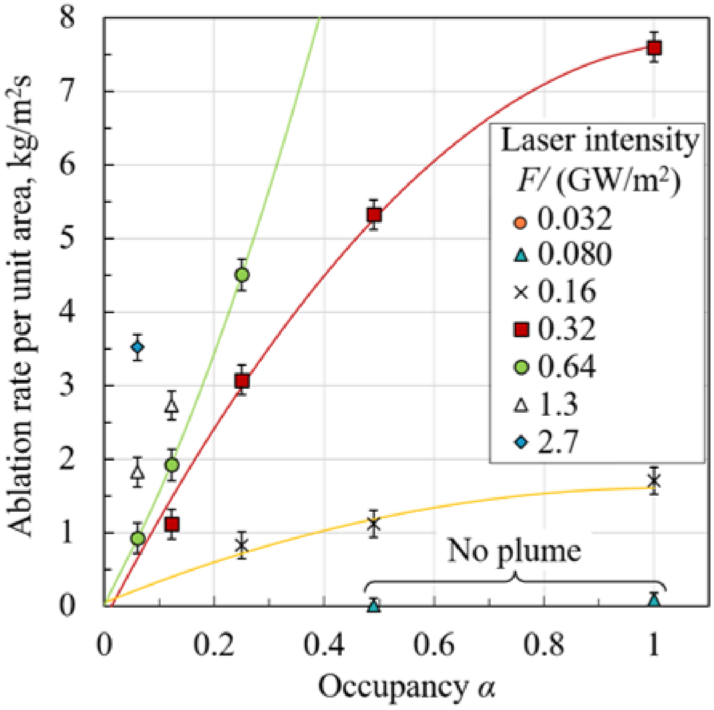

Figure 2-15 Ablation rate per unit area vs. laser spot occupancy (area ratio of laser spot to alumina rod surface) at various laser intensities.

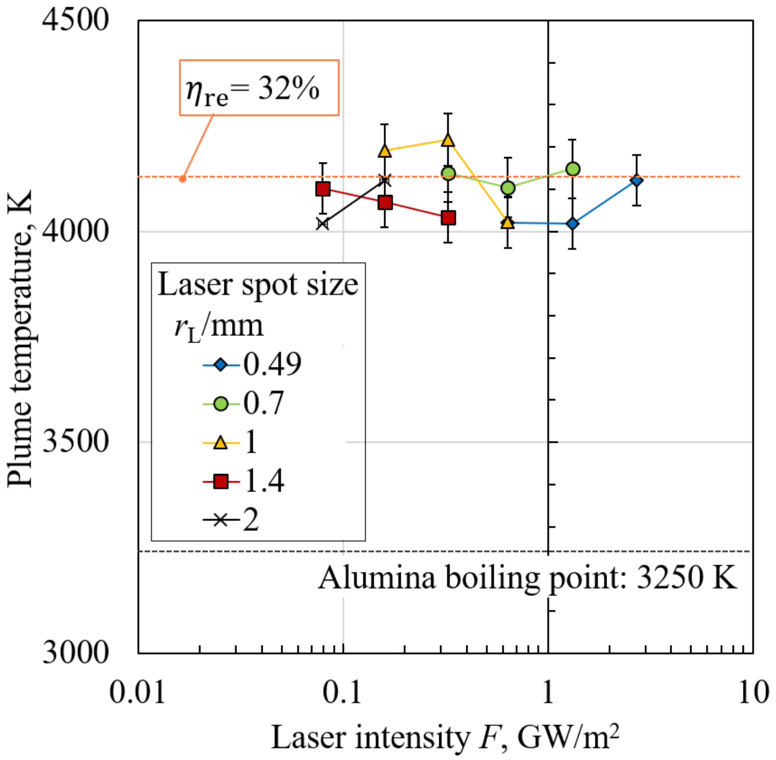

Figure 2-16 Plume temperature vs. laser intensity at various laser spot sizes r_L = 0.49–2.0 mm. The plume temperature achieved the limit temperature, T = 4,100 K.

2.5 Evaluated energy consumption for aluminum production in dissociation

From the results of the ablation rate and molar reduction percentage measurements, the maximum aluminum production rate was measured to 7.6 mg/s in $F = 0.32$ GW/m^2 and laser spot occupancy $\alpha = 0.91$. Therefore, the minimum value of $E_{\mathrm{Al}}\eta_{\mathrm{co}} = 73 \pm 8.4$ kWh/kg-Al was obtained, which is two orders of magnitude smaller than the earlier result obtained without alumina preheating and laser spot size optimization. This energy consumption in the laser ablation method was about twice as large as the value in the inert anode method: 20–50 kWh/kg-Al. However, considering the energy to generate laser and electricity, the laser ablation method becomes comparable with the molten salt electrolysis. A solar pumped laser, which oscillates a laser beam directly by using solar power, has high energy transition efficiency of 30–40%. This value is about twice as large as the power generation efficiency of solar cell: approx. 15–20%.

2.6 Discussion

2.6.1 Calculation of number density in the ablation plume

The effect of the particle number density could be one reason for the decrease of plume expansion speed with ambient pressure. Particles surrounding the ablation plume interrupt the plume expansion in terms of advection. The greater the particle number density above the ablation plume, the stronger this effect would become, decreasing the expansion speed. For the quantitative discussion, the number density of ablation plume was calculated with various ambient pressures.

From the ablation rate and the expansion speed of the ablation plume, the ablation plume number density was estimated using Eq. (2-7) (Table 2-4).

$$n = \frac{\dot{m}_{ab} N_A}{M_{ave} A u} \qquad (2\text{-}7).$$

The number density in ablation plume was estimated from the equation of state as written in Eq. (2-8).

$$n = \frac{P}{kT} \qquad (2\text{-}8).$$

The pressure in the ablation plume *P* was thought equal to the ambient pressure because the plume extended in parallel. As shown in Table 2-4, the estimated number densities in the ablation plume roughly coincided. This consistency demonstrates the validity of the measured expansion speed of the ablation plume. The difference between the two estimated number densities suggests the existence of argon in the ablation plume.

The results imply that the particle number density of Al and AlO in the ablation plume increased with ambient pressure. Concomitantly with the particle number density, the light emission from ablation plume increased. Therefore, the emission from the plume was weak at 0 atm compared with cases having high ambient pressure.

Table 2-4 Estimated number densities at various ambient pressures.

Number density in the ablation plume /(10^{24} /m^3) , *n*	
Estimated from the plume expansion speed, Eq. (2-7)	Estimated from the equation of state, Eq. (2-8)
1.5	2.6
0.96	1.5
0.67	0.97

2.6.2 Plume temperature limitation considering superheat state

The alumina rod surface would be in superheat state. The dome shape seems to have been produced by bubble formation in the superheated liquid layer. The alumina rod surface was heated to superheated liquid by laser ablation. Some bubbles were generated spontaneously in the expanded layer, producing the dome-shaped surface. Therefore, the dome shape indicates that the rod surface was in superheat state, whose temperature was much higher than the 3,250 K boiling point of alumina.

The ablation plume ejected from the superheated alumina rod surface was estimated as a state of superheating because the ablation plume was heated beyond the boiling point of alumina: 3250 K. The measured plume temperature with the alumina rod preheating, T= 4,100 K, was approximately equal to the estimated superheat limit temperature of alumina: $T_{\mathrm{th}} \approx$ 4,400 K. Moreover, the measured plume temperature was consistent with the calculated values considering superheating of alumina in the previous research [62]. Therefore, the limitation of plume temperature would be the superheat limit temperature of alumina. This could be the reason why the tendency of the plume temperature to increase concomitantly with the laser intensity did not appear. For overcoming the superheat limit temperature, a few orders of magnitude larger laser intensity than the values applied in the experiments would be required as reported in the previous research.

2.6.3 Estimation of ablation rates at various laser intensities and laser spot occupancies

From the results of the ablation rate per unit area measurements, the ablation rate in any conditions of laser power, laser intensity, and laser spot occupancy can be estimated. The ablation rate can be calculated by ablation area and ablation rate per unit area, which were determined by laser spot size, laser intensity, and laser spot occupancy. The laser spot size is uniquely decided according to a combination of laser intensity and laser spot occupancy at fixed laser power condition. Therefore, the ablation rate at any conditions of laser power can be estimated at various laser intensity and laser spot occupancy.

Figure 2-17 portrays the ablation rate map for $P_{\mathrm{Laser}} = 2.0$ kW with three representative examples. Table 2-5 shows detailed values of three conditions: A) the smallest laser spot occupancy in this experiment, B) optimized laser intensity, and C) optimized laser intensity and laser spot occupancy. This distribution map shows that the maximum ablation rate is obtained at laser intensity $F = 0.32$ GW/m^2 and laser spot occupancy $\alpha = 1$, corresponding to laser spot size $r_{\mathrm{L}} = 1.4$ and alumina rod radius $r_{\mathrm{a}} = 1.4$ mm. In this experiment, the maximum ablation rate of $\dot{m}_{\mathrm{ab}} = 45.2 \pm 1.3$ mg/s was obtained at laser intensity $F = 0.32$ GW/m^2 and laser spot occupancy $\alpha = 0.91$. For higher laser intensity than $F = 0.32$ GW/m^2, the ablation rate was less than the maximum value because the laser spot size was small despite a high ablation rate per unit area.

Table 2-5 Values obtained for three calculated conditions: A) the lowest laser spot occupancy in this experiment, B) optimized laser intensity, and C) optimized laser intensity and laser spot occupancy.

Legend	Laser spot occupancy	Laser intensity /(GW/m^2)	Ablation rate /(mg/s)	Molar reduction percentage
A	0.060	2.7	2.6 ± 0.31	31.9 ± 2.6%
B	0.49	0.32	34.2 ± 1.2	30.7 ± 3.2%
C	0.91	0.32	45.2 ± 1.3	31.5 ± 3.5%

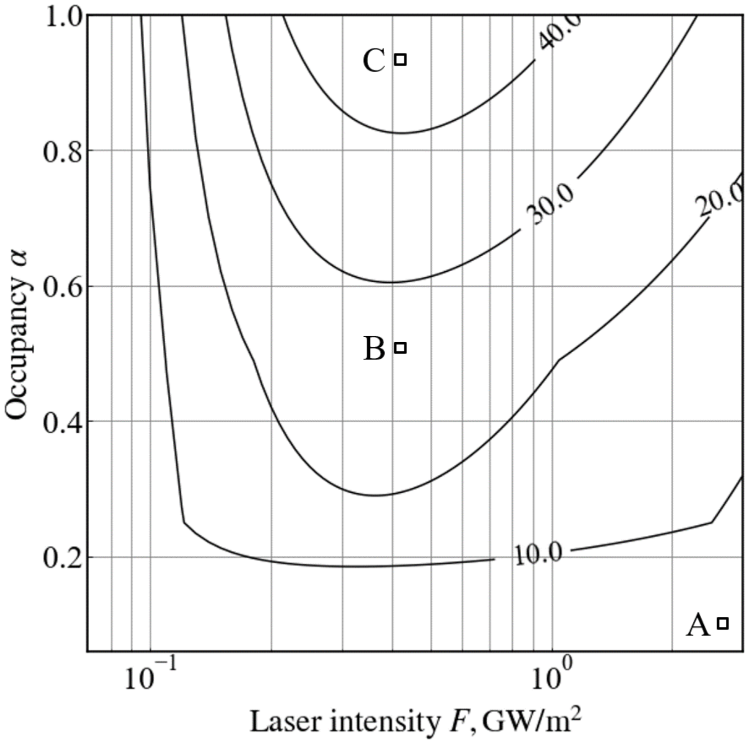

Figure 2-17 Ablation rate map with 2.0 kW laser power in various laser intensities and occupancies (i.e., the area ratio of laser spot to alumina rod surface).

2.6.4 Input energy distribution

The radial heat conduction loss in the sintered alumina rod could be one of advantages of laser spot size optimization. In earlier research reported by Jamdeleit et al. [63–65], the heat conduction loss in pulse laser ablation of the ceramics plate was measured as 20–50%. Reducing the energy loss is expected to affect the ablation rate strongly. Therefore, a high ablation rate per unit area was obtained by increasing the laser energy consumed for alumina ablation.

The energy distributions of this system were calculated for three conditions: A, B, and C in Table 2-5. The input energy was used for ablation, dissociation, and thermal loss, which includes thermal conduction and thermal radiation. The energy balance is described as Eq. (2-9).

$$P_{Laser} = \dot{m}_{ab}(c_{heat}\Delta T + E_m + E_b + E_d) + P_{loss} \qquad (2\text{-}9).$$

The heat of melting and vaporization of alumina is E_m= 109 kJ/mol [66] and E_b= 467 kJ/mol [67]. The dissociation energy was calculated from the change of the enthalpy at the temperature of boiling point. The calculated energy distributions are presented in Figure 2-18. Results showed that, at the smallest laser spot occupancy (legend A in Figure 2-18), the energy for ablation was 0.9%, but that for dissociation was 3.4% of the laser power. In all, only 4.3% of the input energy was used for the heating and dissociation of alumina. At optimized laser intensity (legend B), however, the energy for ablation was 12%; that for dissociation was 53%. The alumina reduction, the sum of ablation and dissociation, increased to 65% from 4.3%. This result implies that laser spot size optimization decreased the radial heat conduction. Moreover, at optimized laser intensity and laser spot occupancy (legend C), the total energy for alumina reduction was estimated as 75%. The thermal radiation loss was calculated assuming that heat is emitted from a dome-shaped surface of a sintered alumina rod of 2 mm radius. Results show that the thermal radiation loss was approx. 200 W, which is 10% of the input energy. The heat conduction loss was calculated from the sensible heat and heat of melting of the melted alumina under the assumption that all the melted parts achieved 3,250 K, the boiling point of alumina. The volume of the melted alumina was estimated from the length of melted alumina rod during laser ablation. Calculations show the heat conduction loss of legend B as about 300 W, which was 15% of the input energy. Error bars include the standard deviation of the ablation rate, molar reduction percentage, and the length of the melted alumina. Other energy would be lost by laser reflection from the alumina rod. Most of the input energy was consumed for alumina reduction by optimization of the laser intensity and laser spot occupancy. This result suggests that alumina rod preheating and laser spot size optimization minimized the energy consumption in the dissociation process. For further improvement, the energy distribution of the consumed energy for vaporization and dissociation should be changed. The aluminum collection process is left for investigation by future research efforts. The energy consumption, including the collection process, should be improved by maximization of the aluminum production rate by alumina preheating and laser spot size optimization as presented herein.

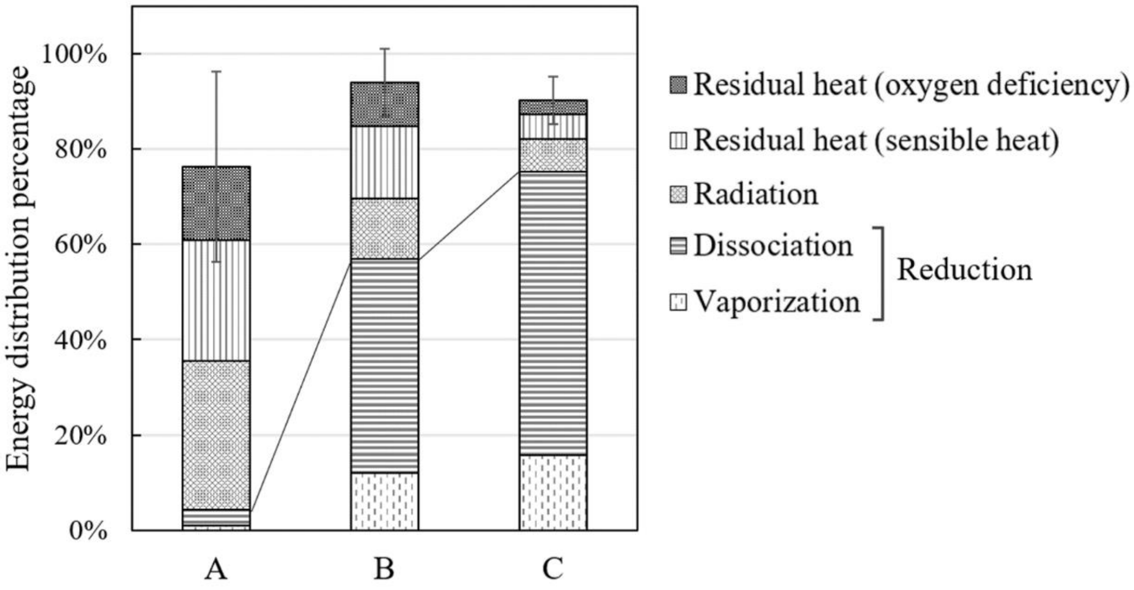

Figure 2-18 Energy distribution percentages in three conditions: A) the lowest laser spot occupancy in this experiment, B) optimized laser intensity, and C) optimized laser intensity and laser spot occupancy.

2.7 Summary

The experiment of alumina reduction by the laser ablation using a continuous-wave laser was conducted. The aluminum existence from the ablation plume, which was ejected from the alumina rod surface, was detected by emission spectroscopy. This result indicates the alumina dissociation was successfully conducted by the laser ablation using a CW laser.

Moreover, the aluminum production rate in the alumina dissociation process was evaluated by the measurements of ablation rate and molar reduction percentage, which was estimated from plume temperature and pressure. The ablation rate per unit area increased monotonically with laser intensity and laser spot occupancy. Experimentally, the maximum ablation rate of 45.2 mg/s was measured at a laser intensity of $F = 0.32$ GW/m^2 and a laser spot occupancy of $\alpha = 0.91$ with a laser power of 2.0 kW. The plume temperature was increased with the ambient pressure according to the pressure dependence of boiling point. By the alumina rod preheating, the plume temperature was increased up to $T = 4{,}100$ K, which was around the estimated superheat limit temperature. As a result of that, the maximum molar reduction percentage of $\eta_{\mathrm{re}} = 32\%$ was obtained at laser intensities over $F = 0.080$ GW/m^2, which was the threshold laser intensity to cause laser ablation. Therefore, the optimized condition for alumina dissociation in the laser ablation method at a laser power of 2.0 kW was determined to $F = 0.32$ GW/m^2, $\alpha = 0.91$. At the optimized condition, 75% of the input laser energy was consumed to alumina dissociation. The maximum aluminum production rate was 7.6 mg/s at a laser power of 2.0 kW, and the minimum energy consumption for aluminum production was obtained to $E_{\mathrm{Al}}\eta_{\mathrm{co}} = 73$ kWh/kg-Al.

Chapter 3

Aluminum particle nucleation on an alumina rod surface

3.1 Background for aluminum particle nucleation

3.1.1 Detection of aluminum particles on the alumina rod surface

To verify the existence of aluminum on the alumina rod surface after laser ablation, element identification was conducted using sodium hydrogen solution. The alumina rod was inserted in a flask containing NaOH solution. The following reactions of aluminum were presumed to take place.

$$2\mathrm{Al} + 2\mathrm{NaOH} + 6\mathrm{H_2O} \rightarrow 2\mathrm{Na[Al(OH)_4]} + 3\mathrm{H_2} \uparrow \qquad (3\text{-}1).$$

Figure 3-1(a) presents a photograph of an ablated alumina rod in NaOH solution. Bubbles were ejected continuously from the alumina rod surface. This result suggests the existence of aluminum on the alumina rod surface. Moreover, using scanning electron microscopy (SEM), many particles were detected on the alumina rod surface after laser ablation, as portrayed in Figure 3-1(b). After chemical treatment, the interiors of the respective spheres were lost; only the sphere shells remained, as shown in Figure 3-1(c). Therefore, the spheres on the alumina rod surface were found to be composed of aluminum. The sphere shell was alumina as an oxide film of aluminum. The oxide film thickness measured from the SEM image was t_{ox}= 0.1–0.2 μm, which is two orders of magnitude greater than the thickness of the aluminum oxide film formed at 300 K: 1 nm [68]. This result implies that the aluminum oxide film could be formed under high-temperature conditions because the oxide film thickness increases with temperature [69]. Moreover, the observed aluminum particles were spherical on the solid alumina. This result indicates that the particles would be formed in a liquid state after the resolidification of alumina at temperatures in the range of 933–2,300 K, considering the melting points of aluminum and alumina.

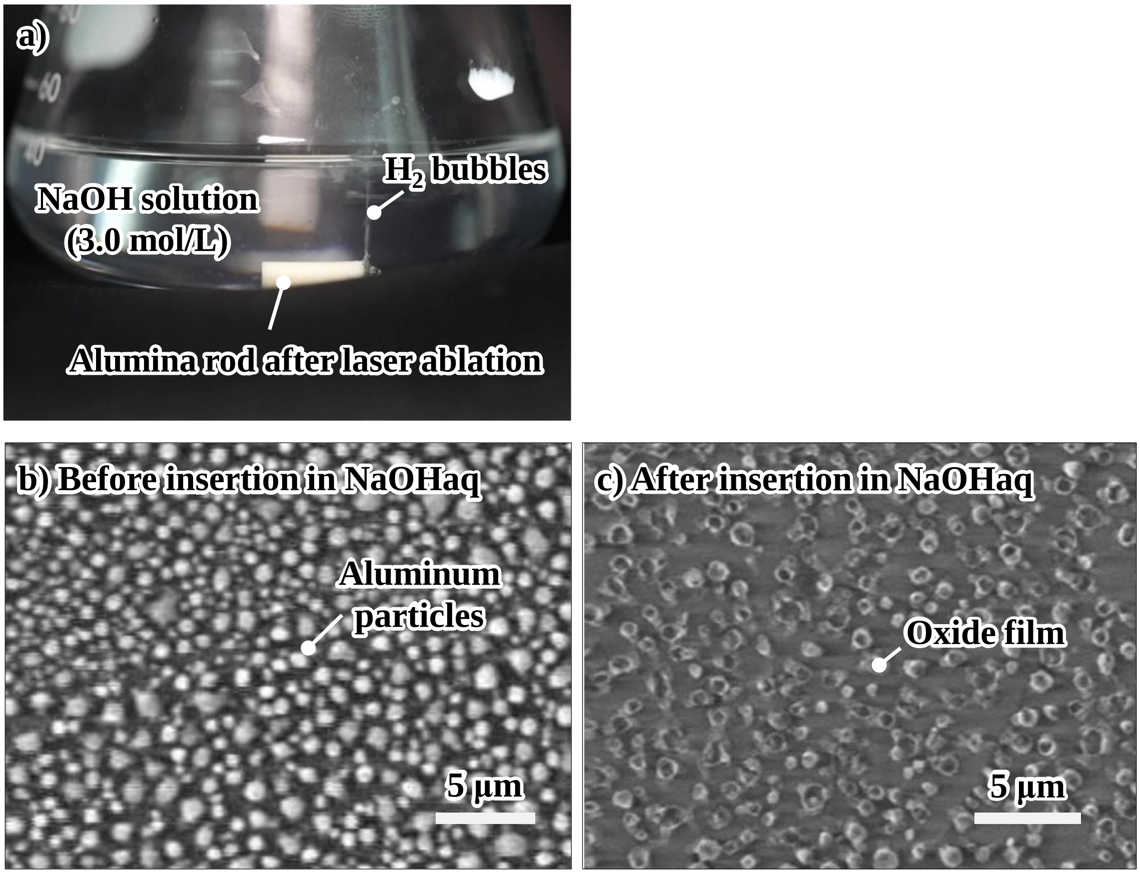

Figure 3-1 Picture of H_2 bubble ejection from the alumina rod (a) and SEM pictures of the rod surface (b and c).

3.1.2 Impurity precipitation of aluminum from oxygen-deficient alumina

As a mechanism of aluminum particle nucleation on the alumina rod surface, we propose impurity precipitation from the alumina rod. The precipitation of impurities from a mixture of metals has been examined for control of its material characteristics [70–71]. In the process of cooling the mixture, the crystal lattice of the mixture changes depending on its cooling rate. Under rapid cooling conditions, the precipitation of impurities can occur when the lattice formation rate of the base metal becomes much larger than the diffusion velocity of atoms. For a mixture of alumina as a base material and aluminum as an impurity, pure aluminum cannot exist stably in low oxygen deficiency alumina: the molar ratio of Al to O is greater than $Al_2O_{2.2–2.3}$[72]. Moreover, in the case of a high cooling rate of the alumina rod surface, aluminum can precipitate from an alumina rod with low oxygen deficiency. In the case of a low cooling rate, the aluminum can be absorbed by the oxygen-deficient alumina and pure alumina.

Therefore, important factors for impurity precipitation in aluminum particle nucleation are temperature change and oxygen deficiency of the alumina rod surface. Generally, lattice defect increases with temperature. Oxygen atoms preferentially exit because oxygen has a higher diffusion rate in the alumina lattice than aluminum does [73]. Therefore, the oxygen deficiency of alumina is expected to increase with temperature. A similar phenomenon can be found for titania: oxygen-deficient titania is produced by heating to 1,070 K in vacuum [74]. Moreover, the temperature of the ablation plume ejected from the alumina rod during laser irradiation increases with increasing laser power. The alumina rod surface temperature would increase monotonically with laser power, along with the plume temperature, because the surface temperature would be equal to the plume temperature. Therefore, the laser power for ablation is expected to be the critical parameter for aluminum particle nucleation.

3.1.3 Heterogeneous nucleation

Particles produced with heterogeneous nucleation are attached to the solid surface with a contact angle. The schematic of heterogeneous nucleation is presented in Figure 3-2. Its mechanism has been examined based on the energy change with the phase transition and surface shape variation [75–80]. Some particles, the white spheres in Figure 3-1, were present on the molten-resolidified surface with a contact angle. This result suggests the possibility that the particles were produced in the rod cooling process after laser ablation with heterogeneous nucleation. Its nucleation and nuclear growth are estimated from the Gibbs free energy using Eq. (3-2) [78–80]. Small ΔG signifies that nucleation can occur easily. Dependence of the particle radius on ΔG determines the nuclear growth.

$$\Delta G(r_\mathrm{p}) = \left\{-\frac{4}{3}\pi r_\mathrm{p}^3 \rho_\mathrm{Al} RT \ln\left(\frac{P_\mathrm{Al}}{P_\mathrm{s}(T_\mathrm{rod})}\right) + \left(4\pi r_\mathrm{p}^2 \sigma - E_\mathrm{S}\right)\right\} f(\theta),$$
$$f(\theta) = \frac{2 - 3\cos\theta + \cos^3\theta}{4} \qquad (3\text{-}2).$$

To obtain the small Gibbs free energy in heterogeneous nucleation to encourage aluminum nucleation and nuclear growth, large surface energy of the base alumina and a slight contact angle are needed. The large surface energy position on the base material is the grain boundary and dislocation line. The boundary layer and dislocation line are expected to encourage aluminum particle nucleation. The surface temperature affects the Gibbs free energy directly, as shown in Eq. (3-2). Moreover, the contact angle of the aluminum particle on the alumina base decreases along with the alumina temperature [81]. Therefore, the rod surface temperature will have an optimal value for the minimum Gibbs free energy for heterogeneous nucleation.

The critical radius for nucleation, the minimum particle size for thermodynamically stable with maximum ΔG, can be calculated from Eq. (3-3) [80, 82].

$$r_\mathrm{p}^* = \frac{2\sigma}{\rho_\mathrm{Al} RT ln\left(\frac{P_\mathrm{Al}}{P_s(T_\mathrm{rod})}\right)} \qquad (3\text{-}3).$$

For the beginning of stable nuclear growth, particles must overcome the critical radius. By comparing the minimum particle size and the critical radius, application of heterogeneous nucleation to aluminum particle nucleation on the alumina rod surface can be verified.

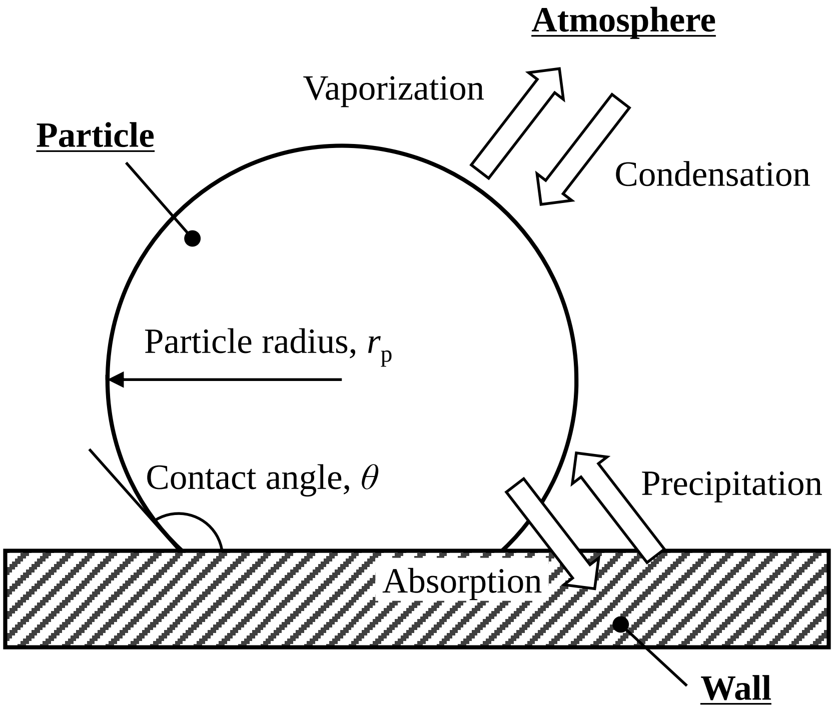

Figure 3-2 Schematic of heterogeneous nucleation.

3.1.4 Objective of this chapter

This aluminum particle nucleation was the first successful result of aluminum collection in the continuous laser ablation method. However, a large amount of aluminum in the ablation plume was wasted during the collection process with the previous collection system. Therefore, the aluminum collection should be performed by both aluminum particle nucleation on the alumina rod surface and aluminum adhesion on the plume cooling plate to decrease energy consumption for aluminum production. Consequently, in this chapter, the distributions of aluminum particles and surface temperature on the alumina rod after laser ablation were measured to verify whether the aluminum particle nucleation followed the heterogeneous nucleation theory, which the aluminum adhesion on the plume cooling plate obeys. If the particle nucleation were confirmed to be amenable to heterogeneous nucleation theory, then the alumina rod surface condition would be applicable to the condition of the plume cooling plate for achieving the aluminum collection from an ablation plume. Moreover, the elucidated mechanism of aluminum particle nucleation from the distributions of aluminum particle and surface temperature on the alumina rod might be used to increase the amount of aluminum particles produced on the alumina rod surface.

3.2 Aluminum particle measurement system

3.2.1 Particle nucleation by laser ablation of an alumina rod

The schematic of experimental setup is depicted in Figure 3-3. The laser ablation condition was the same as the experiment of alumina dissociation demonstration, described in Section 2.2.1, for obtaining aluminum particles on the alumina rod surface after laser ablation. The 4-mm diameter sintered alumina rod was inserted into the plate-shaped rod holder because the aluminum particles were detected on the hollowed-out alumina rod. For the laser ablation of alumina, a CW laser with power of 0.40–2.0 kW was irradiated to the sintered alumina rod for 1.0 s. The laser spot size on the alumina rod surface was 0.49 mm. Initially, the chamber was evacuated to 50 Pa using a rotary pump. Argon gas was supplied to the test chamber. The argon flow rate was 6.0 slm. Ambient pressure in the test chamber was maintained at 1.0 atm during the experiment. After laser ablation, the alumina rod was cooled by heat conduction through the rod holder.

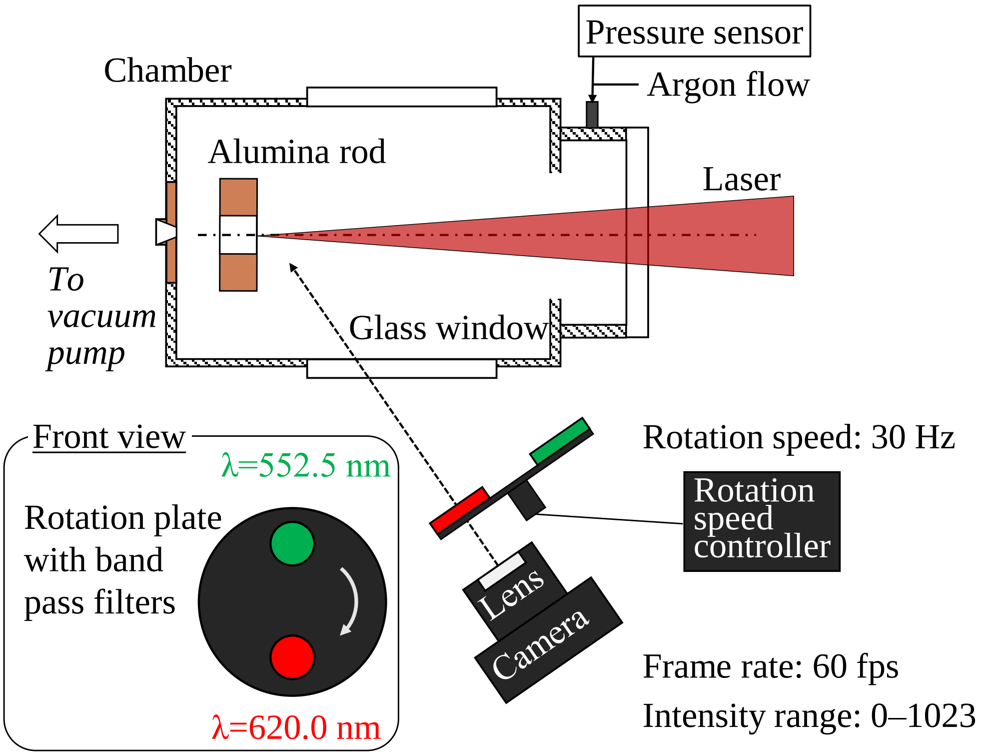

Figure 3-3 Alumina laser ablation system with surface temperature measurement setup of two-color method.

3.2.2 SEM observation and EDX analysis of the particles

The alumina rod surface after laser ablation was observed using SEM at an acceleration voltage of 15 kV and magnifications of ×7,000 and ×35,000 for detailed elemental analyses. In this study, JSM-IT100 SEM (JEOL Ltd.) of the Institute for Solid State Physics at the University of Tokyo was used. The resolution of SEM was 4 nm at an acceleration voltage of 15 kV. However, the resolution of SEM images was limited by the picture size converted by a control computer. Therefore, the resolution of SEM images depended on the magnification of SEM observation. The mole fractions (Al:O) of particles and the rod surface were measured by qualification analysis of EDX: elemental map and X-ray energy spectra. The measurements of X-ray energy spectrum were conducted respectively at three different positions on particles and rod surface. Moreover, the surface observation was conducted using SEM at an acceleration voltage of 1.0 kV for obtaining detailed surface images. The penetration depth to alumina at 1.0 kV was 0.04 μm.

The surface coverage, the percentage of the rod surface covered with particles, and the mean radius of particles were measured by analysis of SEM images using ImageJ, a software for contour detection of particles and measurements of particle radius and coverage [83]. After the rod surface was divided into 12 sections in the radial direction from the center, each was observed using SEM. The magnification was set at ×500 to include the entire section in one SEM micrograph. The resolution of SEM image was 0.13 μm/pixel. When the particle was not detected in the obtained SEM images at ×500, the magnification was increased to ×6,000 at the center of the SEM image; the resolution was 0.010 μm/pixel. The minimum measurable particle radius of the image analysis was 0.03 μm because several pixels were needed to be recognized as a particle by ImageJ. Image analysis was conducted only at the in-focus central area of SEM images when the out-of-focus position was included in the analyzed image as a result of the rod surface tilt produced by laser excavation. Assuming that all the aluminum particles have the same size to mean particle radius in each SEM image, the aluminum mass area density was estimated by application of the measured surface coverage, mean particle radius, and oxide film thickness to Eq. (3-4).

$$
\begin{aligned}
m_{\mathrm{Al}} &= \rho_{\mathrm{Al}} n_{\mathrm{p}} v_{\mathrm{p}} \\
&= \rho_{\mathrm{Al}} \sum_{j=1}^{12} \frac{\varsigma_j \pi \left(r^2(j) - r^2(j-1)\right)}{\pi r_p^2(j)} \frac{4\pi \left(r_p(j) - t_{\mathrm{ox}}\right)^3}{3}
\end{aligned}
\qquad (3\text{-}4).
$$

The oxide film thickness measured from the SEM image, shown in Figure 3 4, was measured to be 0.1–0.2 μm, which is two orders of magnitude greater than the thickness of the aluminum oxide film formed at 300 K: 1 nm [68]. This result implies that the aluminum oxide film was formed under high-temperature conditions because the oxide film thickness increases with temperature [69].

3.3 Rod surface measurement system

3.3.1 Rod shape observation

The rod surface shape was observed during and after laser irradiation using a video camera with the band pass filter: 620.0 nm wavelength for deleting the strong emission of AlO in the wavelength range of 500–600 nm. The FWHM and transmittance of band pass filter at the central wavelength of 552.5 μm were 10 μm and 41% respectively.

3.3.2 Surface temperature measurement using two-color method

The temperature distribution of alumina rod surface after the laser ablation was measured using a two-color method as shown in Figure 3-3. Under the assumption that radiation from the alumina rod surface with uniform spatial temperature depends on the wavelength following Wien's law, the surface temperature can be estimated from emission intensities at two wavelengths, as shown in Eq. (3-5)[86].

$$\frac{I(\lambda_1, T_S)}{I(\lambda_2, T_S)} = \frac{\varepsilon(\lambda_1) f(\lambda_1)}{\varepsilon(\lambda_2) f(\lambda_2)} \frac{\lambda_2^5}{\lambda_1^5} \exp\left(-\frac{C_2}{\lambda_1 T_s} + \frac{C_2}{\lambda_2 T_s}\right) \tag{3-5}$$

The video camera operating at a frame rate of 60 fps and the rotation plate operating at a rotation speed of 30 Hz with two band pass filters (552.5 and 620.0 μm wavelengths) were applied for the temperature measurement system. The FWHM and transmittance of band pass filter at the central wavelength of 552.5 μm was 4.5 μm and 78% respectively. The movie which was taken included photographs of the alumina rod surface at each wavelength alternately. By comparing the emission intensities with two wavelengths at each pixel, the surface temperature distribution was measured. The data was output in RGB 30-bit raw format for obtaining high-resolution emission intensities.

The measured emission intensity by the video camera was calibrated before the temperature calculation. The calibration factor was determined by comparing the intensities measured by the video camera and the emission intensities by spectroscopy as actual intensities. The emission intensities of a light source of halogen lamp with various input powers were measured by the video camera and the emission spectroscopy with the band pass filters at the same time. The measurement area of emission spectroscopy on the halogen lamp was a circle with a diameter of 2.0 mm. Figure 3-4 presents a photograph of the halogen lamp with the measurement area of emission spectroscopy. The measured intensities at the area by the video camera and the emission spectroscopy were compared.

As a result of this intensity measurement, the linear relationship between intensities measured by the video camera and spectroscopy was obtained at both wavelengths as presented in Figure 3-4. The calibration factors were estimated to be 8.54 and 2.37 at wavelengths of 552.5 nm and 620.0 nm, respectively. Considering the limitations of obtainable emission intensity by the video camera, temperatures were divided into three ranges for this experiment: 2,000–2,300 K, 1,600–2,000 K, and 1,300–1,600 K. The camera settings of the ISO number and F-number were varied with the measurable temperature range as shown in Table 3-1. This experiment was conducted three times for one laser power and one temperature range condition.

Table 3-1 Camera conditions of ISO number and F number with various temperature measurement range.

Temperature measurement range/ K	ISO number	F number
2,000–2,300	100	22.0
1,600–2,000	100	7.2
1,200–1,600	1,250	2.8

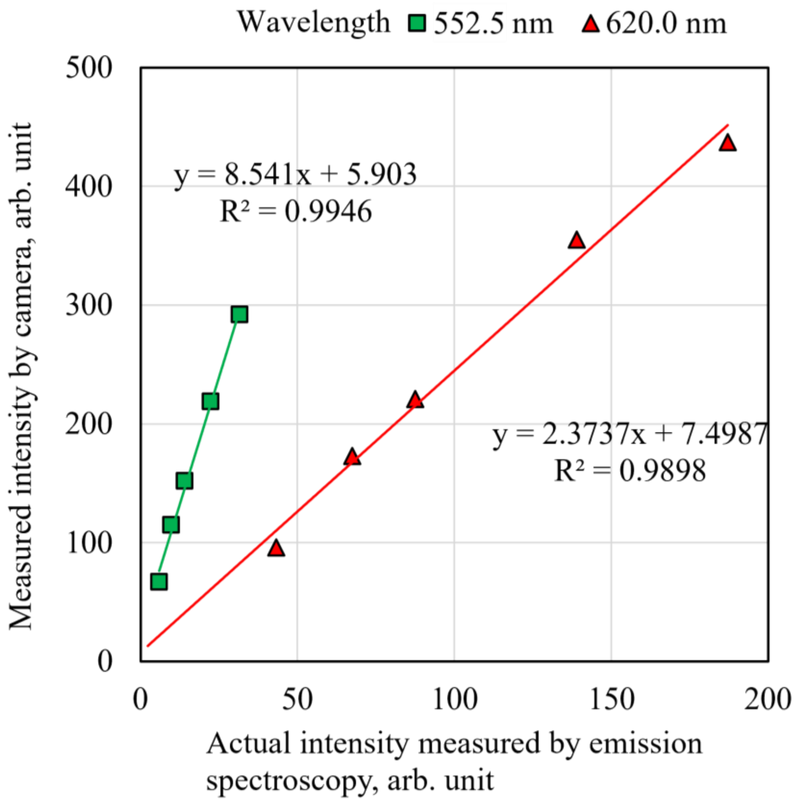

Figure 3-4 Relationship between intensities measured by the video camera and the emission spectroscopy at wavelengths of 552.5 nm and 620.0 nm.

3.4 Measured particle conditions on the alumina rod surface after laser ablation

The hollowed depth and the radius of oxygen-deficient area on alumina rod surface were increased with laser power. The SEM images at magnifications of ×7,000 and ×35,000 and EDX analysis results of ablated alumina rod surface are portrayed in Figure 3-5. The elemental maps indicate that most particles had a larger molar ratio of aluminum to oxygen than the rod surface did. The composition formula was measured as $Al_2O_{0.90}$ at the particles and $Al_2O_{2.5}$ at the rod surface from the X-ray energy spectra. Moreover, the result of EDX analysis with line scan is presented in Figure 3-6. The mass spectrum of aluminum was increased but oxygen was decreased. Therefore, the particles were confirmed to be aluminum and oxide film on the rod surface of oxygen-deficient alumina. The detailed surface images taken by SEM are presented in Figure 3-7. In addition to the aluminum particles, layers were observed on the alumina rod surface. The aluminum particles were incorporated into the layers. Moreover, some particles connected each other with a line.

Figure 3-8 presents an overall view of ablated alumina rod and SEM pictures of alumina rod surface in various radial positions at a laser power of 2.0 kW. The entire surface of the alumina rod became oxygen-deficient at a laser power of 2.0 kW. The distribution and radius of particles changed along with the radial position on the alumina rod surface. The patterns of aluminum particles at $r = 1.0$ mm are expected to result from the dislocation lines. The surface of quenched ceramics has many dislocation lines because of thermal stress [85–86]. The surface energy of dislocation lines encourages heterogeneous nucleation, as shown in Eq. (3-4).

Measurement results of the surface coverage, mean particle radius, and aluminum mass density are presented in Figure 3-9. The errors include the standard deviations and the errors attributable to uncertainty of the SEM image resolution. The rod center, $r =0$, was not observable because the rod was scooped out deeply by laser ablation. The surface coverage increased with distance from the rod center. With laser powers of 0.40 kW and 1.0 kW, no particle was found around the edge of the rod surface and not in the oxygen-deficient area: the percentage was zero. Large aluminum particles, which were obtained at laser powers of 1.0–2.0 kW, are expected to be produced by their nuclear growth. The laser power increased the surface coverage, mean particle radius, and aluminum mass area density. These changes could result from the increased oxygen-deficiency with laser power. The minimum mean particle radius was detected at a distance from the rod center of 0.70 mm with a laser power of 0.40 kW. Figure 3-10 presents a histogram of particle radius in the minimum particle detected condition. The minimum value of particle radius was r_p= 0.10 µm. Many particles at the condition had particle radiuses of 0.10–0.12 µm.

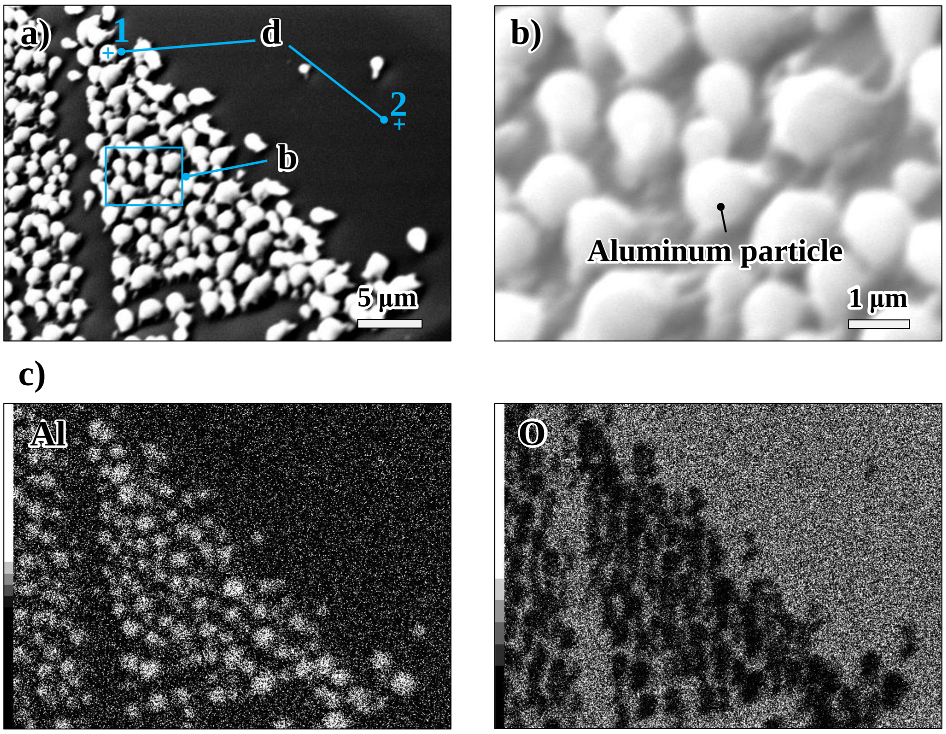

d) Point 1 (particle) **Point 2 (rod surface)**

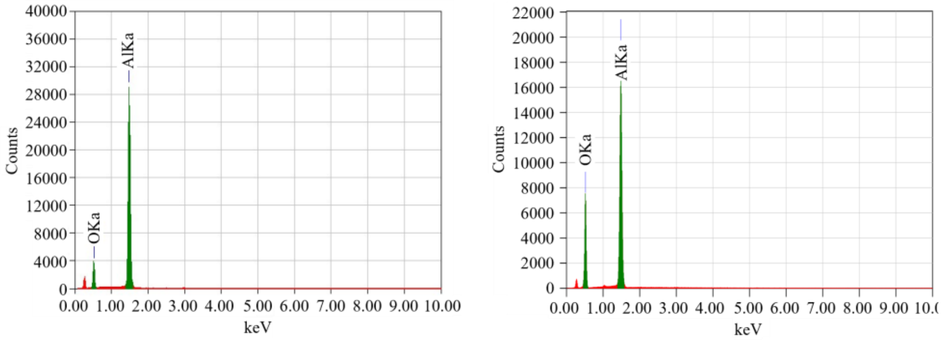

Figure 3-5 SEM pictures and EDX analysis results of the alumina rod surface at a laser power of 2.0 kW: a, b) views of alumina rod surface, c) elemental maps of aluminum (left) and oxygen (right), and d) X-ray energy spectra.

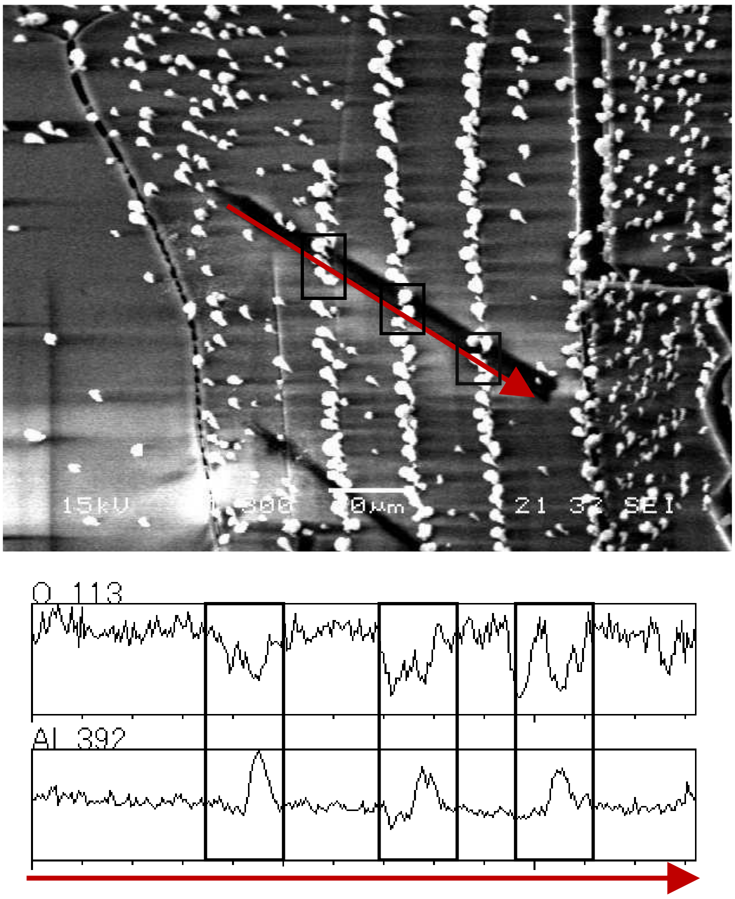

Figure 3-6 EDX analysis result of the alumina rod surface: SEM picture analyzed by EDX, and mass spectrum of oxygen and aluminum atoms through the red line in SEM picture.

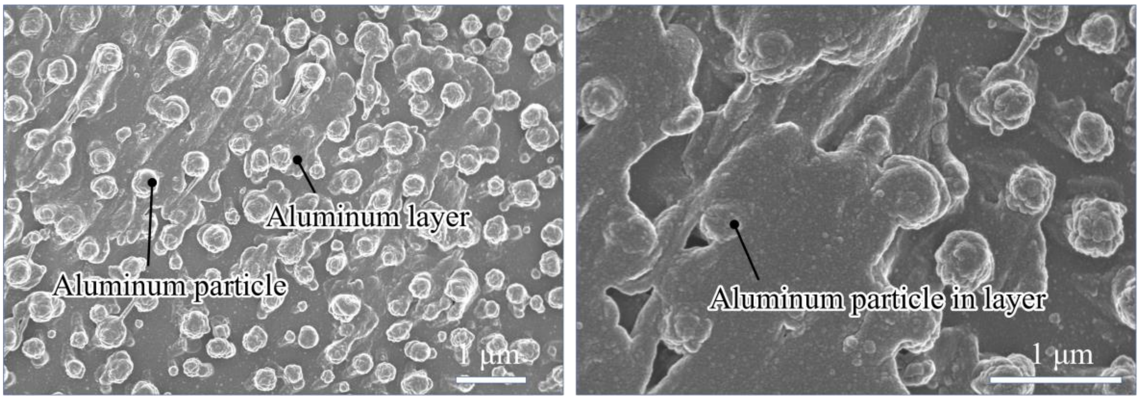

Figure 3-7 SEM picture of the alumina rod surface at an acceleration voltage of 1.0 kV: at magnifications of ×13,000 (left) and ×30,000 (right).

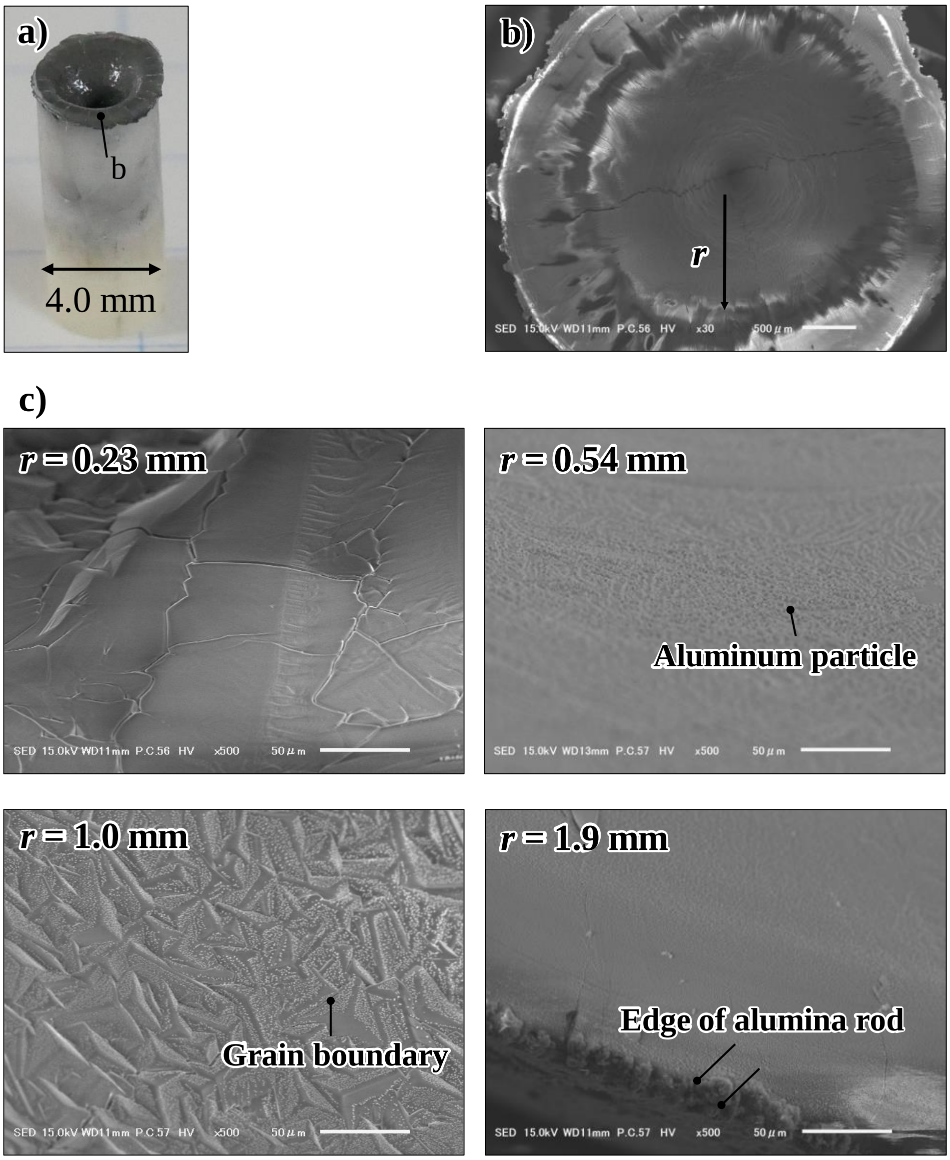

Figure 3-8 Photograph and SEM pictures of a hollowed-out alumina rod surface at a laser power of 2.0 kW, as obtained: a) overall view of alumina rod after laser ablation, b) overall view of alumina rod surface, and c) views of surface in various radial positions.

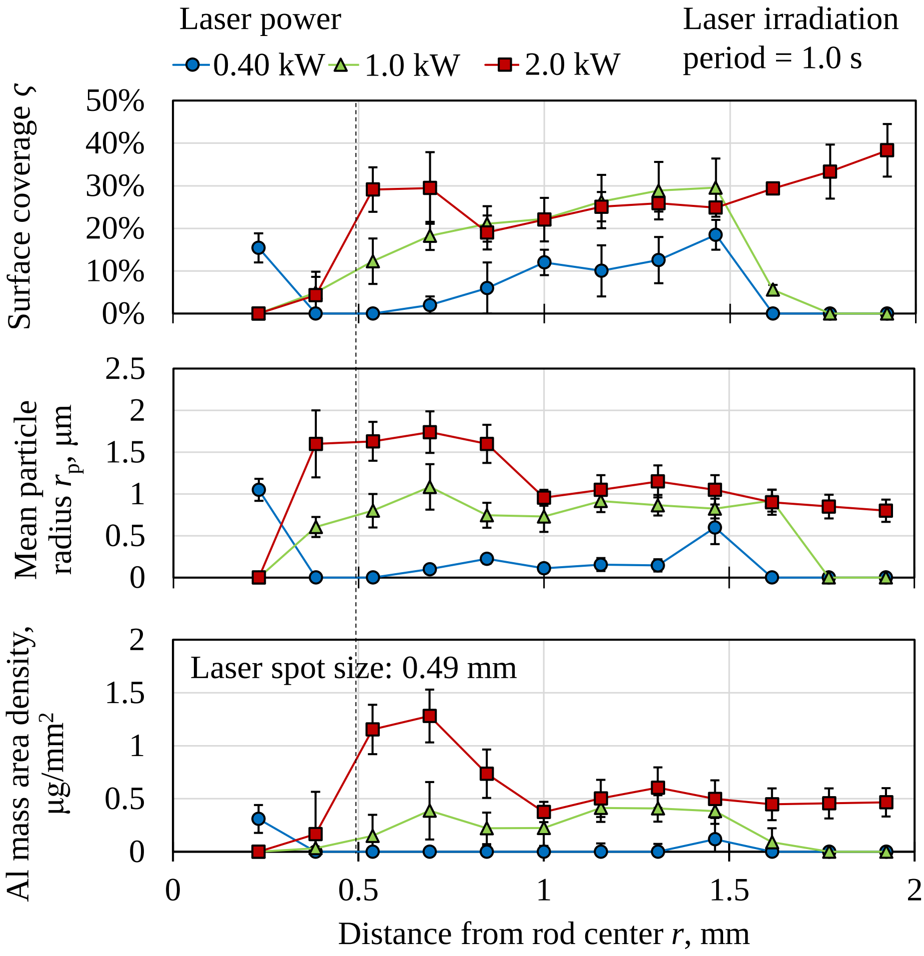

Figure 3-9 Measured surface coverage, mean particle radius, and Al mass area density vs. distance from rod center with various laser powers.

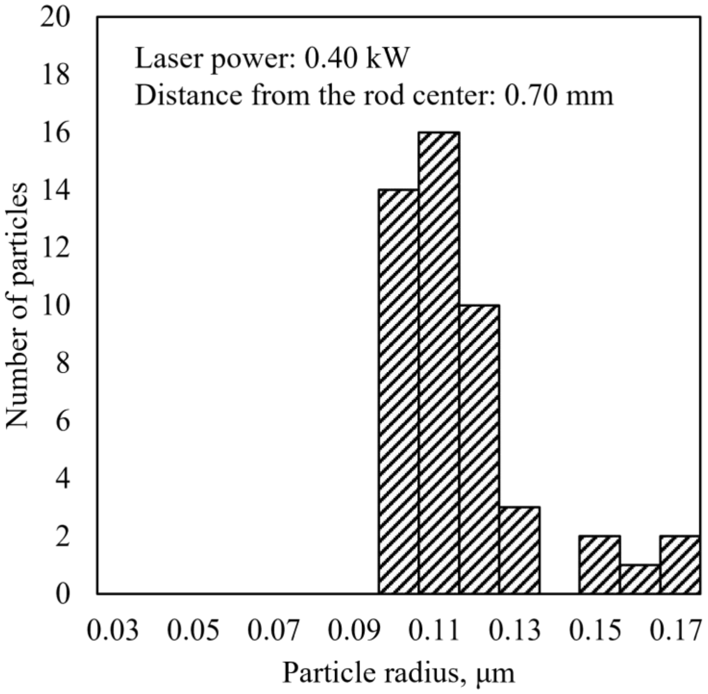

Figure 3-10 Histogram of particle radius and a distance from the rod center of 0.70 mm with a laser power of 0.40 kW, at which the minimum particles were detected.

3.5 Measured rod surface conditions during and after laser ablation

3.5.1 Shape change of the alumina rod

Photographs of the alumina rod surface during laser ablation are portrayed in Figure 3-11. The white dotted line represents the alumina rod surface shape before laser ablation. In addition, *t* = 0 represents the start of laser ablation. At the beginning of laser ablation, the molten alumina at the rod center produced a greatly inflated hemisphere. The liquid state of the hemisphere enlarged and flattened with laser irradiation; it finally deflated after laser ablation. The shape change of alumina rod suggests the existence of liquid flow of melted alumina on the rod surface.

3.5.2 Temperature distribution on the alumina rod surface

Figure 3-12 presents measurement results obtained for the temperature distribution of the alumina rod surface after laser ablation with various laser powers. The errors of the surface temperature include the standard deviations and the errors attributable to uncertainty of the camera sensitivity. The alumina rod surface was cooled after laser ablation. At around *t* = 1.25 s, the surface temperature achieved the melting point of alumina: 2,300 K. The temperature decreased with distance from the rod center. This decrease would be caused by heat loss from the edge of alumina rod. The time history of rod surface temperature was unaffected by laser power, although the plume temperature increased with laser intensity. The liquid flow might have flattened the surface temperature distribution while the melted alumina covered the rod surface: from *t* = 1.0 s to *t* = 1.25 s. As presented in Figure 3-12, the surface cooling rate did not vary with laser power, but surface temperature below the melting point of alumina was an important factor.

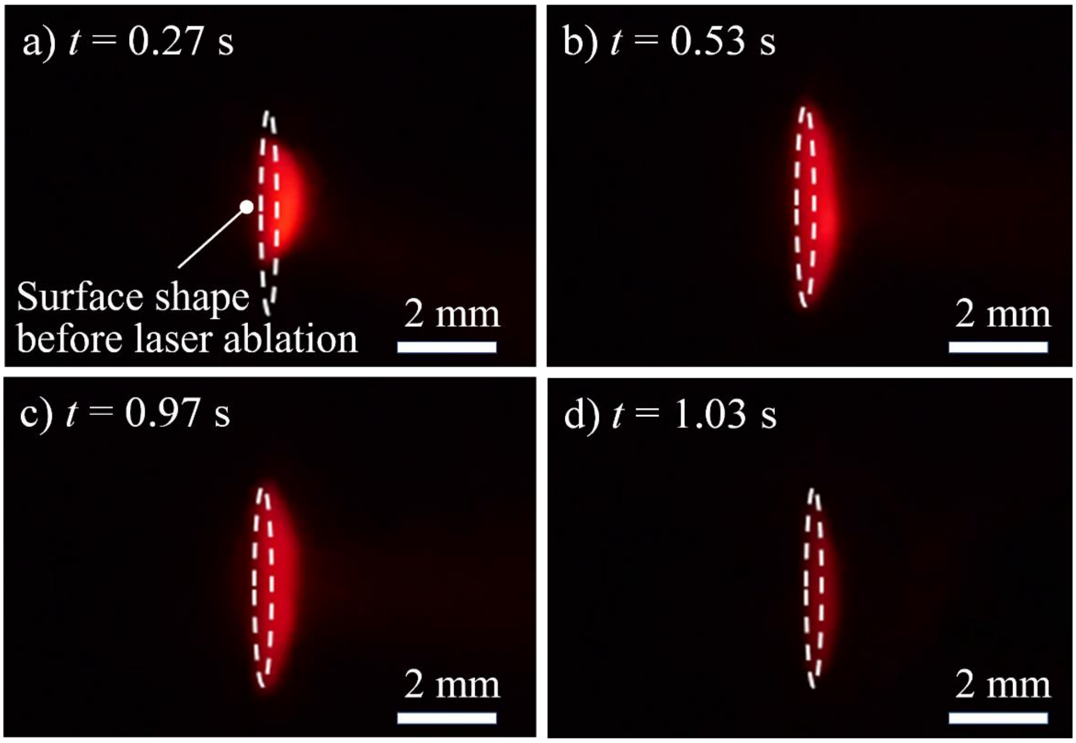

Figure 3-11 Photographs of the alumina rod surface during laser ablation at 620.0 nm wavelength. The white dotted line presents the alumina rod surface shape before laser ablation.

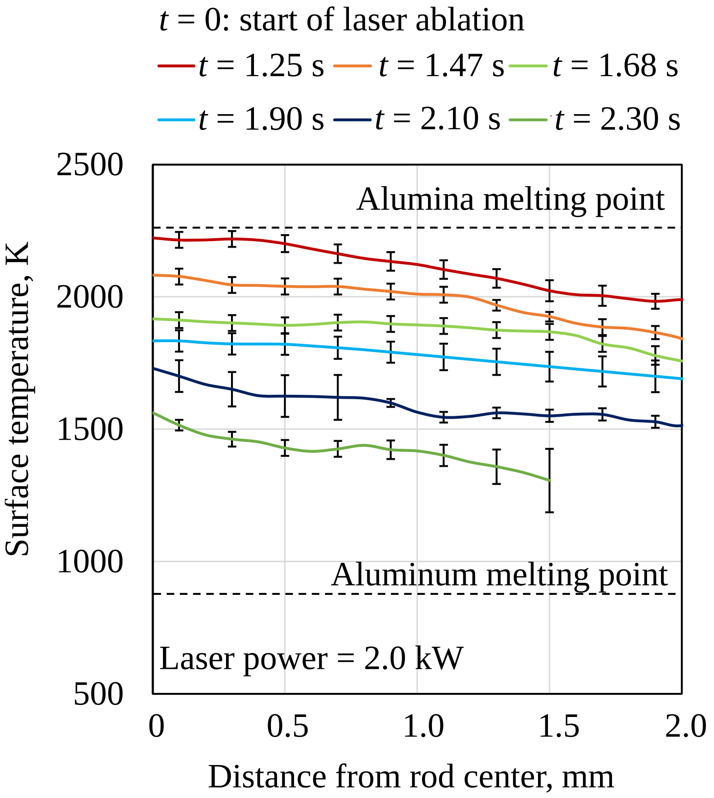

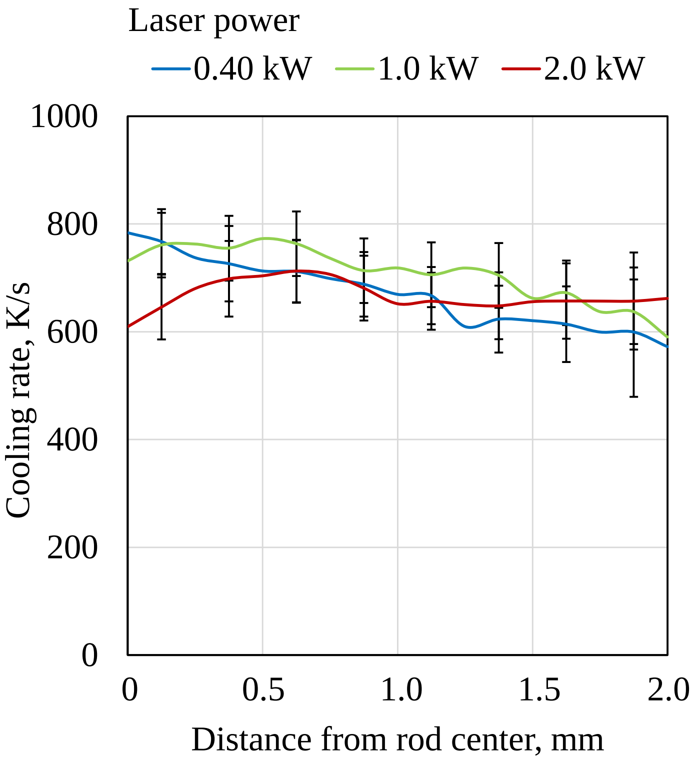

Figure 3-12 Time history of rod surface temperatures at a laser power of 2.0 kW (upper) and cooling rates with various laser power amounts (bottom).

3.6 Discussion

3.6.1 Validity of applying the heterogeneous nucleation theory

In this section, it is validated that the aluminum particle nucleation on the alumina rod surface obeyed the heterogeneous nucleation theory. The validity of applying the heterogeneous nucleation theory to the aluminum particle nucleation on the rod surface should be verified for discussing the conditions in aluminum collection from the ablation plume based on the obtained knowledges in the experiments of aluminum particle nucleation.

SURFACE OBSERVATION

The aluminum particles existed in the layer without an observable boundary as shown in Figure 3-7. This result indicates that the layer was composed of the same material with the particle: aluminum. Moreover, the result that the particles connected each other with a line suggests that the aluminum particles were nucleated from the layer. Two mechanisms of the particle nucleation with the line can be proposed: the particles were produced from the layer, or the particles made the layer. The particles could not be connected by the line after the nucleation of two particles. The line would be produced in the process that one large particle divided into two particles, which cannot be occurred in the layer production from the particles. Therefore, the existence of lines suggests that the particles were produced from the layer. Thereby, this SEM picture of Figure 3-7 should be under the aluminum particle nucleation from the aluminum liquid layer. This result directly indicates that the aluminum particle nucleation is heterogeneous nucleation.

PARTICLE RADIUS

The maximum critical radius was calculated by applying the minimum ratio of aluminum vapor and saturated vapor pressures, $P_{\mathrm{Al}}/P_{\mathrm{s}}(T_{\mathrm{rod}})$. The temperatures of gas and rod surface were assumed to be 2,300 K: the supposed maximum temperature at the impurity precipitation from the alumina rod surface. The aluminum partial pressure above the alumina rod surface was calculated to $P_{\mathrm{Al}} = 0.190$ atm from the chemical composition at ambient pressure of 1.0 atm and a laser power of 2.0 kW. The saturated vapor pressure of aluminum at $T_{\mathrm{rod}} = 2{,}300$ K is $P_{\mathrm{s}} = 0.188$ atm [87]. By substituting $P_{\mathrm{Al}}/P_{\mathrm{s}}(T_{\mathrm{rod}}) = 1.01$,

σ= 0.8 N/m [88–89], ρ_{Al}=2.1×10^3 kg/m^3[90], R= 300 J/kg K, and T= 2,300 K to Eq. (3-3), the critical radius for nucleation was estimated as r_{p}^*= 0.1 μm. The obtained smallest aluminum particle, as presented in Figure 3-10, had a radius of r_{p}= 0.10 μm, which is as large as the critical radius of r_{p}^*= 0.1 μm. This result suggests the validity of considering aluminum particle nucleation in heterogeneous nucleation theory.

3.6.2 Mechanism of aluminum particle nucleation

The inside of the hemisphere during laser ablation would be a gaseous state of alumina at high laser power of 1.0–2.0 kW because the laser-irradiated alumina was in a superheated state. During the deflation process with alumina rod cooling, the cover of the liquid hemisphere is expected to fill the room in the liquid alumina. Because of deflation, no aluminum particle area was produced around the center of the rod surface at high laser power, as shown in Figure 3-9. Moreover, the surface temperature at the center area would be higher than the edge area of alumina rod because of the laser energy input to the rod center and heat loss from the rod edge to the rod holder. Considering the radial temperature gradient at the alumina rod surface, the expansion of the molten alumina presented in Figure 3-13 is expected to result from the liquid movement of natural convection and Marangoni flow [91]. The oxygen-deficient alumina at the center of the rod surface might be spread by the liquid flow.

The surface cooling rate and oxygen-deficiency at a temperature below the melting point of alumina can be expected to affect the aluminum particle nucleation in terms of its impurity precipitation. From the experimentally obtained results, the aluminum particle nucleation was found to be affected by the laser power, as shown in Figure 3-9. Therefore, the increase of oxygen-deficiency along with the laser power would determine the change of aluminum particle nucleation on the alumina rod surface.

3.6.3 Aluminum collectable condition from an ablation plume

The necessary condition of rod surface temperature in the aluminum particle nucleation was T_{s} = 933–2,300 K as described in Section 3.1.1. Moreover, it was validated that the condition in aluminum particle nucleation is applicable to the aluminum

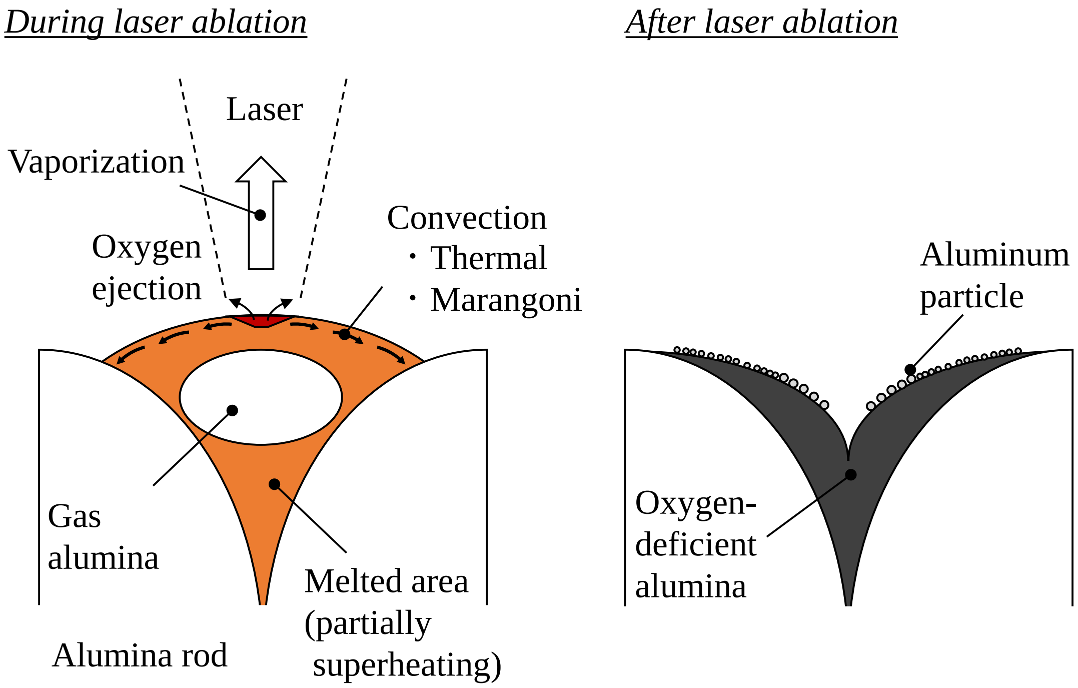

Figure 3-13 Schematic of liquid flow at the surface of alumina rod during and after laser ablation at high laser power.

collection from an ablation plume. Therefore, the surface temperature of collection system needs to be set in the range of 933–2,300 K.

Moreover, Figure 3-12 presents that aluminum is producible from oxygen-deficient alumina at such a time history of the surface temperature and at a cooling rate of 600–800 K. The amount of aluminum particles on alumina rod surface can be increased along with the cooling rate considering the mechanism of impurity precipitation. Moreover, in the earlier aluminum collection experiment using the plume cooling plate, oxygen-deficient alumina was adherent [92]. Aluminum adhesion in the laser ablation method would be accomplished by controlling the collection system surface temperature to keep the cooling rate of more than 600–800 K.

3.7 Summary

Aluminum particles were detected on the surface of laser-ablated alumina rod by SEM observation and EDX analysis. The aluminum mass area density increased with laser power. This tendency is expected to result from the great oxygen deficiency at high laser power. The minimum aluminum particle radius of $r_\mathrm{p} = 0.10$ μm was consistent with the critical radius for aluminum nucleation in heterogeneous nucleation theory: $r_\mathrm{p}^* = 0.1$ μm. Moreover, the aluminum layer was observed at the bottom of aluminum particles. The aluminum particles should be produced from the aluminum layer in the alumina rod cooling process. These results indicate that the aluminum particle nucleation obeys heterogeneous nucleation theory. The estimated necessary condition of surface temperature for the aluminum particle nucleation in the range of $T_\mathrm{s} = 933$–2,300 K would be applicable to the aluminum collection plate for achieving aluminum collection from an ablation plume.

The molten alumina hemisphere was enlarged and flattened with laser irradiation. It was finally deflated after laser ablation was completed. This result represents the liquid flow of molten alumina and expansion of oxygen-deficient alumina. The cooling rate of the rod surface, the important factor of impurity precipitation, was unaffected by laser power. Therefore, the increase of oxygen deficiency with laser power is expected to affect the change of aluminum particle nucleation on the alumina rod surface. Control of the surface temperature and high oxygen-deficiency are fundamentally important for aluminum collection when using the laser ablation method.

Chapter 4 and Chapter 5 are omitted in this thesis because the contents will be published in a journal paper in five years.

Chapter 4, Chapter 5 は投稿論文として掲載される予定であり、本博士論文（要約）では非公開としている。（５年以内に出版予定）

Chapter 6

Conclusion

In this dissertation, alumina reduction by laser ablation using a continuous-wave laser was investigated towards the utilization of lunar resources based on the concept of in-situ resource utilization.

Firstly, alumina dissociation by laser ablation using a CW laser was experimentally demonstrated. The plume temperature and molar reduction percentage were increased by alumina rod preheating with upper limits. The limitation of plume temperature was approximately equal to the superheat limit temperature of alumina. The ablation rate per unit area was increased with laser spot size and laser intensity. Aluminum production rate can be maximized by alumina rod preheating and optimization of laser spot occupancy and laser intensity.

Secondly, aluminum particles were detected on the alumina rod surface after laser ablation. The impurity precipitation of aluminum from high oxygen-deficient alumina was proposed as the mechanism of aluminum particle nucleation. The aluminum particle nucleation on the alumina rod surface by laser ablation obeyed heterogeneous nucleation theory. The aluminum particle nucleation was suggested to be conducted at temperatures in the range above the melting point of aluminum and below the melting point of alumina. The cooling rate of alumina rod surface after laser ablation was measured to 600–800 K/s, which was estimated to be a sufficient condition for impurity precipitation of aluminum from high oxygen-deficient alumina.

Thirdly, aluminum collection from the ablation plume was successfully conducted by the tantalum plate at a plate temperature of 1,500 K. The aluminum collection percentage was 2.0%, which was approximately 70 times as large as the percentage by the previous aluminum collection system: an alumina tube. The plate temperature and material atomic diffusion and the chemical reaction of aluminum with the collection plate affected the aluminum nucleation on the collection plate.

Finally, the comprehensive system evaluation of the alumina reduction method was conducted by applying the optimized conditions in alumina dissociation and aluminum collection. The aluminum collection rate and energy consumption for aluminum production were measured to 0.11 mg/s and 5.0 MWh/kg-Al, respectively. The high aluminum collection rate is a strong point of laser ablation method using a CW laser.

Acknowledgements

For the completion of my doctor thesis, I have been supported a lot by many people. I would like to express the acknowledgments in my mother language, Japanese.

本研究は完成に至るまでに，多くの方々のご指導とご協力を賜りました．ここに皆様への感謝の意を示します．

はじめに，本研究テーマを与えてくださった小紫公也教授に深く感謝いたします．これまで学部時代含め 6 年間に渡り，研究のいろはから指導していただきました．研究を進める過程でこちらが材料的な専門知識に傾倒していく中で，小紫先生にはエネルギー保存則のような物理の基盤となる観点から支えていただき，頭が偏ってしまった状態からハッと目が覚めるような鋭い意見を何度もしていただきました．正直なところ修士課程までは研究での議論においていただいたコメントを理解しきれず，なぜこのような方針をとるのだろうかと悩んだこともありました．しかし博士課程に進学し研究をより俯瞰的に見られるようになったことで，小紫先生が研究内容の本質を突きながら，さらにこちらが成長できるよう課題も与えるという教育的側面を持ってコメントしていただいていたと気づき，その慧眼と懐の深さに感服いたしました．小紫先生の下で博士課程を過ごせたことは間違いなく今後の研究生活における大きな財産となりました．以前小紫先生がおっしゃっていたように，研究室で培ったものを科学界含め社会に還元できるよう今後も精進いたします．

小泉宏之准教授には，研究室輪講での論理的議論に加え，研究生活において”武器”となる考え方を何度もご教授いただきました．特に特別輪講で話されていた (研究力)×(表現力) という話は，研究における表現力の重要さを認識させただけでなく，抽象的事象の細分による具体化という一種の思考メソッドを学ぶきっかけにもなりました．この方法は，研究における還元過程の細分化からタスク処理における具体化に至るまで幅広く活躍し，研究生活をクリアにする強力な武器となったように思います．研究室でのミーティングの行い方など含め，常に上を目指し新しいメソッドを開拓していく小泉先生には大きな刺激を受け，尊敬するばかりでした．また，精力的に研究指導を行い，研究室運営から執筆まで行う，これが研究者なのだと感銘を受けたこともよく覚えております．研究者としての在り方を示していただいたこと，研究での武器を与えていただいたこと，改めて感謝いたします．

川嶋嶺特任助教には, PR セミナーや輪講で何度もご意見をいただきました. 簡単な質問から段々深い質問に変わっていくスタイルは, 聴衆も川嶋さんの思考流れを追っていけるため非常にわかりやすく, 質問方法の参考にしておりました. また自身の研究と並行して研究室の環境を整えていただいたこと, 非常に感謝しております.

関根北斗助教授は柏で最も長く付き合いのある先輩であり, 公私ともに大変お世話になりました. 飲み会に度々連れて行ってもらうなど非常にラフに接していただき, 関根さんのボケにツッコむことを楽しみに研究室に行っていた所もありました. 身近な関根さんだったからこそ, 尊敬も人一倍強く感じていました. 専門知識をもって理路整然とした議論を行い, そして PPPL での研究留学など経験をすべて吸収してどんどんレベルアップしていかれる姿に, 強く憧れ尊敬しておりました. 後輩との接し方から研究姿勢まで参考になる部分ばかりで, 今の自分を形成するうえで最も影響を受けたように思います.

研究室秘書の田原さんにも感謝いたします. 頻繁にお菓子をいただいたり, 逆に田原さんが苦い顔をしているときにこちらから声をかけたり, 研究室の”お隣さん”として仲良くしていただきました. 研究生活からほっと一息つくあの時間があったからこそ, ここまで研究生活を続けられたように思います. ありがとうございました.

研究班の後輩の山田君, 佐藤君, 田中直輝君, 高野君には, 拙い私の指導についてきてもらいながら, 協力して研究を進められたおかげで順調に実験を行うことができました. 研究当初はほとんど実験的知見もなく手探りで始めた状態でしたが, 研究班として着々と積み重ねてきた結果ここまでに至ったと思います.

博士唯一の同期である田畑君にも感謝します. 自分にはない, 論文作成力, 几帳面さ,そしてジャイロトロン完成に至った完遂力でもって研究をガンガン進めていく姿は同期ながら圧倒され, 負けていられないと刺激を受けていました. 同期の田畑君と切磋琢磨できたことは非常に幸運だったと思います. ありがとうございました.

すでに博士課程を卒業されました中村さん, 松井さん, 柳沼さん, 浅川さん, 中川さんにも大変お世話になりました. 優秀かつ全員バラエティに富んで突出したみなさんに憧れ, 博士課程進学を決めたところがありました. 修士 2 年の時に輪講で各々が異なる視点で議論を交わしているのを見て, 研究は一人で行うものではなく多種多様な研究者が協力して創り上げていくのだと実感したこともよく覚えております. みなさんの背中を追いかけて入った博士課程を通して, 追いついたとは言えませんが自分なりに尖っていけたのではないかと思います. 改めてありがとうございました.

最後に, これまで支えていただいた両親にこの場で感謝申し上げます. 東大入学から博士課程進学に至るまで常に予想外の方向へ進むにも関わらず, 変わらず応援し頼りにできる環境を作っていただけたことは, 博士課程での心の支えとなりました. 博士論文完成にあたり, 改めて感謝申し上げます。

2022 年 1 月 7 日
田中聖也

Appendix A-1

Aluminum collection by a collection plate [92, 93]

A.1.1 Aluminum collection system using a collection plate

Alumina dissociation by the laser ablation using a CW laser was demonstrated and optimized for the aluminum production rate, explained in Chapter 2. Next, aluminum collection experiment was conducted using a copper collection plate.

The experimental setup is presented in Figure A-1-1. The laser ablation was conducted with alumina rod preheating and laser spot optimization from the conclusion in Chapter 2. The experimental conditions are shown in Table A-1-1. The alumina rod was preheated to 1,500 K by the semiconductor laser. The copper collection plate, which had a hole for the laser path, was placed above the alumina rod perpendicular to the ejected ablation plume as presented in Figure A-1-2. The collection plate and the alumina rod holder were set on the chamber at an angle of 45° to the chamber bottom so that the ablation plume would collide with the collection plate. The distance between collection plate and alumina rod surface was 5–10 mm. The collection plate was not preheated before the laser ablation. the ablation rate and adhesion rate were measured from the mass change of alumina rod and collection plate, respectively. The existence of aluminum on the collection plate after the laser ablation was verified using NaOH solution.

Table A-1-1 Experimental conditions using a collection plate.

Laser ablation condition	
Laser power/ kW	2.0
Laser spot size on rod/ mm	2.0
Alumina rod radius/ mm	2.0
Laser intensity/ (GW/m^2)	0.16
Laser spot occupancy	1.0
Laser irradiation period/ s	1.0
Argon ambient pressure/ atm	1.0
Preheating temperature/ K	1,500
Collection plate condition	
Material	Copper
Plate temperature /K	300
Distance between rod and plate /mm	5

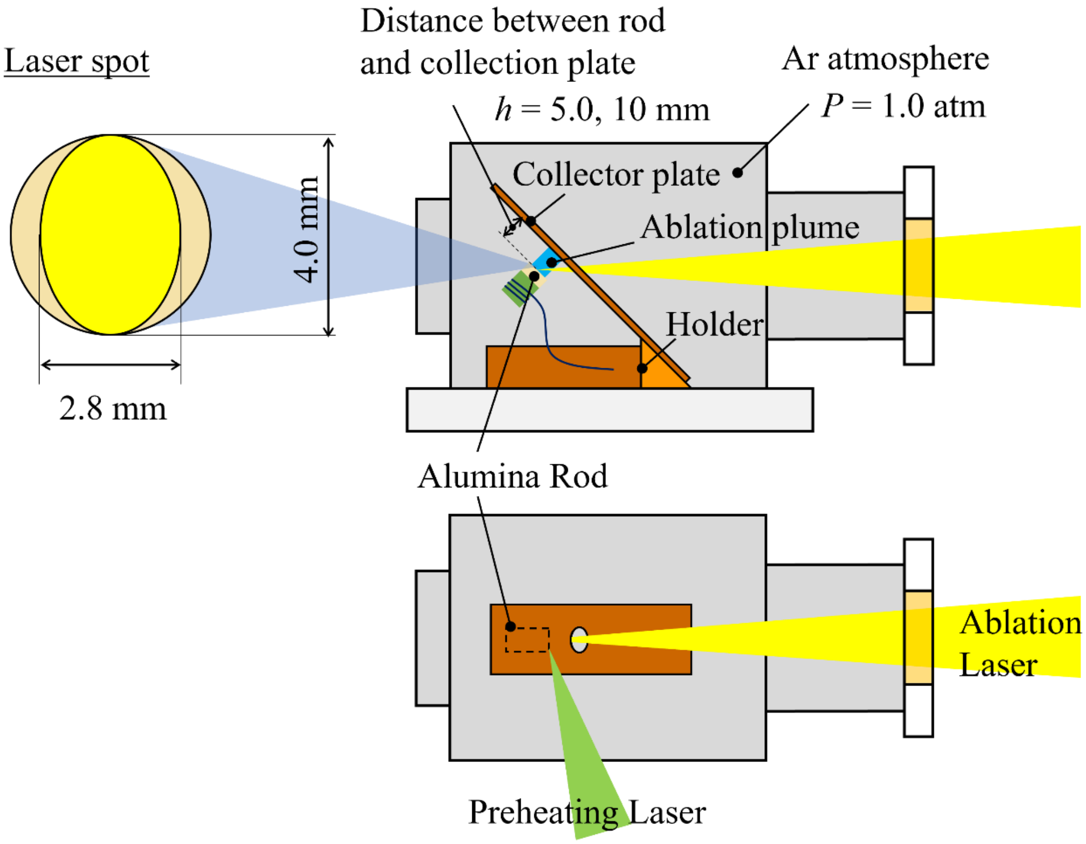

Figure A-1-1 Schematic of aluminum collection system using a collection plate.

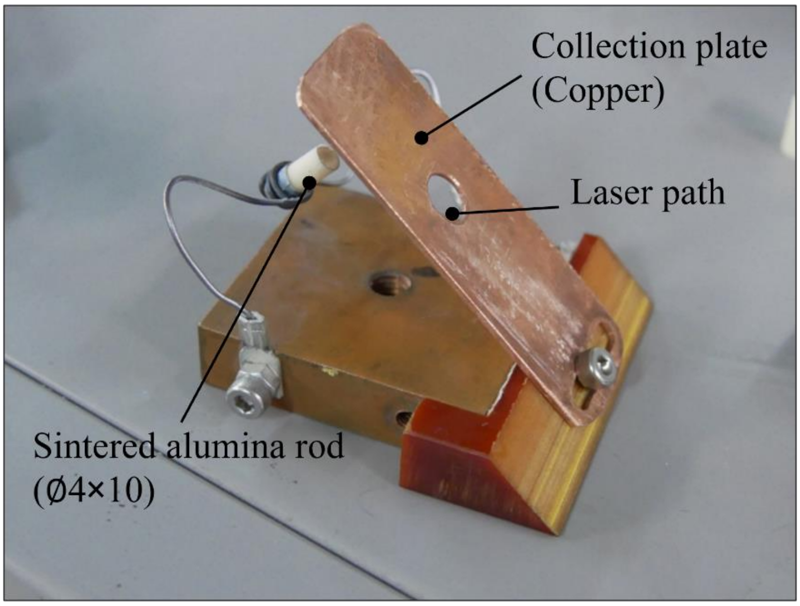

Figure A-1-2 Photograph of the collection plate fixed to the alumina rod holder.

A.1.2 Analysis of adhesion to the collection plate

ADHESION PERCENTAGE

Figure A-1-3 is the photograph taken during the laser ablation. the ablation plume collided with the collection plate as expected. The measured adhesion percentage is depicted in Figure A-1-4. Results show that the adhesion percentage was increased by shortening the distance between the alumina rod and the collection plate. Moreover, the adhesion percentage was 78% at the distance of 5 mm. This result indicates that the most of ablated substances adhered to the collection plate.

ADHERED SUBSTANCES TO COLLECTION PLATE

The photographs of collection plates after the laser ablation are presented in Figure A-1-5. Recombined alumina and oxygen-deficient alumina were observed on the collection plate. As a result of the insertion of collection plate into NaOH solution, bubble ejection of hydrogen gas was not detected. This result indicates aluminum did not exist on the collection plate. Therefore, the aluminum collection was not achieved by the collection plate. This should be caused by the recombination of aluminum and oxygen.

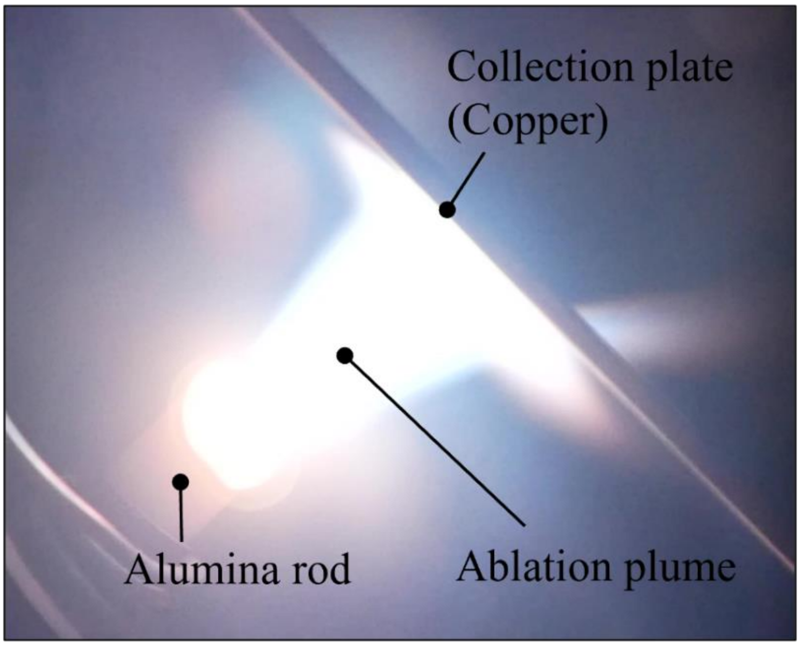

Figure A-1-3 Photograph of the ablation plume hitting to the collection plate.

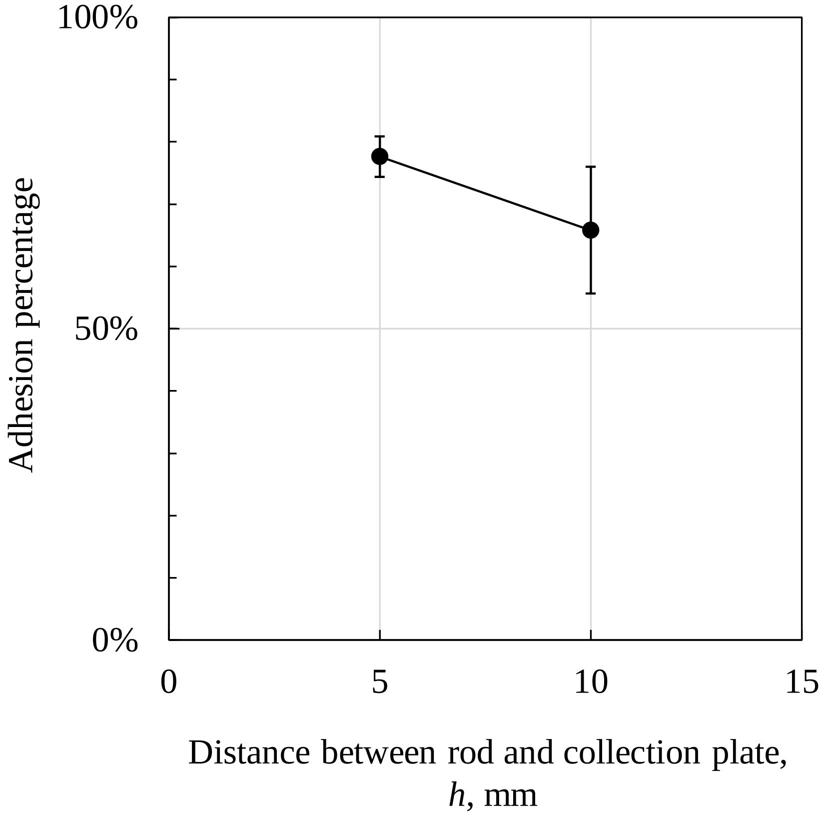

Figure A-1-4 Measured adhesion percentage with various distances between the alumina rod and the collection plate.

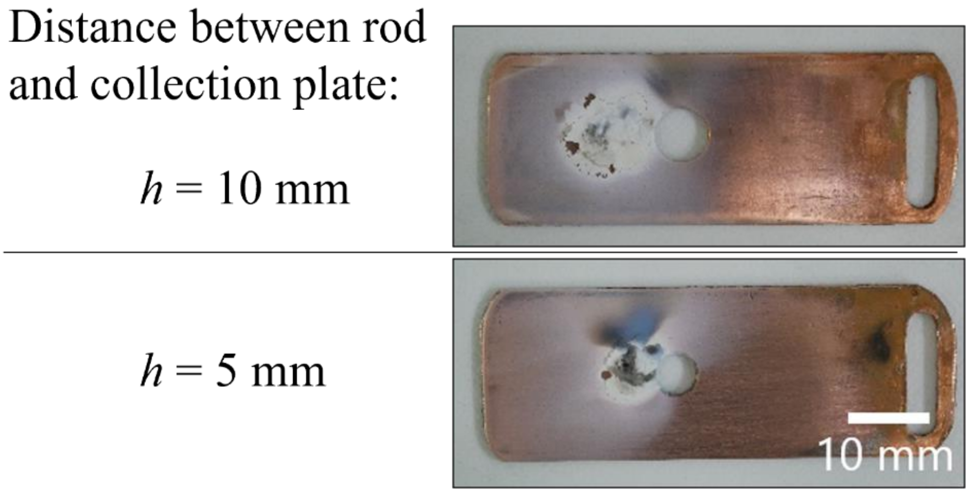

Figure A-1-5 Photograph of the collection plates after laser ablation.

The surface temperature of collection plate was estimated to be under the melting point of aluminum during the laser ablation. The aluminum adhered to the collection plate would coagulate at the low temperature. the particle radius of coagulated material is generally several nanometers. In the case of aluminum, nano particles are fully oxidized because the thickness of an oxide film is nanometer order. Therefore, the aluminum particles were not detected on the collection plate by the recombination of aluminum and oxygen.

Appendix A-2

Aluminum collection by a collection tube [93]

A.2.1 Calculation of aluminum partial pressure in a collection tube

DESIGN OF COLLECTION TUBE

For the aluminum collection based on the condensation, a collection tube was applied. The design of the collection tube is presented in Figure A-2-1. The inner diameter of the collection tube was larger than the diameter of the alumina rod to prevent the melted alumina rod surface from adhering to the collection tube. For causing the condensation of aluminum to the collection tube, the temperature of collection tube was set to 1500 K, which was larger than the melting point of aluminum: 930 K.

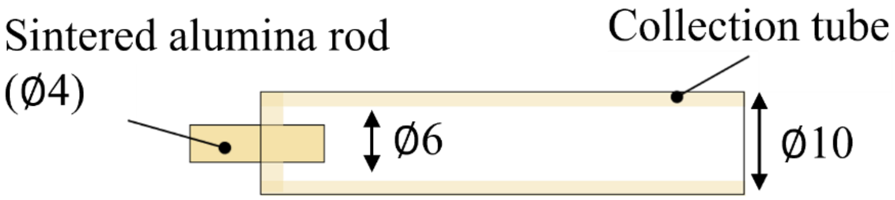

Figure A-2-1 Schematic of aluminum collection system using a collection tube.

SIMULAITION SCHEME

The two-dimensional numerical simulation was carried out in radial and axial dimensions. The velocity and pressure fields were calculated from the continuity equation of incompressible viscosity, Eq. (A-1-1), and the Navier-Stokes equation, Eq. (A-1-2).

$$\frac{\partial u}{\partial x}+\frac{\partial v}{\partial y}=0 \tag{A-1-1}$$

$$\begin{aligned}\frac{\partial u}{\partial t}+u\frac{\partial u}{\partial x}+v\frac{\partial u}{\partial y}&=-\frac{\partial p}{\partial x}+\frac{1}{\mathrm{Re}}\left(\frac{\partial^2 u}{\partial x^2}+\frac{\partial^2 u}{\partial y^2}\right)\\ \frac{\partial v}{\partial t}+u\frac{\partial v}{\partial x}+v\frac{\partial v}{\partial y}&=-\frac{\partial p}{\partial y}+\frac{1}{\mathrm{Re}}\left(\frac{\partial^2 v}{\partial x^2}+\frac{\partial^2 v}{\partial y^2}\right)\end{aligned} \tag{A-1-2}$$

The calculation was proceeded by the combination of Poisson's equations, Eq. (A-1-3), and Navier-Stokes equations, which are derived by combining continuous equations and Navier-Stokes equations.

$$\frac{\partial^2 p}{\partial x^2}+\frac{\partial^2 p}{\partial y^2}=-\left\{\left(\frac{\partial u}{\partial x}\right)^2+\left(\frac{\partial v}{\partial y}\right)^2+2\frac{\partial u}{\partial y}\frac{\partial v}{\partial x}\right\}+\frac{1}{\Delta t}\left(\frac{\partial u}{\partial x}+\frac{\partial v}{\partial y}\right) \tag{A-1-3}$$

Regarding the boundary conditions, the rod surface was set as the blowout condition, and the other boundaries were set as the wall surface condition with a velocity of 0.

Next, the temperature field was calculated from the energy equation, Eq. (A-1-4), using the calculation result of velocity field.

$$\begin{aligned}&\rho c\left(\frac{\partial T}{\partial t}+u\frac{\partial T}{\partial x}+v\frac{\partial T}{\partial y}\right)=k\Delta T+\mu_v\Phi\\ &\Phi=2\left\{\left(\frac{\partial u}{\partial x}\right)^2+\left(\frac{\partial v}{\partial y}\right)^2\right\}+\left(\frac{\partial u}{\partial y}+\frac{\partial v}{\partial x}\right)^2-\frac{2}{3}\left(\frac{\partial u}{\partial x}+\frac{\partial v}{\partial y}\right)^2\end{aligned} \tag{A-1-4}$$

The boundary condition was set to temperature of 1500 K on the collection tube surface.

Finally, the concentration field of the Al-O gas was calculated from the convection-diffusion equation, Eq. (A-1-5), using the result of the velocity field.

$$\frac{\partial C}{\partial t} + \nabla \cdot (\boldsymbol{v}C) = \nabla \cdot (D\nabla C) \tag{A-1-5}$$

The value of the diffusion coefficient of carbon dioxide to argon at 300 K, 1.5×10^{-5} m^2/s, was applied to the diffusion coefficient *D* of the Al-O gas. The diffusion coefficient is proportional to the 1.8th power of the temperature, Eq. (A-1-6).

$$D(T) = \left(\frac{T}{T_0}\right)^{1.8} D(T_0) \tag{A-1-6}$$

The aluminum partial pressure was obtained by application of the mole fraction of aluminum in the Al-O gas, which was calculated by chemical equilibrium calculation in Section 1.5.1, to the numerical simulation results of the temperature and the Al-O gas concentration fields. The requirement for aluminum condensation is that the partial pressure of aluminum at the collection tube surface is larger than the saturated vapor pressure of aluminum at a temperature of 1500 K.

CALCULATION RESULT

The simulation results of the fields of temperature, Al-O pressure, aluminum partial pressure are presented in Figure A-2-2, Figure A-2-3, and Figure A-2-4, respectively. The temperature in the collection tube was decreased along with the axial direction from the center of ablation plume. As a result of this, the aluminum partial pressure on the collection tube surface was lower than that at the center of ablation plume. Figure A-2-5 shows the calculated distribution of aluminum partial pressure on collection tube in axial direction. The saturated vapor pressure of aluminum at a temperature of 1,500 K is 1.0 Pa. The calculated result shows the requirement for aluminum condensation are fully satisfied throughout the collection tube.

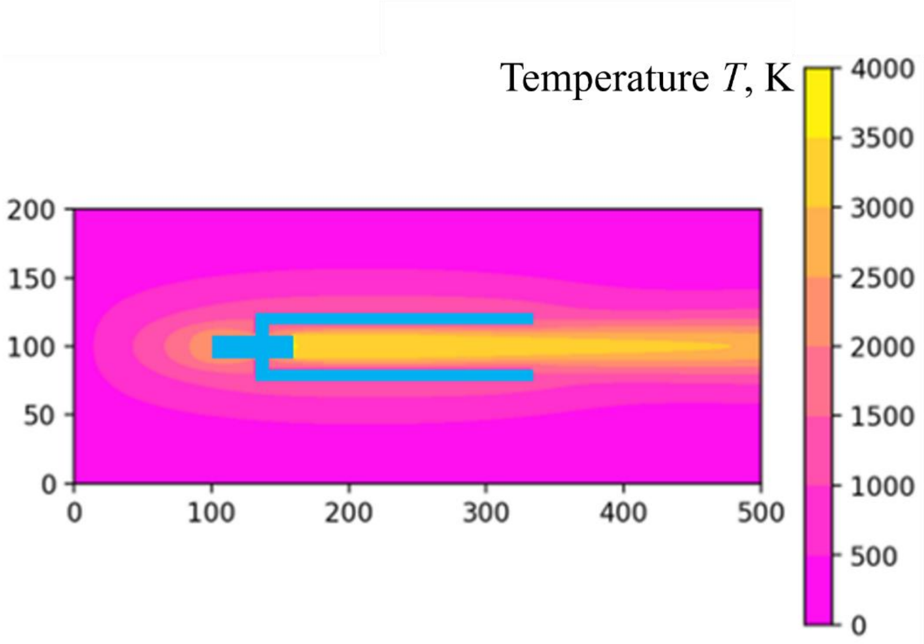

Figure A-2-2 Numerical simulation result of temperature field.

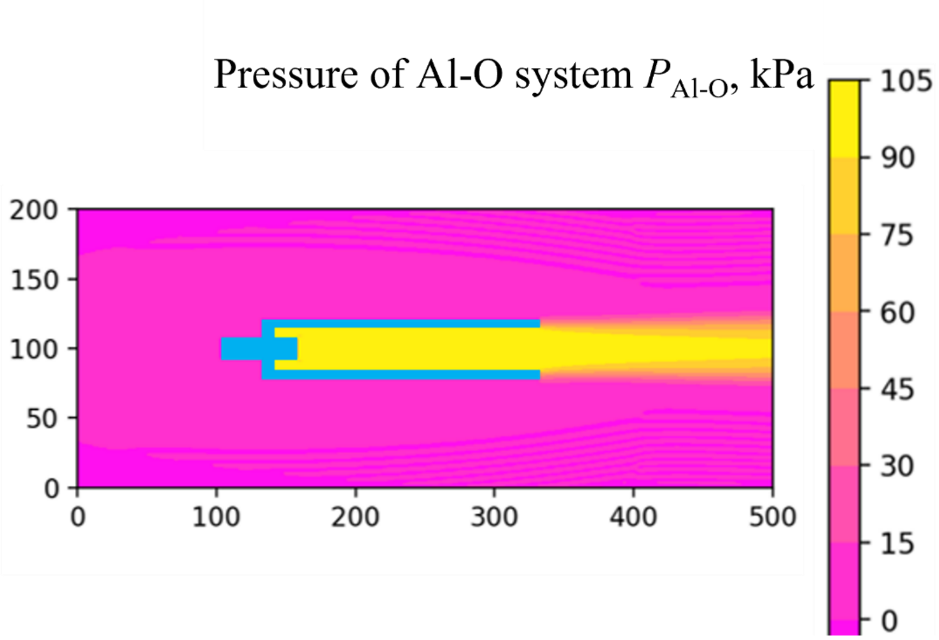

Figure A-2-3 Numerical simulation result of pressure field of Al-O system.

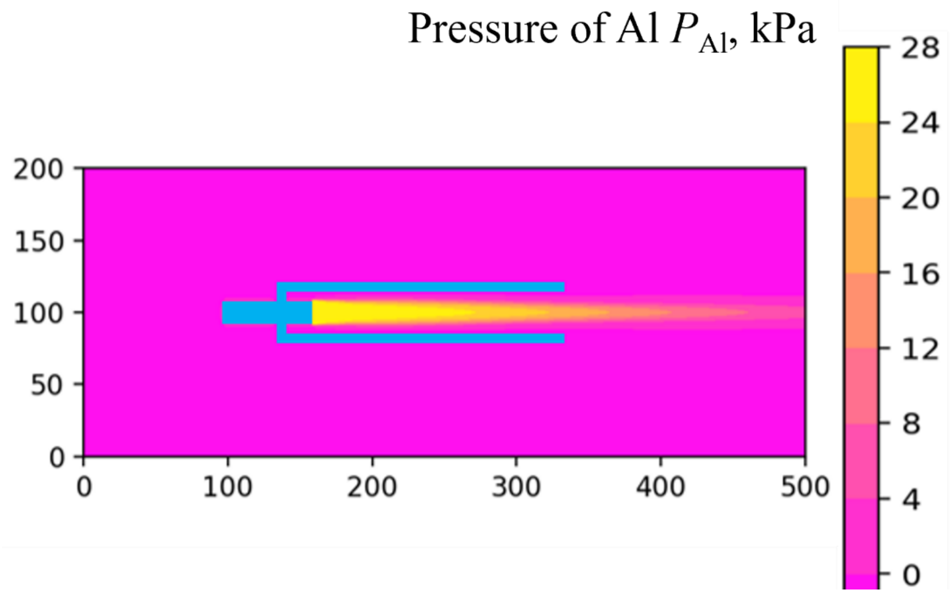

Figure A-2-4 Numerical simulation result of pressure field of aluminum.

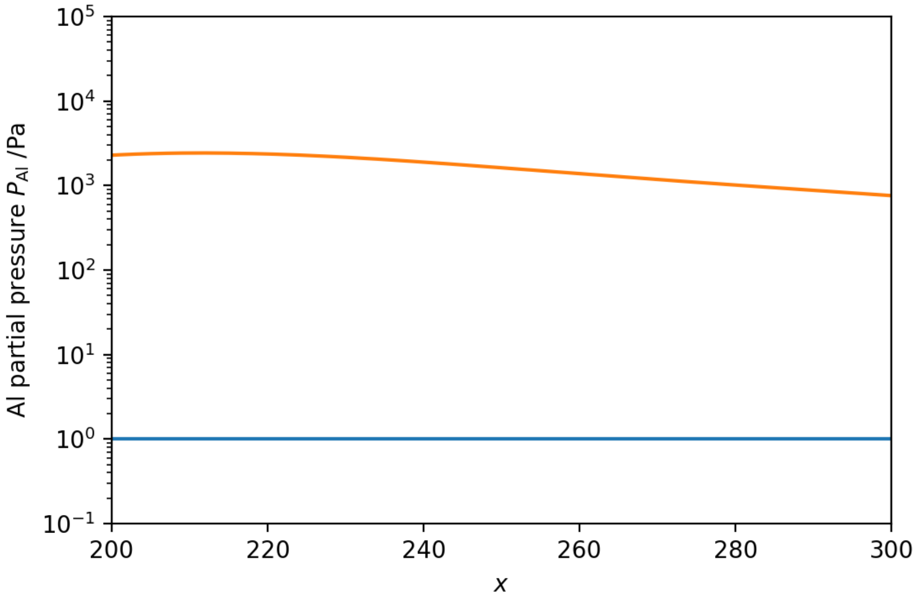

Figure A-2-5 Calculated distribution of aluminum partial pressure on collection tube in axial direction [93].

A.2.2 Aluminum collection system using a collection tube

Figure A-2-6 presents the schematic of experimental setup using a collection tube. The collection tube was set above the coil heater for alumina rod preheating. The laser ablation condition was same to that of collection experiments using a collection plate. The laser beam for laser ablation was irradiated through the inner of collection tube. The alumina rod was inserted into the alumina rod holder with a coil heater for alumina rod preheating. The collection tube was preheated to the temperature of 1,500 K by the semiconductor laser. The existence of aluminum on the collection plate after the laser ablation was verified using NaOH solution. The inner surface of the collection tube was observed by SEM.

Table A-2-1 Experimental conditions using a collection tube.

Laser ablation condition	
Laser power/ kW	2.0
Laser spot size on rod/ mm	2.0
Alumina rod radius/ mm	2.0
Laser intensity/ (GW/m^2)	0.16
Laser spot occupancy	1.0
Laser irradiation period/ s	1.0
Argon ambient pressure/ atm	1.0
Preheating temperature/ K	1,500
Collection plate condition	
Material	Alumina
Tube temperature /K	1,500
Distance between rod and plate /mm	5

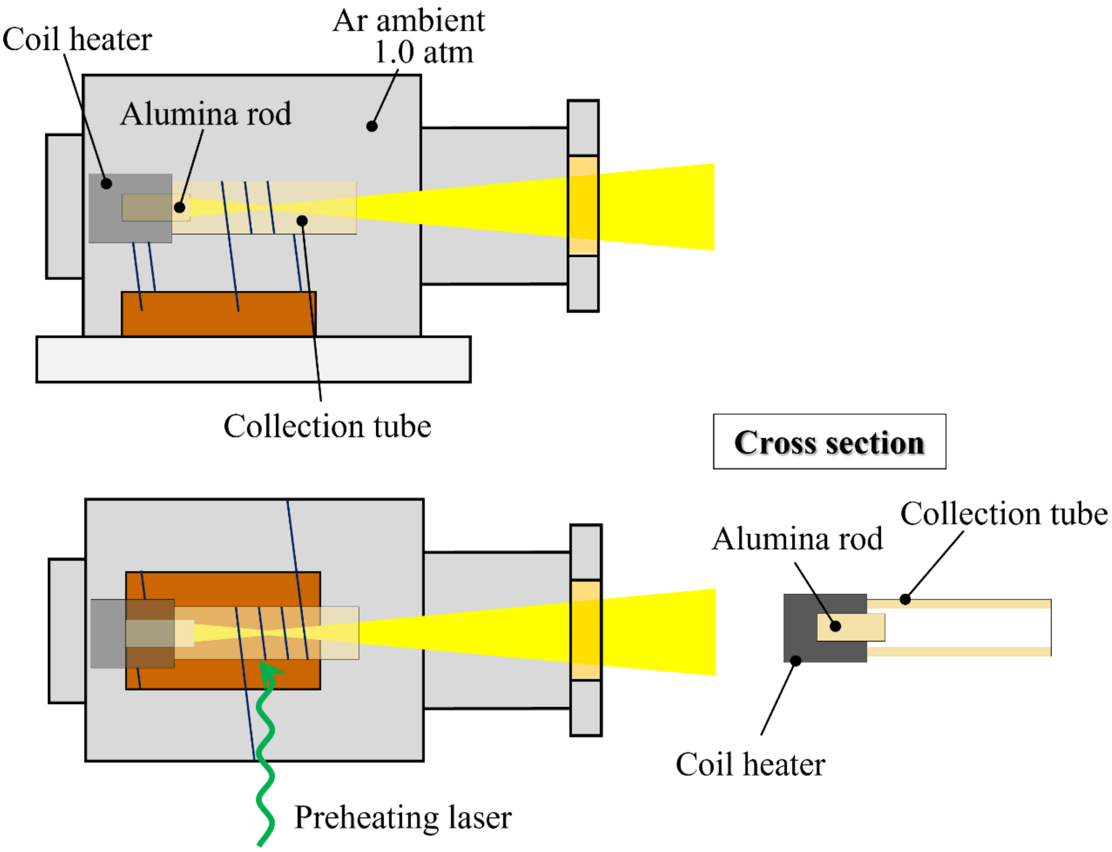

Figure A-2-6 Schematic of aluminum collection system using a collection tube.

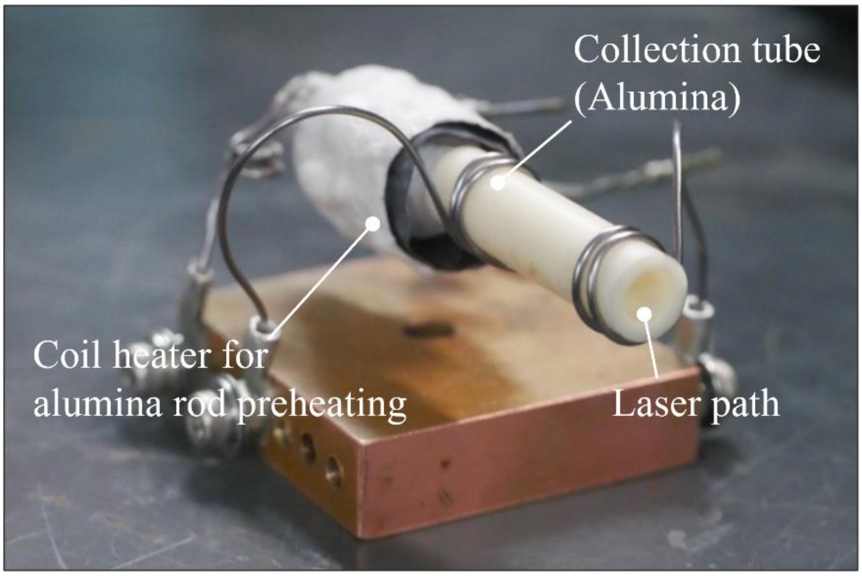

Figure A-2-7 Photograph of a collection tube and coil heater for alumina rod preheating.

A.2.3 Analysis of adhesion to the collection tube

ADHESION PERCENTAGE

Figure A-2-8 is the photograph of the collection tube at the laser ablation. Most parts of the ablation plume passed through the collection tube. As a result, the adhesion percentage by the collection tube was 7.4%, which was an order of magnitude smaller than the percentage by the collection plate.

ADHERED SUBSTANCES TO COLLECTION TUBE

Figure A-2-9 presents the photograph and SEM image of the collection tube. The black powders adhered to the inner of the collection tube. The black area was clarified to be oxygen-deficient alumina by the EDX analysis of SEM image. Moreover, particles were detected on the black area. As a result of the insertion of collection plate into NaOH solution, bubble ejection of hydrogen was observed, which indicates the existence of aluminum. After the chemical treatment, the particles disappeared. Therefore, the particles were confirmed to be aluminum. The adhered aluminum mass was estimated to approximately $\dot{m}_{\mathrm{Al}} = 0.001$ mg from the SEM observation. From the result, the aluminum collection percentage was calculated to $\eta_{\mathrm{co}} = 0.03\%$.

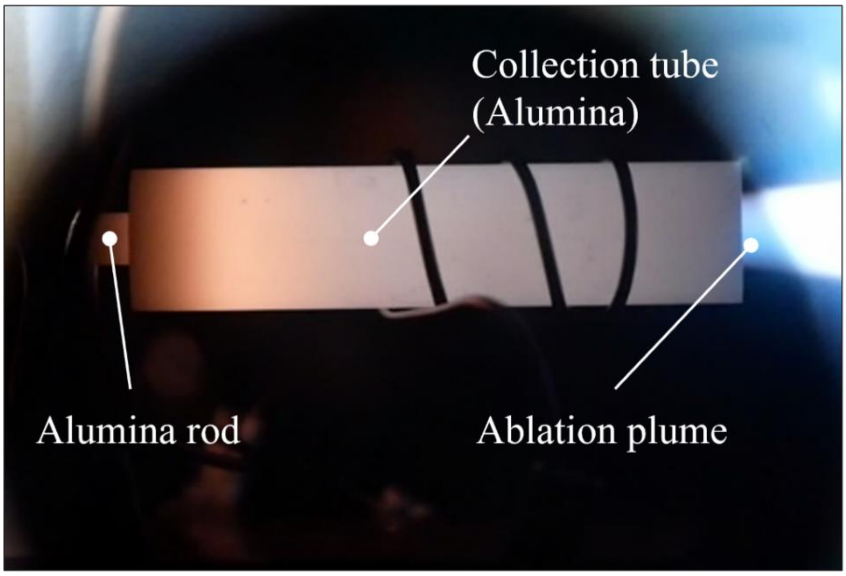

Figure A-2-8 Photograph of the collection tube with the ablation plume passing through the collection tube.

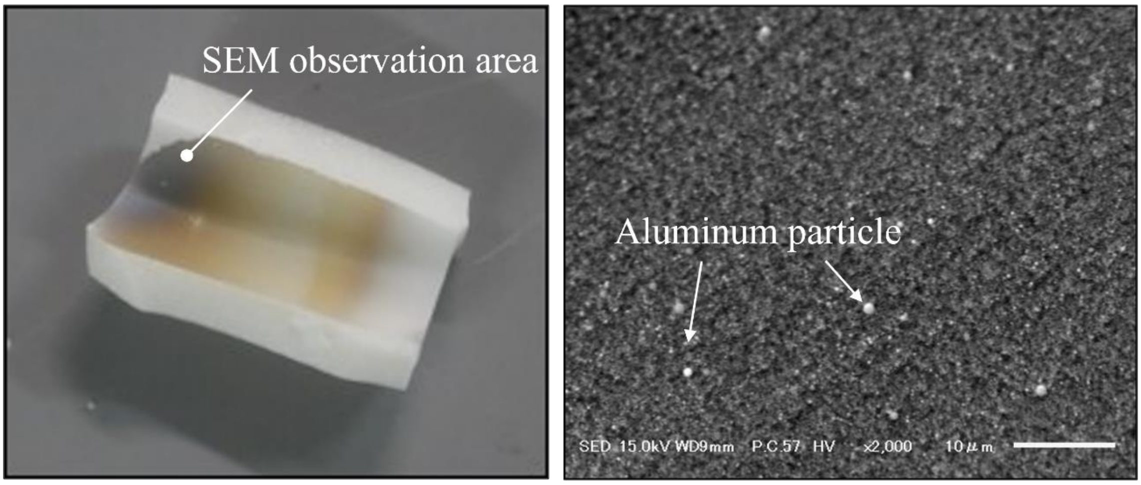

Figure A-2-9 Photograph and SEM picture of the collection tube after the laser ablation.

Appendix B

Effect of high boiling point material doped into alumina [103]

B.1 Background for high boiling point material doping into alumina

For lowering energy consumption for aluminum production, the increase of plume temperature is essential to achieve a high molar reduction percentage. However, the plume temperature by laser ablation was limited to T = 4,100 K: around the superheat limit temperature of alumina. In this research, a high boiling point material was added to the alumina sample to overcome the limit temperature of alumina. The addition of high boiling point material would increase the boiling point of mixed sample mainly composed of alumina.

In this research, zirconia ZrO_2 was adopted as the high boiling point material because of its high boiling point 4,500 K and availability from the lunar regolith. Table B-1 presents the temperatures related to the plume temperature of various materials. The superheat limit temperature was calculated by Guldberg laws, Eqs. (2-2) and (2-3). The values of zirconia doped alumina were estimated under the assumption that the temperatures of mixture change linearly depending on the compounding degree, the basic theory of mixture. The estimated superheat limit temperature of zirconia doped alumina was 4,700 K, which was 300 K larger than the value of pure alumina. The calculation result of molar reduction percentage under the condition of $5Al_2O_3 \cdot ZrO_2$ is presented in Figure B-1. The molar reduction percentage at the plume temperature of 4,700 K at 1.0

atm is 79%, which is about 2.5 times as large as the pure alumina result. Therefore, the improvement of molar reduction percentage was expected to be achieved by the addition of zirconia to alumina.

Table B-1 Melting point, boiling point and estimated superheat limit temperature of various materials. The values presented with "()" are estimated ones.

Material	Melting point /K	Boiling point /K	Superheat limit temperature estimated from Guldberg law /K
Alumina, Al_2O_3	2,300	3,250	(4,400)
Zirconia, ZrO_2	3,000	4,600	(6,200)
Zirconia doped alumina, $5Al_2O_3 \cdot ZrO_2$	(2,420)	(3,480)	(4,700)

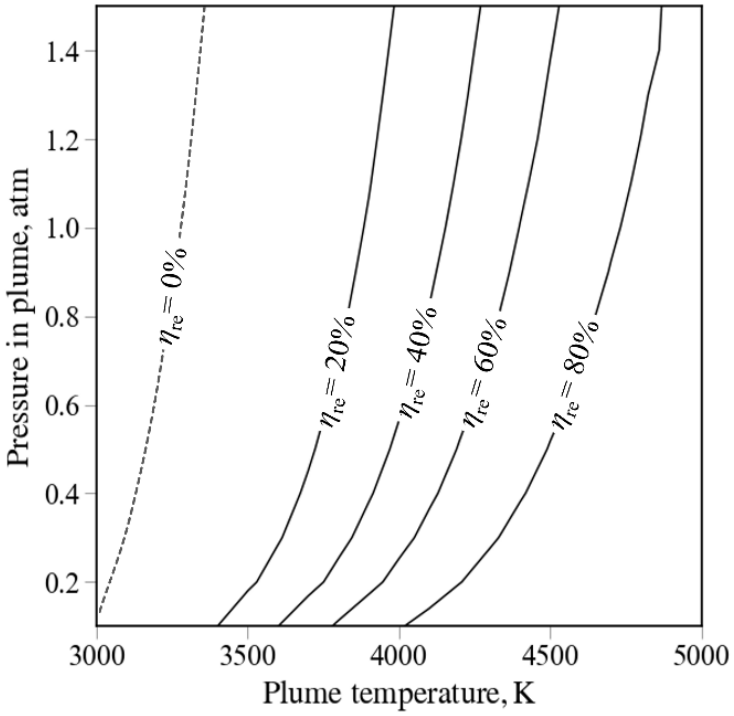

Figure B-1 Distribution map of molar reduction percentage of aluminum from $5Al_2O_3 \cdot ZrO_2$.

B.2 Laser ablation system of zirconia and zirconia doped alumina

Table A-2 presents the experimental conditions in the laser ablation experiments of zirconia and zirconia doped alumina. Firstly, for obtaining the preheating temperature to achieve the limit temperature, the experiment of ZrO_2 laser ablation with various preheating temperatures was conducted. The experimental setup was the same as that of the preheating experiment, as shown in Figure 2-2. The sample was preheated by the semiconductor laser to the preheating temperature of T_{pre}=1,500–2,300 K, which was measured by the emission spectroscopy, application of Planck's law fitting to the continuous spectrum. After the preheating process, the laser ablation by a CW CO_2 laser was conducted. The plume temperature was measured by emission spectroscopy with various laser intensities and preheating temperatures.

Finally, the laser ablation of zirconia doped alumina was conducted with various laser intensities at the preheating temperature, which was obtained in the laser ablation experiment of zirconia. The chemical composition of zirconia doped alumina was $5Al_2O_3{\cdot}ZrO_2$, which was commercially available in the Japanese company, Adamant Namiki Precision Jewel Co. The plume temperature of the zirconia doped alumina was measured to evaluate the temperature change from the value in the alumina laser ablation.

Table B-2 Laser ablation conditions of zirconia and zirconia doped alumina.

Material	ZrO_2, $5Al_2O_3{\cdot}ZrO_2$
Laser power/ kW	0.40–2.0
Laser intensity/ (GW/m^2)	0.30–2.7
Laser spot size on rod/ mm	0.49–1.5
Laser irradiation period/ s	1.0
Argon ambient pressure/ atm	1.0
Preheating temperature/ K	1,500–2,300

B.3 Measured of plume temperature

LASER ABLATION OF ZIRCONIA

The photographs of ejected ablation plume and rod after laser ablation are presented in Figure B-2. The color of ablation plume was bright orange, the emission from zirconium and zirconium oxide. Figure B-3 presents the emission spectrum from the ejected ablation plume. The spectra included the line spectra of zirconium and zirconia monoxide, Zr and ZrO, in all the experimental conditions. This result indicates the existence of gas state of zirconium and zirconia mono oxide. Figure B-4 shows results of measurements of the plume temperature of zirconia with various preheating temperatures and laser intensities. The plume temperature of zirconia was constant with laser intensity at a preheating temperature of T_{pre}= 1,900–2,300 K. Moreover, in the case of the preheating temperature of T_{pre}= 2,300 K, the plume temperature achieved the estimated superheat limit temperature of zirconia: 6,200 K. Therefore, the preheating temperature of zirconia doped alumina was determined to $T_{\mathrm{pre}} = 2{,}300$ K. The plume temperature at a preheating temperature of $T_{\mathrm{pre}} = 1{,}500$ K and a laser intensity of $F = 0.30$ GW/m^2 was lower than the boiling point of zirconia, even though the zirconium atom and zirconium monoxide were detected in the ablation plume. This result implies that the gas temperature in the ablation plume was low, and many liquid particles were cooled down under the boiling point in the case of low laser intensity and low preheating temperature.

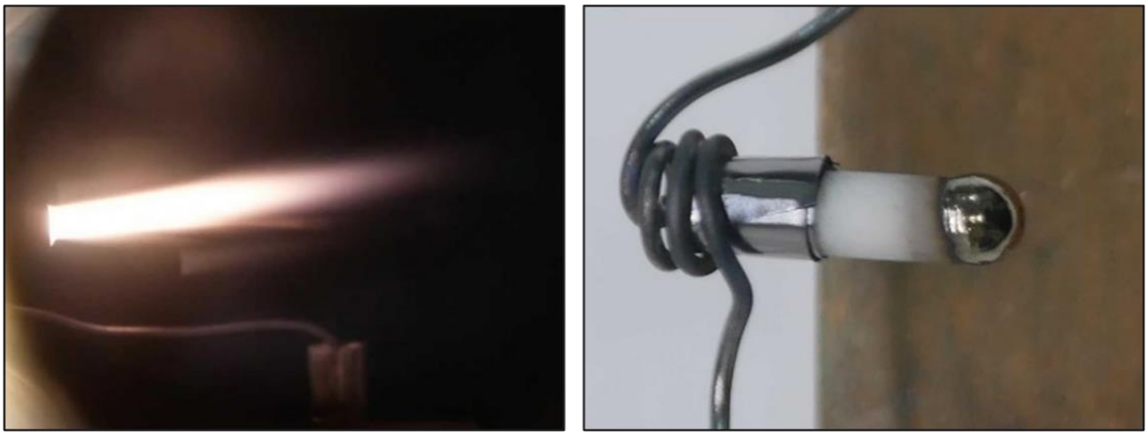

Figure B-2 Photographs of ablation plume (left) and zirconia rod after laser ablation (right).

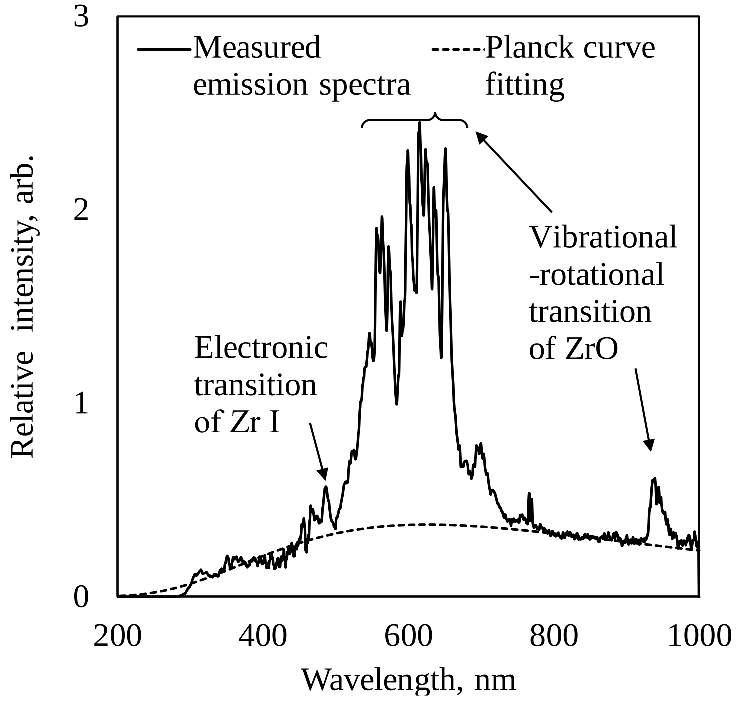

Figure B-3 Measured emission spectrum from the ablation plume of zirconia with Planck curve fitting line.

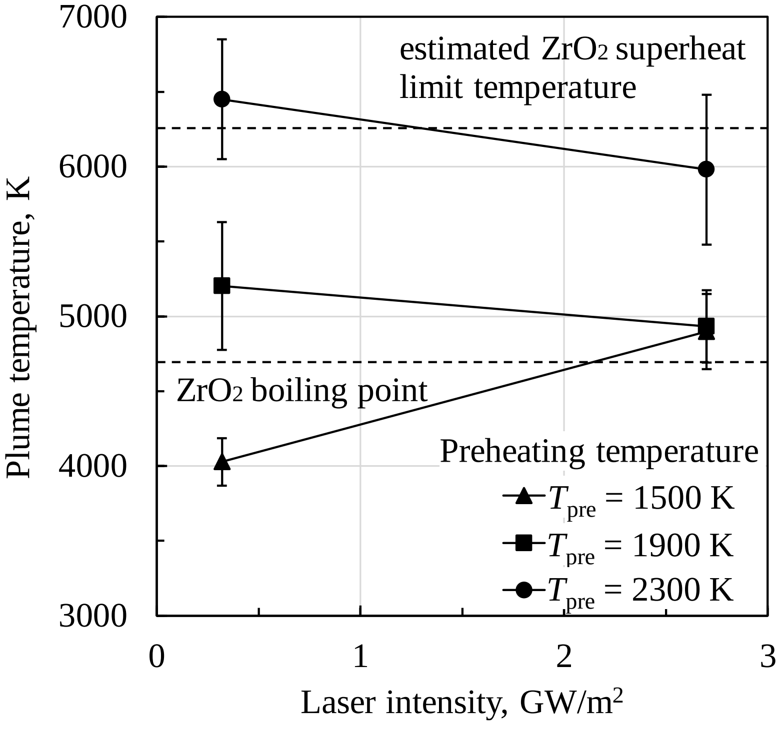

Figure B-4 Measured plume temperature of zirconia and alumina vs. laser intensities at various preheating temperatures.

LASER ABLATION OF ZIRCONIA DOPED ALUMINA, $5Al_2O_3 \cdot ZrO_2$

The photograph of ejected ablation plume and rod after laser ablation is presented in Figure B-5. The color of ablation plume was bright blue, which was similar to the ablation plume of pure alumina. This result suggests that the ablation plume was composed mainly of alumina ablated substances. At a preheating temperature of T_{pre}=2,300 K, the zirconia doped alumina at the laser spot of semiconductor laser was melted during the preheating process. This result suggests that the melting point of zirconia doped alumina, $5Al_2O_3 \cdot ZrO_2$, was decreased to the temperature under the melting point of alumina: 2300 K. This result was contrary to the estimated result of the melting point of zirconia doped alumina under the assumption of the temperature of the melting surface could not be controlled stably because of its high energy absorption of laser energy. Therefore, the condition of preheating temperature was changed to T_{pre}=1,900 K.

Figure B-6 presents the emission spectrum from the ablation plume of zirconia doped alumina. The line spectra of aluminum, aluminum monoxide and zirconia monoxide were detected. This result indicates that the vaporization of the zirconia doped alumina occurred successfully. The measurement result of plume temperature with various laser intensities is portrayed in Figure B-7. The plume temperature of zirconia doped alumina was 3,930 K, which was smaller than that of pure alumina: 4,100 K. Therefore, the plume temperature was decreased by the zirconia doping to alumina. Moreover, the plume temperature was smaller than the boiling point of zirconia: 4,600 K, even though the laser intensity of 2.7 GW/m^2 was large enough to cause the ablation of pure zirconia and alumina as shown in Figure B-7.

The decrease of boiling point by doping could occur the decrease of plume temperature even though the laser ablation occurred. Previous studies have shown that the boiling point of mixtures does not change linearly with the molar ratio depending on the material combination [55]. This phenomenon is called azeotrope. The boiling point of mixtures can have maximal or minimal values because of its heterogeneous intermolecular force: negative and positive azeotrope, respectively. For the reason that vaporization is encouraged in the case of weak intermolecular force, the boiling point can be lower than the value estimated under the assumption that the boiling point of mixture changes linearly depending on the compounding degree because. The mixture of alumina and zirconia could be the positive azeotrope, and the boiling point of zirconia doped alumina was decreased. This should be the reason for the decrease of plume temperature. The detection of applicable material for negative azeotropes with alumina should be the one way for plume temperature increase.

Figure B-5 Photographs of ablation plume (left) and zirconia doped alumina rod after laser ablation (right).

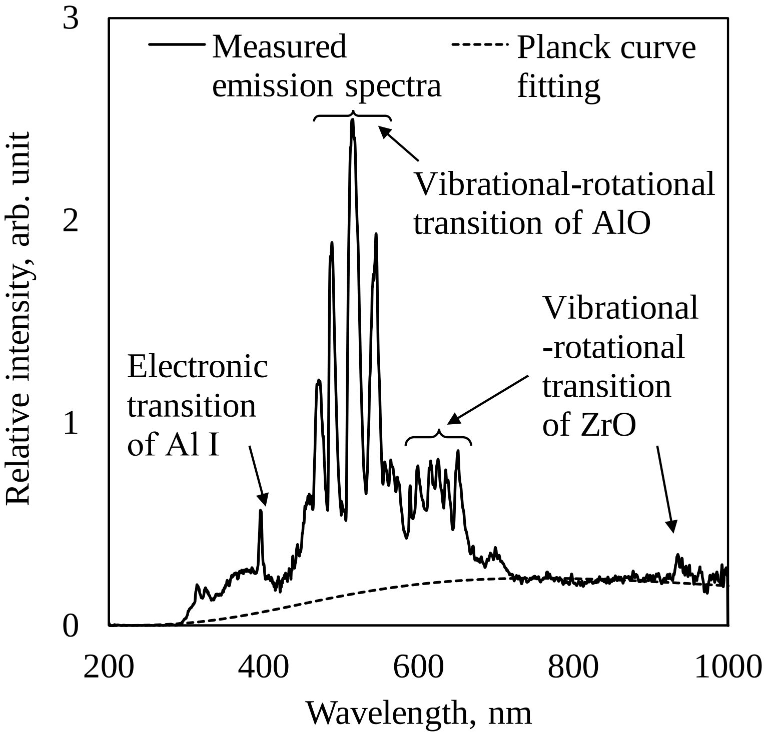

Figure B-6 Measured emission spectrum from the ablation plume of zirconia with Planck curve fitting line.

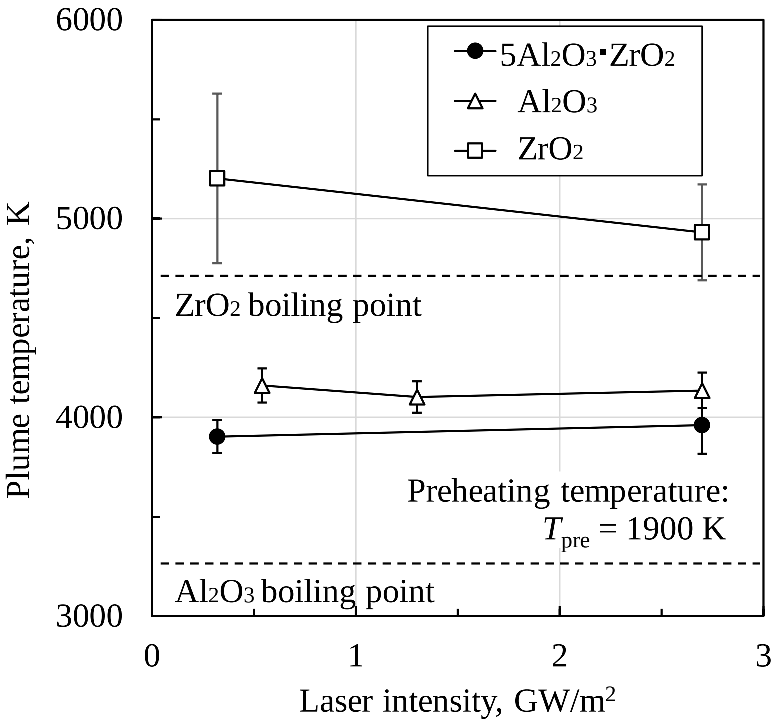

Figure B-7 Measured plume temperature of zirconia and alumina vs. laser intensities at a preheating temperature of T_{pre}=1,900 K.

Bibliography

[1] T. Hoshino, S. Wakabayashi, M. Ohtake, Y. Karouji, T. Hayashi, H. Morimoto, H. Shiraishi, T. Shimada, T. Hashimoto, H. Inoue, R. Hirasawa, Y. Shirasawa, H. Mizuno, H. Kanamori, Lunar polar exploration mission for water prospection – JAXA's current status of joint study with ISRO, Acta Astronautica 176, (2020) 52–58.

[2] L.B. Strogonova, Manned Expedition to Mars: Concepts & Problems, Acta Astronautica 23, (1991) 279–287.

[3] E. Detsis, O. Doule, A. Ebrahimi, Location selection and layout for LB10, a lunar base at the Lunar North Pole with a liquid mirror observatory, Acta Astronautica 85, (2013) 61–72.

[4] M. Kaczmarzyk, M. Musial, Parametric Study of a Lunar Base Power Systems, Energies 14(4), (2021) 1141.

[5] M. Anand, I.A. Crawford, M. Balat-Pichelin, S. Abanades, W. van Westrenen, G. Peraudeau, R. Jaumann, W. Seboldt, A brief review of chemical and mineralogical resources on the Moon and likely initial in situ resource utilization (ISRU) applications, Planetary and Space Science 74 (2012) 42–48.

[6] P.D. Spudis, A.R. Lavoie, Using the resources of the Moon to create a permanent, cislunar space-faring system, AIAA SPACE 2011 Conference & Exposition, September 2011, California, USA, 27–29.

[7] S. Ulamec, J. Biele, E. Trollope, How to survive a Lunar night, Planetary and Space Science 58 (2010) 1985–1995.

[8] H. Benaroya, S. Mottaghi, Z. Porter, Magnesium as an ISRU-Derived Resource for Lunar Structures, Journal of Aerospace Engineering 26(1), (2013) 152–159.

[9] C. Schwandt, J.A. Hamilton, D.J. Fray, I.A. Crawford, The production of oxygen and metal from lunar regolith, Planetary and Space Science 74, (2012) 49–56.

[10] G. Corrias, R. Licheri, R. Orru, G. Cao, Optimization of the self-propagating high-

temperature process for the fabrication in situ of Lunar construction materials, Chemical Engineering Journal 193–194, (2012) 410–421.

[11] M.F. Palos, P. Serra, S. Fereres, K. Stephenson, R. González-Cinca, Lunar ISRU energy storage and electricity generation, Acta Astronautica 170, (2020) 412–420.

[12] M. Hecht, J. Hoffman, D. Rapp, et al., Mars Oxygen ISRU Experiment (MOXIE), Space Science Review 217(9), (2021) .

[13] G.H. Heiken, D.T. Vaniman, B.M. French, Lunar Sourcebook, Cambridge University Press (1991).

[14] S. J. Indyk, H. Benaroya, A structural assessment of unrefined sintered lunar regolith simulant, Acta Astronautica 140, (2017) 517–536.

[15] G. Corrias, R. Licheri, R. Orrù, G. Cao, Optimization of the self-propagating high-temperature process for the fabrication in situ of Lunar construction materials, Chemical Engineering Journal 193–194 (2012) 410–421.

[16] P.M. Raju, Advances in manufacture of Mooncrete – a Review, International Journal of Engineering Science & Advanced Technology 4 (5), (2014) 501–510.

[17] K. Wang, P.N. Lemougna, Q. Tang, W. Li, X. Cui, Lunar regolith can allow the synthesis of cement materials with near-zero water consumption, Gondwana Research, 44, (2017) 1–6.

[18] N. Saburo, I. Hiroo, E. Hiroshi, and I. Shu, Eds., 理化学事典, 5th ed. Tokyo: 岩波書店, 1998, p.1854.

[19] A.V. Blinova, P.P. Chekmareva, V. Ya. Il'ichev, A.I. Telegon, Mechanical Properties of Aluminum Alloys at Temperatures Down to 4.2 K, Metal Science and Heat Treatment 17(6), (1975) 502–505.

[20] K. K. Sharma, M. Singh, Variation of beta-ray backscattering with target thickness, Journal of Applied Physics 50(3), (1979) 1529–1532.

[21] M. L. Rustgi and J.E. Turner, P. T. Leung, Stopping power of matter for alpha particles at extreme relativistic energies, Physical Review A 22(6), (1980) 2510–2522.

[22] G. L. Cherepakhova, L. A. Levina, A. V. Shreider, V. G. D'yakov, Corrosion Resistance of Aluminum and Its Alloys in Atmospheres of Chemical Plants, Chemical and Petroleum Engineering 13(7), (1977) 621–623.

[23] R. Watanabe, Production of aluminum metal, Light metal 39(5), (1989) 403–414.

[24] J. Vind, A. Malfliet, C. Bonomi, P. Paiste, I. E. Sajó, B. Blanpain, A. H. Tkaczyk, V. Vassiliadou, D. Panias, Modes of occurrences of scandium in Greek bauxite and bauxite residue, Minerals Engineering 123, (2018) 35-48.

[25] F. A. Peters, R. C. Kirby, K. B. Higbie, Methods for producing alumina from clay an evaluation, Journal of Metals 19(10), (1967) 26–34.

[26] H. Kvande, The Aluminum Smelting Process, Journal of Occupational and Environmental Medicine 56(5S), (2014) S2–S4.

[27] N. Masuko, K Masio, Present aluminum smelting technology, Journal of the Japan Institute of Light Metals 65(2), (2015) 66–71.

[28] K. Xie, Z Shi, J Xu, X Hu, B Gao, Z. Wang, Aluminothermic Reduction-Molten Salt Electrolysis Using Inert Anode for Oxygen and Al-Base Alloy Extraction from Lunar Soil Simulant, Journal of Metals 89 (10), (2017) 1963–1969.

[29] W. Wei, S. Geng, D. Xie, F. Wang, High temperature oxidation and corrosion behaviours of Ni–Fe–Cr alloys as inert anode for aluminum electrolysis, Corrosion Science 157, (2019) 382-391.

[30] S. Helle, B. Davis, D. Guay, L. Roue, Ball-Milled (Cu-Ni-Fe + Fe_2O_3) Composite as Inert Anode for Aluminum Electrolysis, Journal of the Electrochemical Society 160 (6), (2013) E55-E59.

[31] H. Kvande, W. Haupin, Inert Anodes for Al Smelters: Energy Balances and Environmental Impact, Journal of Metals 53(5), (2011) 29–33.

[32] S. Helle, B. Davis, D. Guay, L. Roué, Electrolytic Production of Aluminum Using Mechanically Alloyed Cu–Al–Ni–Fe-Based Materials as Inert Anodes, Journal of The Electrochemical Society 157(11), (2010) E173-E179.

[33] W.B. White, S.M. Johnson, G.B. Dantzig, Chemical Equilibrium in Complex Mixtures, The Journal of Chemical Physics 28, (1958) 751–755.

[34] M.W. Chase, NIST-JANAF Thermochemical Tables (J. Phys. Chem. Ref. Data Monograph 9 1998), Fourth ed.

[35] T. Yabe, M.S. Mohamed, S. Uchida, C. Baasandash, Y. Sato, M. Tsuji, Y. Mori, Noncatalytic dissociation of MgO by laser pulses towards sustainable energy cycle, Journal of Applied Physics 101(123106), (2007) 1–7.

[36] M.S. Mohamed, T. Yabe, C. Baasandash, Y. Sato, Y. Mori, L.S. Hua, H. Sato, S. Uchida, Laser induced magnesium production from magnesium oxide using reducing agents, Journal of Applied Physics 104 (113110), (2008).

[37] M.S. Mahmoud, T. Yabe, Silicothermic reduction of MgO using diode laser: Experimental and kinetic study, Journal of Magnesium and Alloys 5(4), (2017) 430–438.

[38] M.S. Mahmoud, T. Yabe, E. Iida, Novel Approach for the Reduction of ZnO and

MgO Using a Direct Diode-Laser, Metallurgical and Materials Transactions B 48(1), (2017) 179–186.

[39] M. Oliveira, D. Liang, J. Almeida, C.R. Vistas, F. Gonçalves, R. Martins, A path to renewable Mg reduction from MgO by a continuous-wave Cr:Nd:YAG ceramic solar laser, Solar Energy Materials and Solar Cells 155, (2016) 430-435.

[40] T. Yabe, A New Energy Cycle Utilizing Solar Pumped Laser and Magnesium, The review of laser engineering 38(3), (2010) 176–179.

[41] T. Saiki, S. Motokoshi, K. Imasaki, H. Fujita, M. Nakatsuka, C. Yamanaka, Nd/Cr:YAG Ceramic Rod Laser Pumped Using Arc-Metal-Halide-Lamp, Journal of Applied Physics 46, (2007) 156–160.

[42] S. Payziyev, K. Makhmudov, Solar pumped Nd:YAG laser efficiency enhancement using Cr:LiCAF frequency down-shifter, Optics communications 380, (2016) 57–60.

[43] R. Rajasekar, P. Prasannaa, R. Ramkumar, Efficiency of solar PV panel by the application of coconut fibres saturated by earthen clay pot water, Environmental Technology 42(3), (2021) 358–365.

[44] T. Ma, H. Yang, Y. Zhang, L. Lu, X. Wang, Using phase change materials in photovoltaic systems for thermal regulation and electrical efficiency improvement: A review and outlook, Renewable and Sustainable Energy Reviews 43, (2015) 1273–1284.

[45] L.T.B. Mendonça, A.G. Bezerra, W.M. de Azevedo, Preparation and characterization of V2O5 and V2O5/PANI nanocomposite by laser ablation technique in liquid, Materials Chemistry and Physics 273, (2021) 125084.

[46] M. Hiramatsu, K. Imaeda, N. Horio, M. Nawata, Transparent conducting ZnO thin films prepared by XeCl excimer laser ablation, Journal of Vacuum Science & Technology A: Vacuum, Surfaces, and Films 16(2), (1998) 669–673.

[47] A.V. Rode, B. Luther-Davies, E.G. Gamaly, Ultrafast ablation with high-pulse-rate lasers. Part II: Experiments on laser deposition of amorphous carbon films, Journal of Applied Physics 85(8), (1999) 4222–4230.

[48] P. Suzana, D. Milovanović, B. Salatić, D. Peruško, J. Kovač, G. Dražić, M. Mitrić, M. Trtica, B. Jelenković, Composition and structure of NiAu nanoparticles formed by laser ablation of Ni target in Au colloidal solution, Materials Chemistry and Physics 166(15), (2015) 223–232.

[49] M. Matsui, N. Fukuji, M. Nakano, Alumina reduction by laser sustained plasma for aluminum-based renewable energy cycling, Journal of Renewable and Sustainable

Energy 5(3), (2013) 039101.

[50] N. Fukuji, M. Matsui, Y. Yamagiwa, Evaluation of Flow Characteristics and Alumina Reduction Efficiency in Laser Plasma Wind Tunnel Flows by Emission Spectroscopy, Applied Plasma Science 21(1), (2013) 47–50.

[51] N. Fukuji, M. Matsui, M. Nakano, Y. Yamagiwa, K. Komurasaki, Y. Arakawa, T. Goto, H. Shirakata, Influence of Plasma Fluctuation and Size on Reduction Efficiency of Alumina, Frontier of Applied Plasma Technology 6(2), (2013).

[52] K. Tanaka, M. Matsui, M. Nakano, et al., A Preliminary Study of Alumina Reduction in a Laser Sustained Plasma Flow, Plasma Application and Hybrid Functional Materials 21, (2012) 19–20.

[53] M. Matsui, K. Shinmi, T. Ueno, K. Komurasaki, Y. Arakawa, Operation Characteristics of Laser Driven Plasma Wind Tunnel, Trans. JSASS Space Tech. Japan 7(26), (2009) 31–39.

[54] M. Ishii, M. Matsui, Energy Conversion Efficiency Measurement of Alumina Reduction Using Laser Ablation, Journal of IAPS 25(2), (2017) 89–93.

[55] C. T. Avedisian, J. R. Sullivan, A Generalized Corresponding States Method for Predicting the Limits of Superheat of Mixtures, Chemical Engineering Science 39(6), (1984) 1033–1041.

[56] N. Fabrlclus, P. Hermes, D. yon der Linde, A. Pospieszczyk, B. Stritzker, Observation of Superheating During Picosecond Laser Melting, Solid State Communications 58(4), (1986), 239–242.

[57] M.Q. Jiang, Y.P. Wei, G. Wilde, L.H. Dai, Explosive boiling of a metallic glass superheated by nanosecond pulse laser ablation, Applied Physics Letter 106, (2015) 021904.

[58] M.M. Martynyuk, Superheating of solid and liquid metals in the process of pulse heating, Thermochimica Acta 206(10), (1992) 55–60.

[59] C.M. Guldberg, Über die Gesetze der Molekularvolumina und der Siedepunkte, Zeitschrift für Physikalische Chemie 5, (1890) 374–382.

[60] Y. Ralchenko, A.E. Kramida, J. Reader, Atomic Spectra Database.

[61] A.E. Siegman, S.W. Townsend, Output Beam Propagation and Beam Quality from a Multimode Stable-Cavity Laser, IEEE Journal of Quantum Electronics 29(4), (1993) 1212–1217.

[62] S. Sinha, Thermal model for nanosecond laser ablation of alumina, Ceramics International 41(5), (2015) 6596–6603.

[63] J. Jamdeleit, G. Urbasch, H.D. Hoffman, H.G. Treusch, E.W. Kreutz, Picosecond laser ablation of thin copper films, Applied Physics A 52(2), (1996) 117–121.

[64] M. Hashida, A.F. Semerok, O. Gobert, G. Petite, Y. Izawa, J.F. Wagner, Ablation threshold dependence on pulse duration for copper, Applied Surface Science 197-198(30), (2002) 862–867.

[65] K. Nagashima, M. Hashida, M. Katto, M. Tsukamoto, M. Fujita, Y. Izawa, Femtosecond Laser Ablation of Al_2O_3 ceramics, Institute of Electrical Engineers of Japan Transactions on Electronics, Information and Systems 124(2), (2004) 388–392.

[66] P.F. Paradis, T. Ishikawa, Y. Saita, S. Yoda, Non-Contact Thermophysical Property Measurements of Liquid and Undercooled Alumina, Japanese Journal of Applied Physics 43(4A), (2004) 1496–1500.

[67] P.A. Atanasov, E.D. Eugenieva, N.N. Nedialkov, Laser drilling of silicon nitride and alumina ceramics: A numerical and experimental study, Journal of Applied Physics 89(4), (2001) 2013–2016.

[68] G. Ito, Corrosion of Aluminum and its alloys, Corrosion Engineering 27(4), (1978) 194–202.

[69] P.E. Doherty, R.S. Davis, Direct Observation of the Oxidation of Aluminum Single-Crystal Surfaces, Journal of Applied Physics 34, (1963) 619–628.

[70] S. Niu, Q. You, X. Yout, S. Shi, Y. Wang, Mechanism of impurities reduction and evaporation of alloying elements for a multi-element Ni-based superalloy during electron beam remelting, Vacuum 156, (2018) 345–350.

[71] A. Goto, T. Aizawa, S. Okada, On the Amount of Graphite Formed during Freezing and Cooling in Spheroidal Graphite Cast Iron, Casting Engineering 50(6), (1978) 345–349.

[72] H. Yanagida, F.A. Kroger, The System Al-O, Journal of the American Ceramic Society 51(12), (1968) 700–706.

[73] V.S. Kortov, S.V. Zvonarev, A.N. Kiryakov, D.V. Ananchenko, Dosimetric phosphor based on oxygen-deficient alumina ceramics, Radiation Measurements 90, (2016) 196–200.

[74] K. Mitsuhara, T. Matsuda, H. Okumura, A. Visikovskiy, Y. Kido, Oxygen deficiency and excess of rutile titania (110) surfaces analyzed by ion scattering coupled with elastic recoil detection, Nuclear Instruments and Methods in Physics Research Section B: Beam Interactions with Materials and Atoms 269(16), (2011) 1859–1864.

[75] A.S. Abyzov, L.N. Davydov, J.W. P. Schmelzer, Heterogeneous Nucleation in Solutions on Rough Solid Surfaces: Generalized Gibbs Approach, Entropy 21(8), (2019) 782.

[76] H. Yuan, S. Tan, W. Du, S. Ding, C. Guo, Heterogeneous bubble nucleation model on heated surface based on free energy analysis, International Journal of Heat and Mass Transfer 122, (2018) 1198–1209.

[77] Q. Guo, P. Cheng, Effects of non-uniform temperature of the ice nucleus on heterogeneous ice nucleation, International Journal of Heat and Mass Transfer 163, (2020) 120404.

[78] M.G. Abdoelatef, F. Badry, D. Schwen, C. Permann, Y. Zhang, K. Ahmed, Mesoscale Modeling of High Burn-Up Structure Formation and Evolution in UO_2, The Journal of The Minerals, Metals & Materials Society 71, (2019) 4817–4828.

[79] T. Li, C. Liu, Z. Zhang, B. Yu, H. Dong, W. Jia, Z. Jia, C. Yu, L. Gan, B. Xu, H. Jiang, Understanding the Growth Mechanism of GaN Epitaxial Layers on Mechanically Exfoliated Graphite, Nanoscale Research Letters 13(1), (2018) 130.

[80] J.W.P. Schmelzer, On the determination of the kinetic pre-factor in classical nucleation theory, Journal of Non-Crystalline Solids 356(52–54), (2010) 2901–2907.

[81] J.B. John, A.P. Joseph, Effect of Nature of Surfaces on Wetting of Sapphire by Liquid Aluminum, Journal of the American Ceramic Society 51(10), (1968) 569–573.

[82] R. Finsy, On the critical radius in Ostwald ripening, Langmuir 20(7), (2004) 2975–2976.

[83] M.D. Abramoff, P.J. Magelhaes, S.J. Ram, Image Processing with ImageJ, Biophotonics International 11(7), (2004) 36–42.

[84] Y. Huang, Y. Yan, G. Riley, Vision-based measurement of temperature distribution in a 500-kW model furnace using the two-colour method, Measurement 28(3), (2000) 175–183.

[85] L. Zhiying, H. Bei, L. Tianyi, Z. Yu, A Review on Additive Manufacturing of Titanium Alloys for Aerospace Applications: Directed Energy Deposition and Beyond Ti-6Al-4V, The Journal of the Minerals, Metals & Materials Society 73, (2021) 1804–1818.

[86] T. Nishikawa, T. Nishida, K. Inoue, High Temperature Deformation of Polycrystalline β-Alumina, Yogyo-Kyokai-Shi 83(1), (1975) 13–17.

[87] J.H. Hildebrand, The Vapor Pressures of Liquid Metals, Journal of the American Chemical Society 40(1), (1918) 45–49.

[88] S. K. Rhee, Wetting of Ceramics by Liquid Aluminum, Journal of the American Ceramics Society 53, (1970) 386–389.

[89] L. Goumiri, J. C. Joud, P. Desre, Tensions superficielles d'alliages liquides binaires présentant un caractère dimmiscibilité: Al-Pb, Al-Bi, Al-Sn et Zn-Bi, Surface Science 83, (1979) 471–486.

[90] M.J. Assael, K. Kakosimos, R.M. Banish, J. Brillo, I. Egry, R. Brooks, P.N. Quested, K.C. Mills, A. Nagashima, Y. Sato, W.A. Wakeham, Reference Data for the Density and Viscosity of Liquid Aluminum and Liquid Iron, Journal of Physical and Chemical Reference Data 35, (2006) 285–300.

[91] N. V. Alexey, V. Z. Leonid, Melt dynamics and melt-through time in continuous wave laser heating of metal films: Contributions of the recoil vapor pressure and Marangoni effects, International Journal of Heat and Mass Transfer 112, (2017) 300–317.

[92] S. Yamada, S. Tanaka, K. Komurasaki, R. Kawashima, H. Koizumi, Characterization of Reduction Products Generated by Laser Ablation of Alumina, Journal of IAPS 26(1), (2018) 33–38.

[93] S. Yamada, アルミナレーザー還元における生成アルミニウムの不均一凝縮核生成による回収, Master thesis in the University of Tokyo, 2019.

[94] H. Kimura, O. Nakano, T. Ohkoshi, On the aluminum-tantalum system, Light metal 23(3), (1973) 106–112.

[95] S. Maruyama, Molecular Dynamics Simulations of Heterogeneous Nucleation of Vapor Bubble and Liquid Droplet on Solid Surface, Japan Journal of Multiphase Flow 15(1), (2001) 39–46.

[96] K. Yasuoka, M. Matsumoto, Molecular dynamics of homogeneous nucleation in the vapor phase. I. Lennard-Jones fluid, Journal of Chemical Physics 109(19), (1998) 8451–8462.

[97] H. Toyota, T. Ide, H. Yagi, K. Endo, Y. Mori, K. Hirose, A New Measurement and Evaluation of Wettability between Solid and Liquid Metals in Ultra-High Vacuum (2nd Report), Journal of the Japan Society for Precision Engineering 66(7), (2000) 1120–1124.

[98] G.I. Nikolaev, N.V. Bodrov, Study by atomic absorption of the evaporation of aluminium impurities from tantalum and niobium, Russian Journal of Physical Chemistry 52, (1978), 821-823.

[99] H. Zhang, P. Feng, F. Akhtar, Aluminium matrix tungsten aluminide and tungsten reinforced composites by solid-state diffusion mechanism, Science Report 7, (2017) 12391.

[100] L. Brewer, A.W. Searcy, The Gaseous Species of the Al-Al_2O_3 System, Journal of the American Chemical Society 73(1), (1951) 5308–5314.

[101] A. Rubinraut, Moonplane—A Spacecraft for Regular Delivery of Astronauts onto the Moon, Advances in Aerospace Science and Technology 4(3), (2019).

[102] IEA, Energy Prices and Taxes, 2019 (1) First Quarter 2019, (2019), OECD Publishing, Paris.

[103] S. Sato, ジルコニア混合によるレーザーアルミナ還元率向上, Bachelor thesis in the University of Tokyo, 2019.

This dissertation is based on the following journal papers written by the author.

Chapter 2:

S. Tanaka, S. Yamada, R. Soga, K. Komurasaki, R. Kawashima, H. Koizumi, Alumina reduction by laser ablation using a continuous-wave CO_2 laser toward lunar resource utilization, Vacuum 167, (2019) 495-499.

S. Tanaka, S. Yamada, K. Komurasaki, H. Koizumi, Laser Spot Size and Preheating Effects on Alumina Reduction Using Laser Ablation, Journal of Thermophysics and Heat Transfer 34 (4), (2020) 733-740.

Chapter 3:

S. Tanaka, N. Tanaka, K. Komurasaki, R. Kawashima, H. Koizumi, Aluminum particle production on alumina rod surface by continuous-wave laser ablation, Materials Chemistry and Physics 278, (2022) 125557.